PB81-238537

NBS: Materials Measurements

(U.S.) National Bureau of Standards
Washington, DC

Prepared for

National Aeronautics and Space Administration
Washington, DC

Jun 81

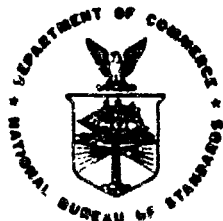# NBSIR 81-2295

NBS: Materials Measurements

U.S. Department of Commerce
National Bureau of Standards
Washington, DC 20234
Phone: (301) 921 3354

U.S. DEPARTMENT OF COMMERCE

NATIONAL BUREAU OF STANDARDS

4. TITLE AND SUBTITLE

NBS: Materials Measurements

5. AUTHOR(S)

J. R. Manning

11. ABSTRACT (A 200-word or less factual summary of most significant information. If document includes a significant bibliography or literature survey, mention it here)

This report describes NBS work for NASA in support of NASA's Materials Processing in Space Program under NASA Government Order H-27354B (Properties of Electronic Materials) covering the period April 1, 1980 to March 31, 1981. The work emphasizes measurements of materials properties and thermophysical properties.

This work has been carried out in five tasks. These tasks have, as two of their focal points, the role of convection effects and the role of container effects, both of which would differ in space-based experiments from those found in ground-based experiments. The results obtained for each task are given in detailed summaries in the body of the report. The five tasks are Task 1 - Surface Tensions and Their Variations with Temperature and Impurities; Task 2 - Convection During Unidirectional Solidification; Task 3 - Measurement of High Temperature Thermophysical Properties of Tungsten Liquid and Solid; Task 4 - Thermodynamic Properties of Refractory Materials at High Temperatures; Task 5 - Experimental and Theoretical Studies in Wetting and Multi-layer Adsorption.

NBSIR 81-2295

NBS: MATERIALS MEASUREMENTS

J. R. Manning

U.S. Department of Commerce
National Bureau of Standards
Washington, DC 20234
Phone: (301) 921-3354

June 1981

U.S. DEPARTMENT OF COMMERCE, Malcolm Baidrige, *Secretary*

NATIONAL BUREAU OF STANDARDS, Ernest Ambier, *Director*

TABLE OF CONTENTS

National Bureau of Standards
Materials Measurements

Summary

This report describes NBS work for NASA in support of NASA's Materials

Processing in Space Program under NASA Government Order H-27954B (Properties

of Electronic Materials) covering the period April 1, 1980 to March 31, 1981.

The work emphasizes measurement of materials properties and thermophysical

properties important in materials processing applications.   It has two main

thrusts:

1)   Carrying out precision measurements in space and investigating the

feasibility of improved measurements when the space environment offers a

unique opportunity for performing such measurements.   These measurements

would be useful for either space processing or processes on the ground.

2)   Obtaining precision measurements on materials properties when these

properties are important to the design and interpretation of space processing

experiments.   These measurements would be carried out either in space or on

the ground.

This work has been carried out in five tasks.   These tasks have, as two

of their focal points, the role of convection effects and the role of con-

tainer effects, both of which would differ in space-based experiments from

those found in ground-based experiments.   The results obtained for each task

are given in detailed summaries in the body of the report.

Briefly, in Task 1 - Surface Tensions and Their Variations with Temperature

and Impurities - special equipment has been put into operation which, for the

first time, allows simultaneous liquid-vapor surface tension and Auger surface

concentration measurements to be made on metal liquids. This apparatus has been used to analyze surface tensions and reactions on pure gallium and a gallium-tin alloy, providing information which is important for prediction and analysis of surface processes on liquids in space flight experiments. Applications include, for example, Marangoni convection and surface segregation effects occurring during solidification. In this work, ionic bombardment sputtering with argon was found to be a very promising method for producing clean liquid surfaces, since unexpected convection currents appeared which allow rapid and efficient cleaning of carbon particles from the whole surface, or indeed the whole volume, of the liquid droplet. For gallium specimens cleaned by this method, a linear dependence of surface tension on temperature was found, in contrast to the quadratic dependence found for less clean samples. For Ga-Sn (1.9 at.%) alloys the Auger measurements showed strong temperature-dependent surface segregation of Sn to the surface. This result was consistent with the simultaneous surface tension measurements made on the alloys.

In Task 2 - Convection During Unidirectional Solidification - the succinonitrile-ethanol system is being investigated as a transparent material in which convective flows produced by simultaneous temperature and composition gradients during unidirectional solidification can be quantitatively measured and compared with theoretical predictions. Knowledge of convective conditions is important in comparing solidification in microgravity with that on earth and in evaluating the advantages of space processing. In order to determine the distribution coefficient k, the phase diagram in the low

ethanol range was determined, and k was measured as 0.044. Calculations to predict the range of convective instabilities then were made using this distribution coefficient value. It was predicted that ethanol concentrations in the range 10^{-3} to 10^{-2} weight percent can provide either convective, interfacial or oscillatory instability depending on the values of temperature gradients and solidification velocities. An apparatus has been constructed to measure convective flows in these ranges in this material, and initial baseline thermal convection measurements have been made. Velocities are determined by time lapse photography of polyvinyltoluene spheres having nearly the same density as the solidifying liquid with the spheres acting as markers in the liquid to map the convective flows.

In Task 3 – Measurement of High Temperature Thermophysical Properties of Tungsten Liquid and Solid – this task contributes to a joint effort of the General Electric Advanced Applications Laboratory (GE), Rice University (RICE) and the National Bureau of Standards (NBS) to develop levitation/drop calorimetry techniques. The immediate objective is to measure the specific heat of liquid tungsten, in order to provide key benchmark measurements on thermophysical properties. The current phase of this effort has involved completing the physical connection of the RICE calorimetric system to the GE levitation facility. In this phase, improvements have been made particularly in the temperature measurement area. A data logging system has been added to eliminate the need for a human observer of the calorimeter heat trend. This automation, along with proposed automation of the calorimeter data system, which is made necessary by the erratic levitation holding times of the molten tungsten drops, can also be expected to aid in automatic operation of similar space flight experiments.

3

In Task 4 - High Temperature Thermophysical Properties of Refractory Materials from Free Cooling Experiments - a free-cooling method for measuring specific heats of reactive and refractory materials is being developed. This method allows use of the positioning-levitation capabilities available in space to provide thermophysical measurements without contact with a container. Tests with a millisecond pulse heating system have been performed using pyroelectric radiometer devices to measure the energy radiated from the specimen. In addition, calculations have been performed to relate the surface temperature and radiated energy of spherical samples (which can be measured directly with a pyrometer and the newly developed pyroelectric radiometer devices) to the specific heat, thermal conductivity, and emissivity of the sample. Under certain conditions, it should be possible to determine the temperature dependence of these parameters from simultaneous measurements of energy radiated and temperature change during free-cooling of a levitated sample.

In Task 5 - Experimental and Theoretical Studies in Wetting and Multilayer Adsorption - ellipsometric parameters of the liquid-vapor interface between a binary C_7F_{14}-C_7H_{14} mixture and air have been measured near the predicted transition from high adsorption to low adsorption. Also a method of measuring and recording the index of refraction of this transparent binary mixture simultaneously with measurement of the ellipsometric parameters has been tested. Separate laser light sources are used for the two types of measure-ments. Since the index of refraction measurement is extremely sensitive to the appearance of macroscopic amounts of a second liquid phase, it can serve to precisely locate the miscibility gap. Thus the simultaneous measurement of both the index of refraction and the ellipsometric parameters will locate the

adsorption transition with respect to the miscibility gap in the same sample. Measurements of ellipsometric and other optical parameters will allow evaluation of wetting behavior involving immiscible materials, a topic of major significance in space processing applications.

Task 1

Surface Tensions and Their Variations
with Temperature and Impurities

S. C. Hardy
Metallurgy Division
Center for Materials Science

and

J. Fine
Surface Science Division
Center for Chemical Physics

Summary

Sessile drops of pure gallium and a gallium-tin (1.9 at.%) alloy have been studied in an Auger spectrometer. The surfaces of the drops were cleaned by heating to 500 °C and by ionic bombardment with argon. The surface tension of pure gallium cleaned in this way was found to vary linearly with temperature and could be represented by

$$\gamma = 724.1 - .0721 \, T \, (^\circ C).$$

This linear relationship is significantly different from the quadratic variation found previously for samples cleaned only by heating in vacuum and hydrogen. The difference in the two results is tentatively attributed to the presence of small carbon platelets on the surfaces of the unsputtered drops.

The segregation of tin at the surface of gallium-1.9% tin drop was measured by comparing the tin Auger line amplitudes with that of a pure tin sample with the same spectrometer settings. Although there is some uncertainty in the attenuation length and backscattering factors used in the analysis,

surface concentrations in excess of two monolayers were found at 50 °C, with a

sharp decline with increasing temperature. Surface concentrations calculated

from surface tension measurements were in general agreement with this conclusion.

Introduction

It has been widely recognized that surface tension measurements of liquid metals and semiconductors are flawed by the absence of any independent characterization of the chemical species present on the surfaces. The development of modern surface spectroscopies makes available a host of techniques which can address this gap in our knowledge of liquid surfaces, at least for some low vapor pressure materials. In previously reported work, Auger electron spectroscopy (A.E.S.) was applied to liquid gallium and provided valuable information about the state of the surface. The configuration of the spectrometer, however, did not allow the surface tension to be measured with the desired accuracy. This past year has been largely spent in the assembly and operation of an Auger instrument which does permit accurate surface tension measurements of the liquid sample.

Our initial studies of liquid gallium last year showed that the primary surface impurities were oxygen and carbon[1,2,3]. The oxygen was undoubtedly in the form of a gallium oxide and could be effectively reduced and removed by heating; the carbon, however, remained in the form of small platelets floating on the surface. In an attempt to clean a spot on the surface to obtain the spectrum of clean gallium, we sputtered a small area with argon ions using a conventional low power gun. The ion bombardment was found to generate large scale fluid flow that eventually carried all of the carbon into the ion beam where it was sputtered away. The result was a gallium surface which appeared to be perfectly clean within the measurement limits of the Auger spectrometer. Our first surface tension measurements on gallium sessile drops with surfaces cleaned by sputtering will be seen to have a different temperature dependence

9

from our previous results with thermally cleaned surfaces. This observation reinforces our feeling that the sputter cleaning process will be an important tool in future studies of liquid surfaces. We will present here our current ideas on the mechanism responsible for the fluid flow during the sputtering process.

The study of surface segregation in liquid alloys is an area which seems particularly suited to A.E.S. The comparison of directly measured surface concentrations with those deduced from surface tension values should eventually result in improved models for the interface. We have begun measurements with dilute alloys of Sn in Ga and will describe some initial results.

<u>Experimental Apparatus and Procedures</u>

The Auger spectrometer which we have assembled is a conventional single-pass cylindrical mirror analyzer system with a coaxial electron gun. The CMA is mounted vertically so that it can be focussed on the apex of a sessile drop located beneath it. This arrangement was chosen because it maximizes the fraction of the drop surface which can be analyzed by the spectrometer and provides excellent visibility for photography by locating the drop near the center of two opposing 8" view ports. The shallow cylindrical cup containing the sessile drop is clamped to a simple hot stage mounted on a horizontal manipulator which translates in three orthogonal directions. An ion gun mounted in a side port is also focussed at the drop apex. Fig. 1 shows schematically the experimental arrangement. The stainless steel bell jar in which these components are mounted is equipped with three pneumatic vibration isolation supports which are adjusted to level the cup for sessile drop surface tension measurements. The bell jar is

evacuated with sorption and ion pumps to minimize hydrocarbon concentrations. Pressures in the mid 10^{-9} torr range are achieved without baking as measured by a nude ionization gauge. High purity gases can be admitted to the bell jar from a connecting system for sputtering or oxidation studies.

The hot stage is also shown schematically in Fig. 1. The seven heaters are 0.6 mil tungsten wire spirals enclosed in alumina tubes and are pressed to the bottom of the plate which supports the cup by an opposing plate. The heater ends are shielded to prevent evaporative contamination of the sessile drop and the CMA. The cups are generally made of 0.6" O.D. silica cylinders fused to 1" diameter flat silica plates to provide a wide shoulder at the base. The body of the cup passes through a hole in a thin steel sheet which presses the cup base against the heated plate. A chromel alumel thermocouple is mounted on this pressure plate at the edge of the hole through which the cup passes. The temperatures read by this thermocouple were in agreement with those measured by a W-Rh thermocouple inserted into a sessile drop of gallium contained in the cup.

The hot stage, which is constructed of stainless steel, is mounted by three thin screws to a silica plate. This silica plate is itself attached to the platform of the manipulator and provides effective thermal isolation for the hot stage by its length and its low conductivity. Consequently, the equilibrium temperature of the stage is extremely stable. This thermal isolation, however, imposes the penalty of a slow cooling rate at low temperatures where radiation losses are small. Fig. 2 shows the equilibrium temperature of the hot stage as a function of heater current. The power source was a small variable transformer.

The use of insulating cups to contain the sessile drop requires that an electrical contact be made with the sample for Auger analysis. If this is not done, charge builds up on the sample and disrupts the operation of the CMA. It is also important to be able to measure the electron beam current in order to compare different Auger spectra. We make electrical contact to the drop with a fine W wire spot welded to a nickel rod that is rigidly held in an electrical feedthrough on the manipulator flange. For surface tension measurements, the manipulator is used to translate the drop and break contact. This is necessary to obtain an unperturbed sessile drop. This technique was also used to insert a fine thermocouple in the drop as mentioned previously.

Prior to forming a sessile drop, the bell jar was evacuated and the hot stage temperature was raised to 500 °C for about an hour. After cooling, the system was back filled with dry nitrogen gas. A small port was removed and gas allowed to flow through the system while the cup was partially filled with liquid gallium using a syringe. The port was then replaced and the system very slowly evacuated with the sorption pumps. If evacuation is too rapid the expansion of gases trapped under the gallium in the cup will expel the liquid charge. After evacuation the process is repeated to form a sessile drop large enough for surface tension measurements. Fig. 3 is a photograph of a sessile drop formed in this way.

The instrumentation for our Auger spectrometer is not yet complete. The electronics used to form a video image of the sample by rastering the electron beam over the surface were not received and have had to be reordered. The imaging of the sessile drop is important because our previous work showed that the major impurities are in the form of solid platelets floating on the surface.

Thus without the video picture we cannot tell if the 3 µm diameter spot analyzed by A.E.S. is typical of the entire surface. We have nevertheless proceeded with measurements to gain experience and explore the capabilities of the device.

Experimental Observations

a.   The Gallium Surface

As we have previously reported, (1) the surface of a newly formed sessile drop of gallium is covered by a thin solid oxide layer with a high carbon content. Fig. 4 shows the Auger spectrum of such a drop. In addition to oxygen and carbon, this spectrum shows some chlorine which comes from the HCl used in the preparation of the drop to dissolve the surface oxide. After heating to 410 °C, the oxygen and chlorine lines are gone, but the carbon is undiminished as seen in Fig. 5a. A brief sputtering (15 min.) at a beam current of 2×10^{-6} amperes eliminates the carbon, as seen in Fig. 5b. The drop, however, is not clean yet because carbon reappears on the surface after a few hours. Several sputtering and equilibration cycles are necessary before the carbon is effectively eliminated from the drop. Eventually, no carbon is detected in the spectrum taken at the apex after sitting for many days. Although we cannot yet examine for particulates with a video imager, we believe the surface to be essentially clean after this procedure. Analysis of other areas on the drop support this conclusion.

The reduction of carbon concentration in the drop by sequential sputtering and equilibration is probably evidence for volume mixing of particulates by fluid flow during ion bombardment. The impingent ions

13

remove some carbon from the surface and drive some into the gallium where it
is mixed throughout the drop by convection. Carbon is much less dense than
gallium so buoyancy will drive these small particles back to the drop apex.
A calculation using Stokes equation and a particle diameter of 10^{-4} cm gives
velocities which would clear the drop volume of carbon in several hours. This
particle diameter is in reasonable accord with measurements from video images
of the surface. Since the velocity varies as r^2, however, it is quite sensitive
to the diameter chosen, so this calculation only establishes the feasibility
of this process as an explanation for the evolution of the surface carbon
concentration.

There are a number of possible mechanisms which may account for the fluid
flow during ion bombardment: 1) temperature gradients at the surface, 2)
electrostatic forces due to surface charging, 3) surface tension gradients due
to concentration variation of impurities, 4) surface tension gradients due to
implanted argon concentration gradients, 5) surface density gradients due to
implanted argon, 6) momentum transfer from the ion beam, The first of these
seems unlikely for at least two reasons: a) an ion beam at the low power used
here does not produce a change in the drop temperature as measured by a
thermocouple immersed in the drop, b) the impact of the electron beam by
itself does not produce any mass flow even though its total power is com-
parable to that of the ion beam (10^{-3} watt). The second explanation also
seems unlikely since carbon is conductive, as is, of course, the metal
surface. Surface tension gradients due to impurity concentration gradients
should not be present for a surface which is clean except for a few isolated
particulates. The fourth and fifth mechanisms are ruled out because they

14

require a significant argon concentration in the gallium and we have never been able to detect any argon in the Auger spectra during sputtering.

The most likely explanation for the fluid flow generated by argon ion bombardment seems to be momentum transfer from the ion beam to the liquid. Although the magnitude of this momemtum transfer is small, other fluid flow phenomena such as thermocapillary convection are also driven by very small forces. The rigorous calculation of the flow generated in a sessile drop, or any fluid body, by a localized beam of ions would be a major research effort. A very approximate calculation, however, yields flow velocities which suggest this mechanism to be the one of importance. The ion beam exerts a pressure of about 4×10^{-2} dvnes/cm^2 over its impact area of 10^{-1} cm^2. If we consider the sessile drop surface under the ion beam to be a plane fluid-vapor interface and neglect fluid flow in tne vapor, the Navier-Stokes equation for an incompressible fluid gives

$$P_v - P_L = 2\eta_L \frac{\partial V_z}{\partial z} \tag{1}$$

for the velocity gradient normal to the surface. Here P_v and P_L are the pressures in the beam and in the liquid at the surface, V_z is the velocity normal to t'e surface a:.d η_L is the viscosity. For gallium, $\eta_L \cong 2 \times 10^{-2}$ poise, and using the approximate ion biam pressure calculated above gives a velocity gradient of 1 s^{-1}. Assuming a linear velocity function normal to the surface and a liquid depth of 1 cm yields a normal velocity at the tʋp surface of 1 cm/sec. Although this is admittedly a very crude approximation, the velocity calculated is large enough to suggest the beam pressure is responsible for the fluid flow.

Carbon is normally found along with oxygen in the Auger spectra of all surfaces before cleaning. Thus, it is not surprising that we find carbon on our gallium surfaces. Gallium drops contained in cups of high density graphite show intolerable carbon concentrations and it has proved impossible to eliminate carbon when using them. We presume that the surface of the cup is eroding at a rate which keeps the gallium contaminated with carbon particles. The vitreous graphite cups used in the Auger work reported last year had a much harder surface than the present cups and the gallium could be cleaned by repeated sputtering. Even with quartz cups, however, carbon is found on the surface of a freshly formed drop as shown in the spectrum of Fig. 4. We suspected that the carbon might be originating in the alcohol which is used in the preparation of the gallium before filling the syringe for cup loading. However, similar carbon concentrations were found when distilled water was used as the carrier fluid. In these experiments, a fresh gallium ingot was used and all tools and glassware were degreased with acetone and rinsed with distilled water prior to use.

In a further attempt to isolate the source of the carbon, a gallium drop wh⁴ᶜᵢₗ had been repeatedly sputtered and showed no indications of carbon after eₒᵤᵢᵗₗᵢᵇᵣᵃting for three days was exposed to air by opening a valve. On re-evacuation, the Auger spectrum showed a very large oxygen line but no carbon. Heating to 500 °C eliminated the oxygen and the spectrum looked as clean as that of a sputtered surface. After equilibrating for two days, however, a strong carbon line was measured. It does not seem likely that this carbon came from the bulk of the gallium. Rather we suspect that it may have originated in the hot filaments of the ionization gauge or the heaters. The

residual oxygen pressure due to opening the vacuum system was much higher than normal for several days as the system pumped down to the 10^{-9} torr range. This oxygen may have reacted with the carbon in the hot filaments to generate CO which accumulated on the gallium surface. However, the surface showed no oxygen after this procedure so we would have to argue that the CO decomposed on the cool gallium surface. This does occur on other metal surfaces. The origin of the carbon found on the surfaces of gallium is still unknown.

b.   The Surface Tension of Pure Gallium

The surface tension of a gallium drop which had been cleaned by sputtering is shown in Fig. 6. A number of sputtering cycles reduced the carbon concentration to the degree that none could be detected twelve hours after sputtering. The surface tension values were calculated from photographs of the drop profile using the Bashforth and Adams technique. A linear regression analysis of the data gave the following relationship:

$$\gamma = 724.1 - .0721 \ T \ (^{\circ}C) \tag{2}$$

We also show in Fig. 6 the nearly quadratic temperature dependence which we found previously for gallium which was cleaned by heating in vacuum and in hydrogen atmospheres with graphite and quartz cups. This nonlinear relationship is in good agreement with three other measurements[4,5,6]. Our present data is in fair agreement with one of the two linear relationships found previously for gallium[7] and shown in Fig. 6. Since the Auger spectrum shows the surfaces used in the present measurements are clean, we believe the nonlinear surface tension temperature dependence found in our

17

previous work and also in other laboratories may be due to solid carbon platelets distorting the sessile drops. These platelets accumulate at the apex of the drop, a uniquely important area for surface tension calculation because it is the origin from which all the altitudes are measured. Only very small distortions would be required to produce the maximum low temperature discrepancy between our two measurements of $10mJ/m^2$ at 30 °C, a difference of less than 1.5%. This explanation can only be proved by measuring a quadratically varying surface tension for a thermally cleaned drop, characterizing the carbon concentration, sputtering to eliminate the carbon, then remeasuring the surface tension. We have not done this.

c. Gallium-Tin

The first liquid Ga-Sn sample studied in the Auger spectrometer was a gallium drop containing 1.9 atomic percent tin. This alloy was chosen because measurements had shown a large reduction in its surface tension below that of pure gallium suggesting that tin was strongly adsorbed at the metal-vacuum interface. The sample, however, was contained in a graphite cup and we were unable to completely eliminate carbon from the drop by sputtering, as discussed earlier. The amplitudes of the gallium and tin Auger electron lines are sensitive to the presence of carbon so that the estimation of surface concentration is inaccurate if the surface is not clean. This problem was circumvented by recording the Auger spectrum after sputtering when the surface was free of carbon. Fig. 7 shows the Auger spectrum of the alloy drop at 30 °C and 450 °C. The amplitude of the gallium line varies little while that of the tin line decreases strongly as temperature increases. Since the amplitude of the line is roughly proportional to the concentration

18

of the species, this implies adsorption weakens with increasing temperature. This is in accord with observations of surface adsorption in other liquid alloys.

The concentration of Sn at the surface of the drop was estimated by comparing the amplitude of the dominant tin line at 430 e.v. with that from a pure tin sample using the same spectrometer settings. This procedure is not straightforward, however, because the detected Auger electrons originate from significant depths and not solely from the surface layer. The primary electron beam (200 e.v. for our measurements) penetrates deeply into the sample. The Auger electrons generated by the beam are exponentially attenuated with distance from their origins. Thus when Auger line amplitudes from surface layers are compared with those from bulk standards, this attenuation must be taken into account[8]. For an incoherent scattering model of a uniformly adsorbed layer of Sn, the intensity of the 430 e.v. Auger electrons, I^{Sn}, is given by

$$I^{Sn} = I_\infty^{Sn} \frac{1 + r_{Ga} \ (430 \ e.v.)}{1 + r_{Sn} \ (430 \ e.v.)} \left[1 - \exp \ (\frac{-m}{L}) \right]. \qquad (3)$$

Here I_∞^{Sn} is the intensity of a pure bulk tin sample, m is the layer thickness and L is the attenuation length for 430 e.v. electrons in tin. The r terms take into account the Auger electrons which arise from the backscattered primary beam; they vary with energy and atomic species. In the filled circles in Fig. 8 we show the surface coverage of tin as a function of temperature calculated with equation 3 using an attenuation length of 4 monolayers[9]. The r values for Sn and Ga at 430 e.v. were estimated to be 0.62 and 0.46

19

respectively[10]. Thus the term $\frac{1+r_{Ga}}{1+r_{Sn}}$ is approximately 0.9.

We have also measured the surface tension for the gallium-1.9% Sn drop. The data shown in Fig. 9 (filled circles on line 1) were taken after sputtering and before carbon redeveloped at the surface. Although carbon may have been located on the surface outside of the area analyzed by the electron beam, the error so introduced into the surface tension values should be small compared to the large effects of the tin adsorbed at the surface. We also show in this figure the surface tension relationship (line 4) we find for pure gallium surfaces cleaned by sputtering. For comparison some surface tension values for gallium and a gallium-2% tin alloy measured in another laboratory (ref. 6) are also presented. The results for the alloys are in fairly good agreement except below 100 °C.

The depression of the surface tension of the alloy below that of pure gallium is produced by the adsorption of tin at the liquid-vacuum interface. This adsorption is strongly temperature dependent and produces a temperature dependent surface concentration of tin, as indicated in Fig. 8. This surface concentration of tin can be estimated from the relative adsorption $\Gamma_{Sn}^{(Ga)}$. For a dilute solution this can be written as

$$\Gamma_{Sn}^{(Ga)} = -\frac{X_{Sn}}{RT} \frac{d\gamma}{dX_{Sn}} \tag{4}$$

where X_{Sn} is the bulk concentration. The coverage in monolayers is found by multiplying $\Gamma_{Sn}^{(Ga)}$ by the area of a tin molecule. In Fig. 8 we show (open circle) the surface coverage of Sn for the gallium alloy drop calculated by taking

$$\frac{d\gamma}{dX_{Sn}} = \frac{\gamma_{Ga} - \gamma_{alloy}}{X_{Sn}} . \tag{5}$$

20

These results can be compared with the surface coverages estimated from the Auger line intensities (filled circles in Fig. 8). The surface coverages are in good agreement, particularly at the lower temperatures. Given the uncertainties in attenuation lengths and backscattering factors, the agreement may be fortuitous. No effort has been made to improve the agreement of the two sets of data by adjusting these parameters. The surprising aspect of this data is that it suggests coverages in excess of a monolayer below 125 °C. It was anticipated that the coverage might reach a monolayer but would then saturate and remain constant. Large adjustments to the attenuation length, back-scattering factors, and the variation of surface tension with concentration would be necessary to reduce the coverage to below a monolayer.

In conclusion, our initial studies have shown that Auger spectroscopy can be successfully applied to liquid metals and alloys. Ionic bombardment sputtering seems to be a promising way of producing clean liquid surfaces although we have not tested the technique yet for impurities which are surface active but remain in solution. The study of segregation at liquid alloy surfaces by Auger spectroscopy combined with surface tension measurements is a promising area for future work even though attenuation lengths and back-scattering factors may not be sufficiently well known for some materials.

References

1. S. C. Hardy and J. Fine, *Materials Measurements*, NBSIR 80-2082, 1 (1980).

2. J. Fine, S. C. Hardy, and T. D. Andreadis, "Symposium on the Physics of Ionized Gases," Dubrovnik, Yugoslavia, 294 (1980).

3. J. Fine, S. C. Hardy, and T. D. Andreadis, Journal of Vacuum Science and Technology, in press.

4. O. A. Timofeevicheva and P. P. Pugachevich, Dokl. A. Kad. Nar K. SSF, $\underline{134}$, 840 (1960).

5. V. I. Nizhenko, L. P. Sklyarenko, and B. N. Evemenko, Ukrain. Khim. Zhur. $\underline{6}$, 550 (1965).

6. A. G. Nalgiev and Kh. I. Ibragimov, Zh. Fiz. Khim. $\underline{48}$, 1289 (1974).

7. Kh. B. Khokonov, S. N. Zadrmkin, and B. B. Alchagirov, Elektrokhimiya $\underline{10}$, 865 (1974).

8. M. P. Seah and W. A. Dench, Surface and Interface Analysis $\underline{1}$, 2 (1979).

9. M. P. Seah, Surface Science $\underline{40}$, 595 (1973).

10. D. M. Smith and T. E. Gallon, J. Phys. D $\underline{7}$, 151 (1974).
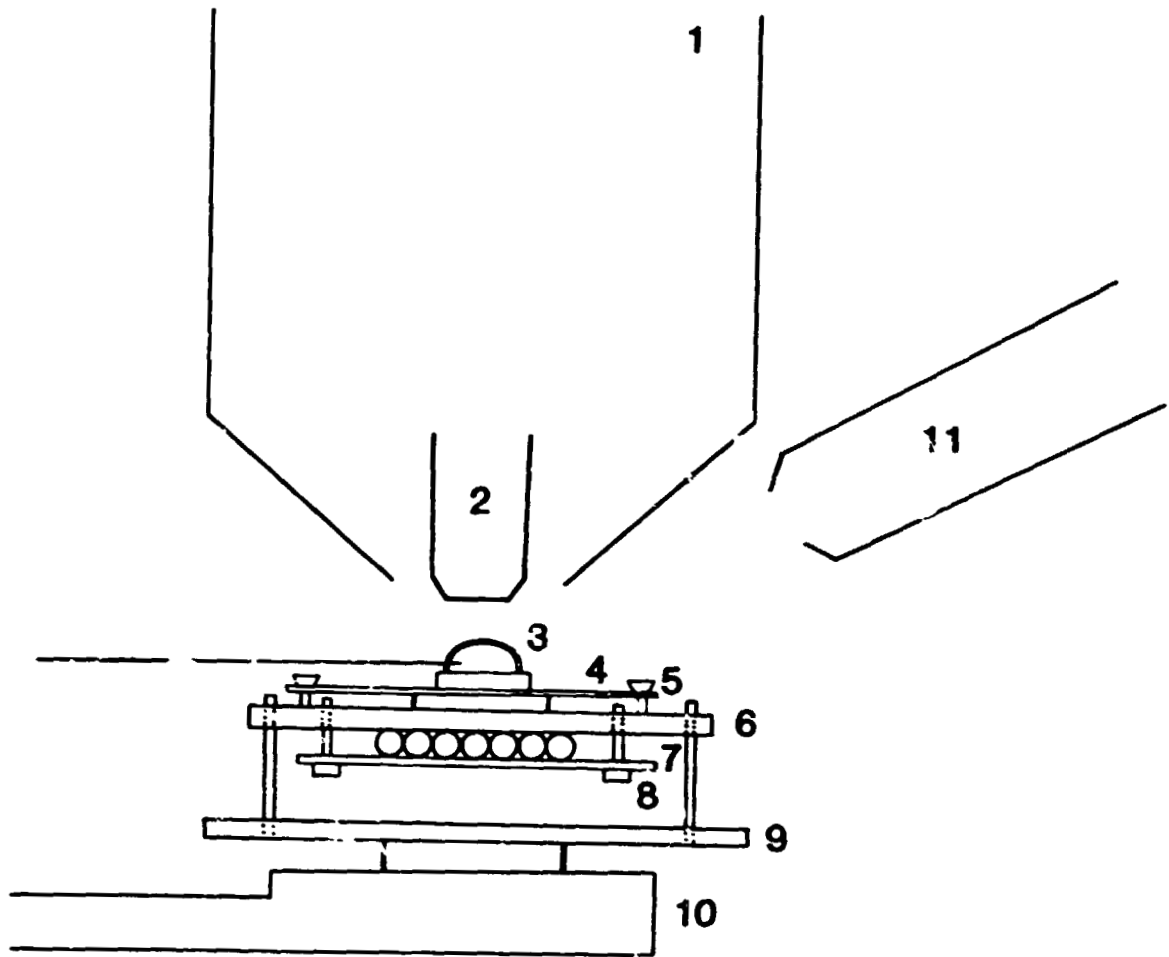
Fig. 1. Schematic diagram of experimental arrangement. 1) CMA,
2) electron gun. 3) sessile drop, 4) cup, 5) pressure plate,
6) hot stage, 7) heaters, 8) pressure plate, 9) quartz plate,
10) manipulator, 11) ion gun.

23
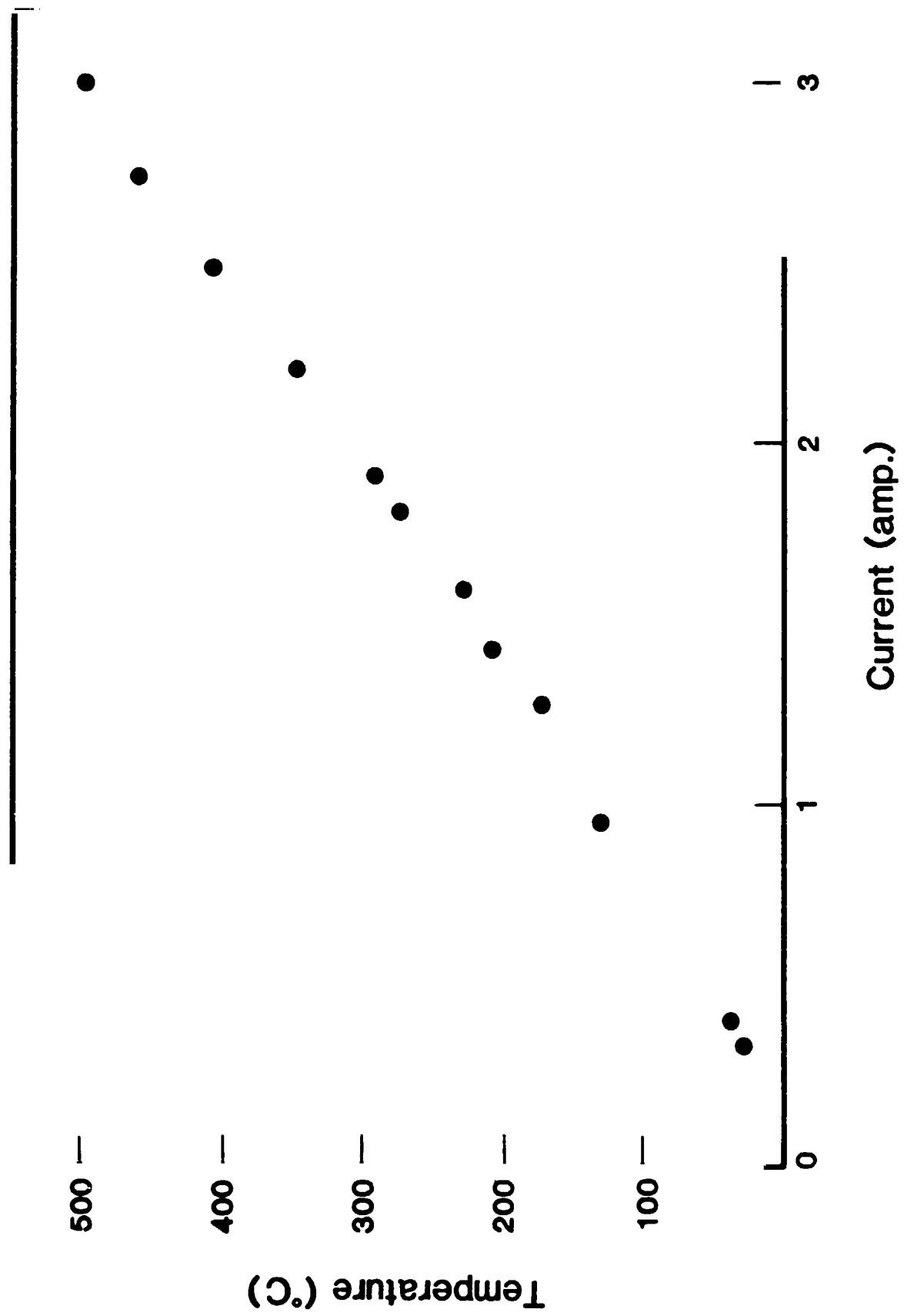
Fig. 2. The temperature of the hot stage as a function of heater current.

24

Fig. 3.   Photograph (negative) of sessile drop in Auger spectrometer.
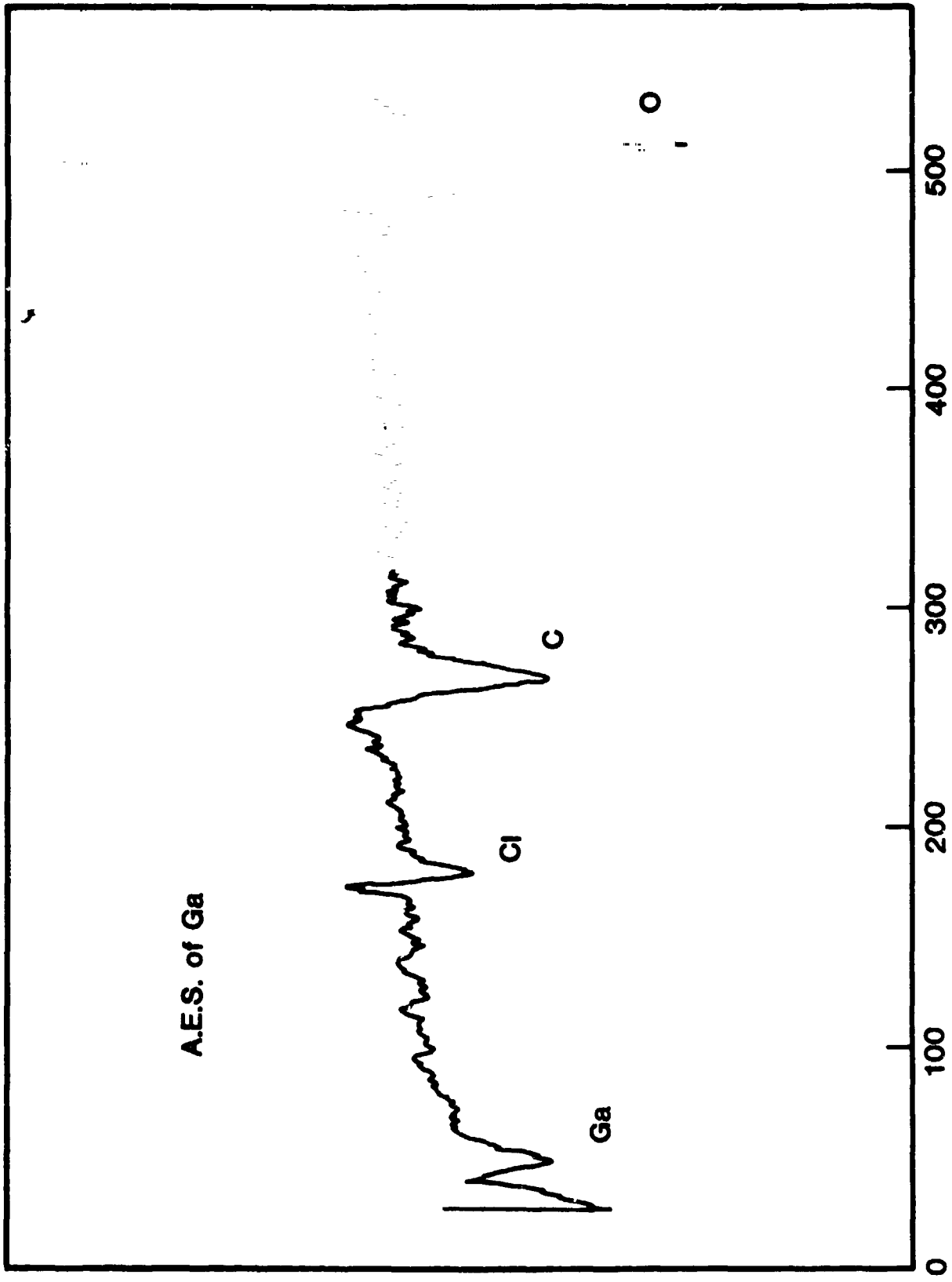
Fig. 4.   Auger spectrum of uncleaned Ga drop.
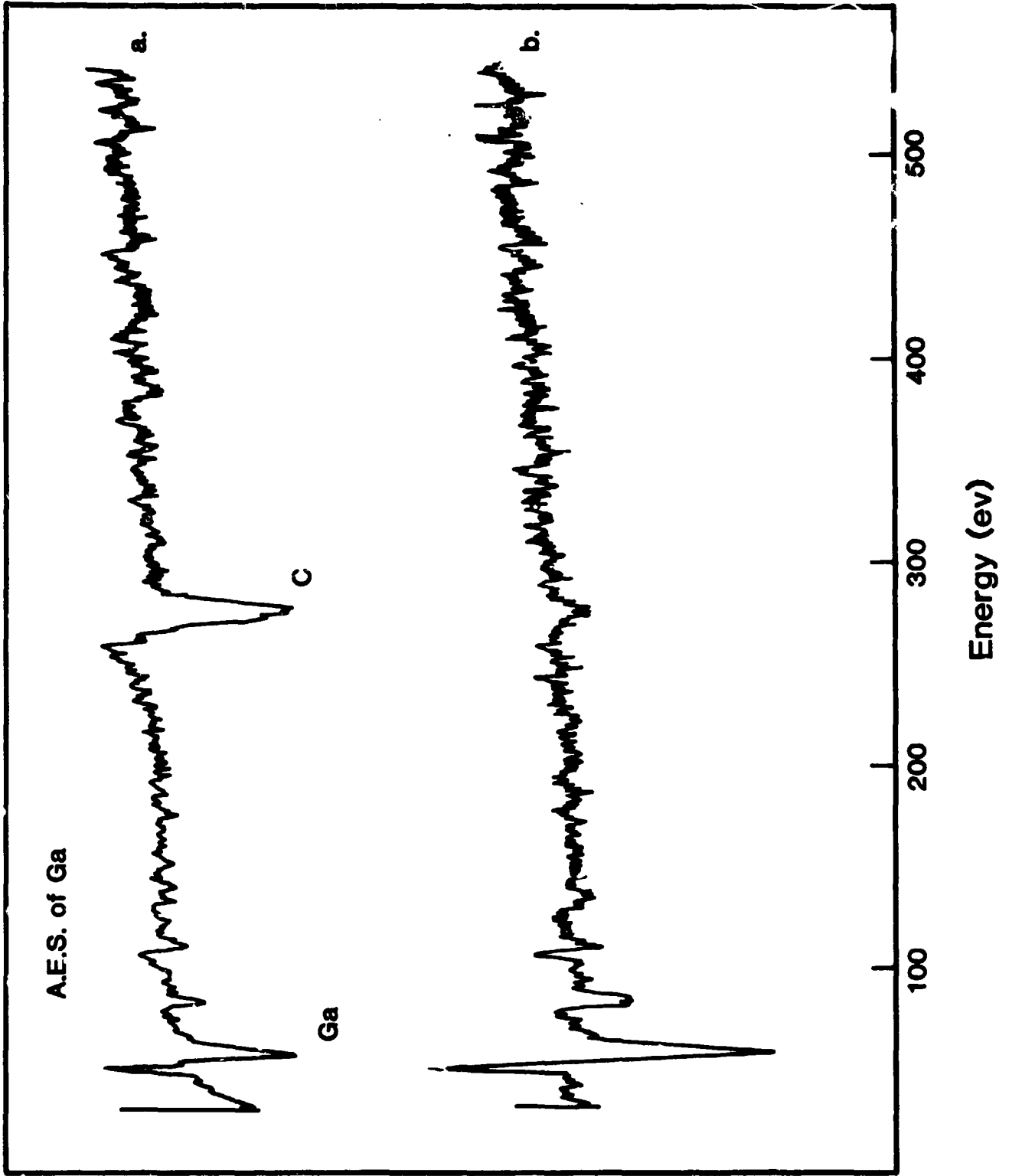
Fig. 5. Auger spectrum of Ga drop (a) after heating to 450 °C (b) after sputtering.
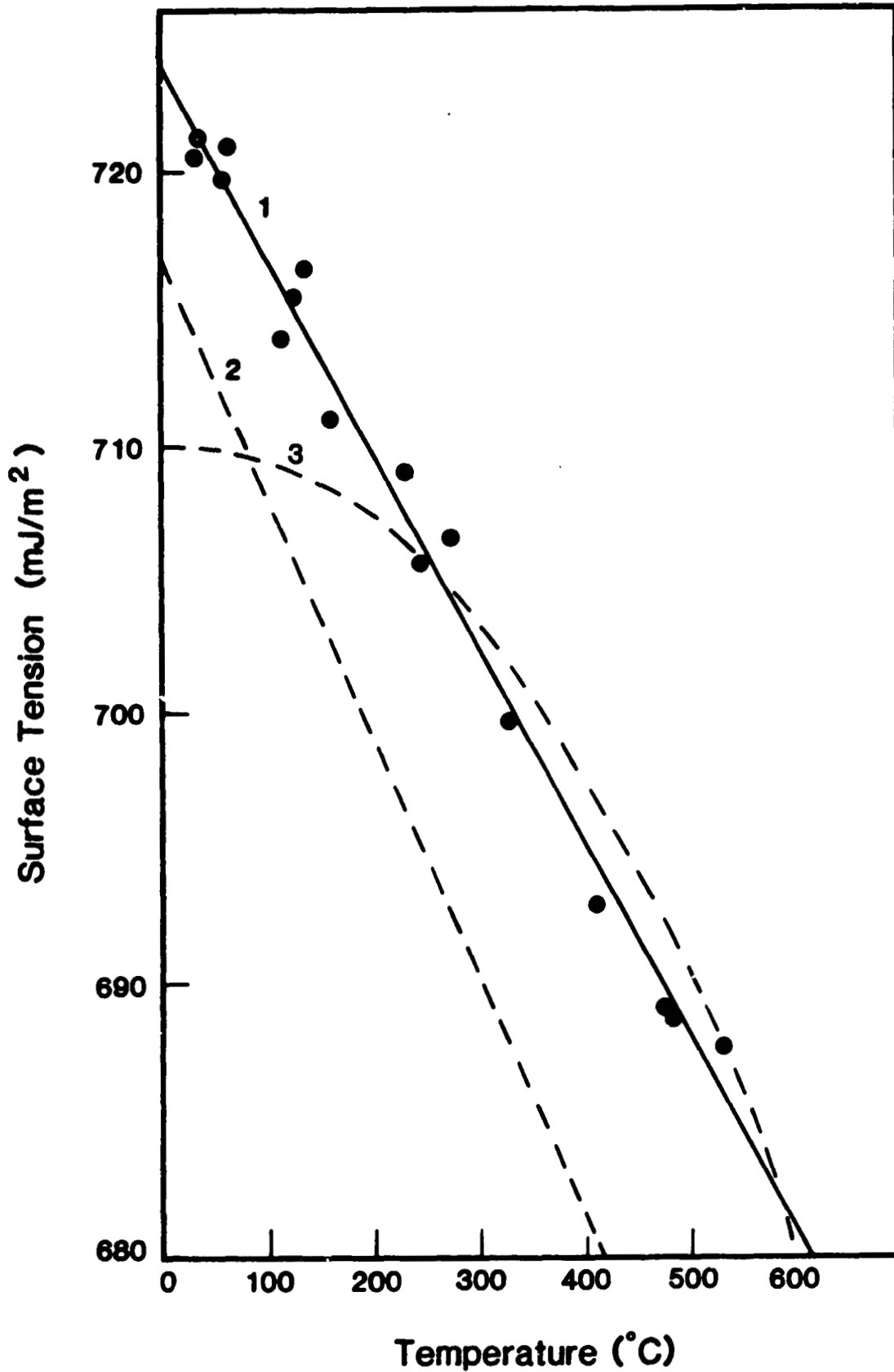
Fig. 6.   The surface tension of Ga as a function of temperature.   1) present work, 2) ref. 7, 3) ref. 1.

28
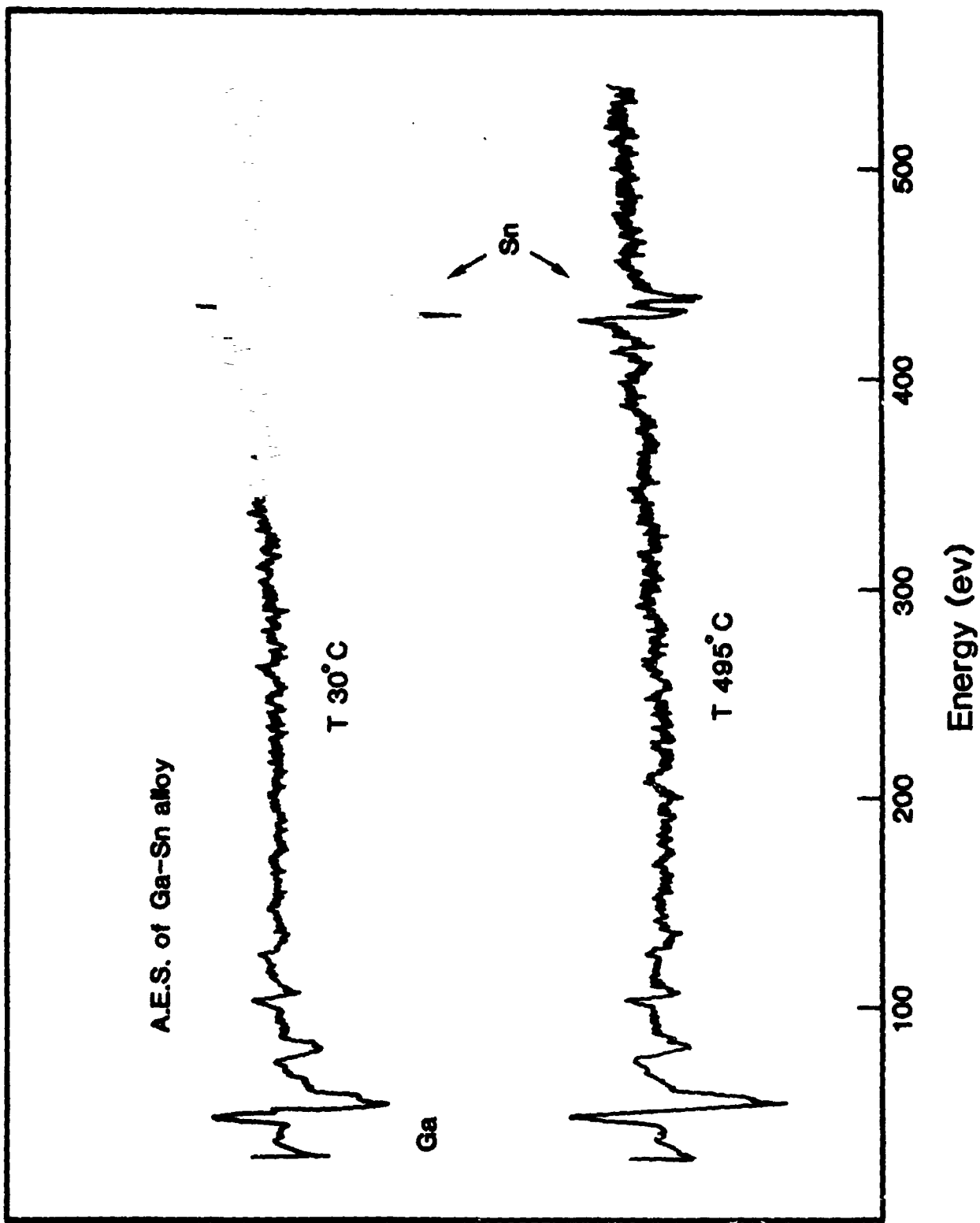
Fig. 7. The Auger spectrum of Ga-Sn 1.9 at.% at (a) 30 °C and (b) 450 °C.
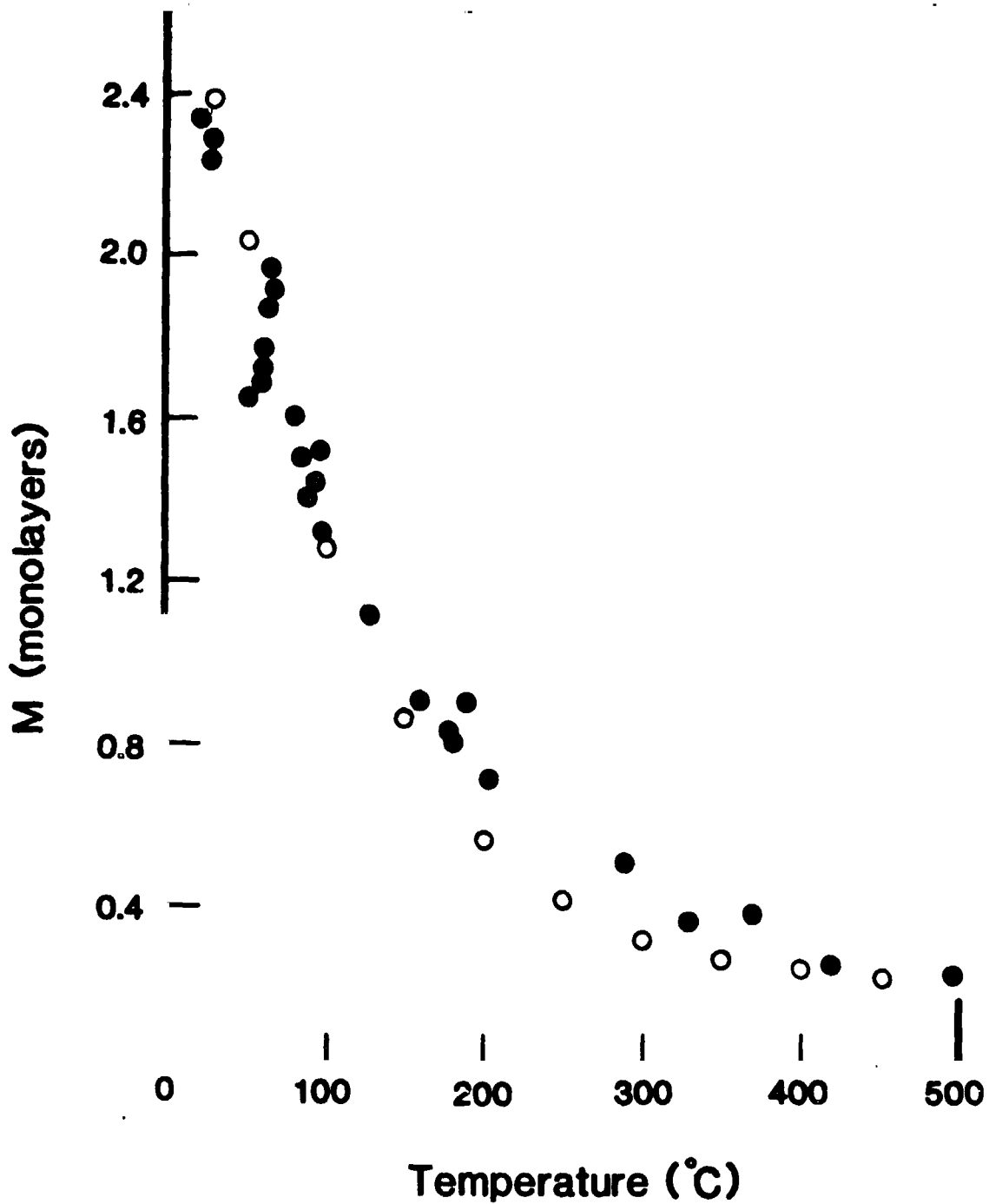
Fig. 8.   The surface coverage in monolayers of Sn as a function of temperature
as measured from line amplitudes (filled circles) and surface
tension changes (open circles).
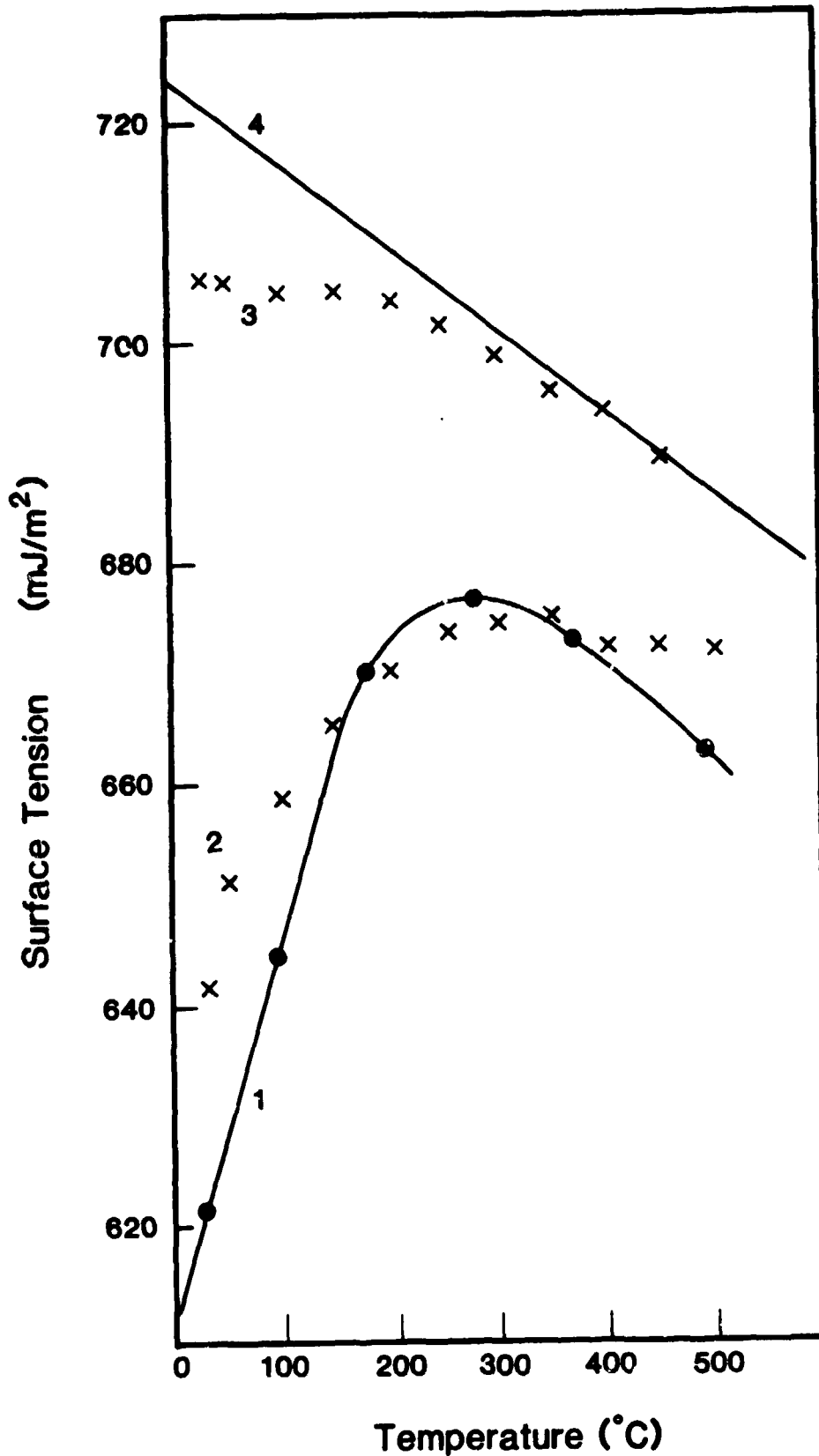
Fig. 9.   The surface tension of Ga-Sn 1.9 at.% as a function of temperature.
The filled circles along with curve (1) give measurements from the
current work.   The X's which form curve (2) are data reported in
reference 6.   Curves (3) and (4) are results for pure gallium, the
X's which form curve (3) being data given in reference 6 and the
straight line (4) being results from the present work.

Task 2

Convection During Unidirectional Solidification

S. R. Coriell and R. J. Schaefer
Metallurgy Division
Center for Materials Science

Summary

The succinonitrile-ethanol system has been selected for the experimental study of solute-induced convective and morphological instabilities. The phase diagram of this system has been determined and the measured distribution coefficient of 0.044 was used to perform stability calculations. Several modes of instability are predicted in the composition range of 10^{-3} to 10^{-2} weight percent ethanol and the solidification velocity range of 0.5 to 5 μm/sec. Experimental measurements of convective flow have used the tracking of small neutrally buoyant particles, and have to this point been devoted to measuring the background of thermally induced convection in pure succinonitrile. Flow rates of 1 to 5 μm/sec were produced in the present apparatus from thermal convection alone without solidification whereas convective flows induced by solidification processes were 15 μm/sec or more.

Introduction

During the solidification of a material containing more than one component, density differences due to chemical inhomogeneities of the liquid phase are among the several driving forces for convective flow, in the presence of a gravitational field. The onset of coupled convective and constitutional interfacial instabilities during the directional solidification of a single phase binary alloy at constant velocity vertically upwards was previously treated by a linear stability analysis and specific calculations were made for physical properties appropriate to the solidification of lead containing tin [1]. For experimental verification of this type of calculation, and to reveal the nature of the convective flow once it is initiated, it is necessary to study the solidification of transparent materials. Such materials have physical properties which differ greatly from those of metals, but similar instabilities should occur. We report here calculations and experiments on the solidification of succinonitrile containing ethanol. For the lead-tin system, we give some additional results in which the convective and interfacial instabilities are decoupled and compare these with the coupled results.

Theory

We recall that the dependence of the perturbed temperature, concentration, fluid velocity, and interface shape on the horizontal coordinates x and y and the time t is of the form $\exp [\sigma t + i(\omega_x x + \omega_y y)]$, where ω_x and ω_y are spatial frequencies. In general, the time constant σ is complex, i.e., $\sigma = \sigma_r + i\sigma_i$. If $\sigma_r > 0$ for any values of ω_x and ω_y,

the system is unstable. If $\sigma_r < 0$ for all values of ω_x and ω_y, the system is stable. We refer to instabilities corresponding to large values of $\omega = (\omega_x^2 + \omega_y^2)^{\frac{1}{2}}$ (small wavelengths, $\lambda = 2\pi/\omega$) as morphological (or interfacial) instabilities and to instabilities corresponding to small values of ω (large wavelengths) as convective instabilities.

The properties of the succinonitrile-ethanol system are given in Table I. The solute diffusion coefficient, D, in the liquid and the variation of liquid density, ρ, with solute concentration, c, have not been measured. Estimated values of these have been used in the calculations, viz., $D = 1.0 \ (10^{-5}) \ \text{cm}^2/\text{s}$ and $\alpha_c \equiv - (\partial\rho/\partial c)/\rho = 3.07 \ (10^{-3})$ $(\text{wt.\%})^{-1}$. For a temperature gradient G_L in the liquid of 10 K/cm, the critical concentrations of ethanol in succinonitrile above which instability occurs are shown in Fig. 1. The results are similar to the previous calculations on the lead-tin system, and instability occurs at concentrations of the order of 10^{-3} wt.%. For small velocities the convective instability occurs at lower concentrations than the morphological instability. The concentration for convective instability increases with velocity while the concentration for morphological instability decreases with velocity. The two curves cross at a velocity of about 3.5 μm/s. In the vicinity of this crossover, i.e., where convective and morphological occur at about the same critical concentrations, instability occurs by an oscillatory mode for which $\sigma_i \neq 0$ when $\sigma_r = 0$. The onset of instability by an oscillatory mode is the most striking difference between the results for lead-tin and succinonitrile-ethanol. Fig. 1 also shows the dimensionless ratio of the perturbation

wavelength λ at the onset of instability to the diffusion boundary layer thickness D/V. As previously noted, the wavelength corresponding to convective instability is considerably larger than the wavelength corresponding to interfacial instability. At small velocities, the convective wavelengths are quite large, e.g., λ = 5.7 cm for V = 0.5 μm/s.

The effect of the temperature gradient G_L in the 1 quid on the critical concentration for instability is shown in Fig. 2. As long as the mode of instability does not change, the critical concentration increases with increasing temperature gradient as would be expected since the temperature gradient is a stabilizing influence. However, as illustrated by the V = 3.0 μm/s data in Fig. 2, the critical concentration at G_L = 10 K/cm is larger than the critical concentration at 20 K/cm; the mode of instability changes from oscillatory convective ($\sigma_i \neq 0$) to convective ($\sigma_i = 0$) as the gradient increases. For V = 4.0 μm/s, the r de of instability changes from morphological to oscillatory convective to convective as the temperature gradient increases from 10 to 40 K/cm.

These changes in the mode of instability are illustrated in detail in Figs. 3-6, which give the concentration at which σ_r = 0 as a function of the spatial frequency ω of the sinusoidal perturbation for G_L = 10 μ/cm and V = 2.5, 3.0, 3.5, and 4.0 μm/s, respectively. The solid lines correspond to σ_i = 0, while the dashed lines correspond to $\sigma_i \neq 0$; the values of σ_i are indicated by the lower curves in the figures. At V = 2.5 μm/s, the smallest concentration corresponds to a non-oscillatory convective mode whereas at V = 3.0 and 3.5 μm/s an oscillatory convective mode occurs with σ_i in the range 10^{-2} to 10^{-3} s^{-1}. At V = 4.0 μm/s, instability first occurs by a morphological mode with c_∞ = 4.66 (10^{-3}) wt.%

and $\omega = 140$ cm^{-1} (not shown in the figure).

Since the liquid diffusion coefficient D has not been measured, some calculations were carried out with a different value of D. For D = 5 (10^{-6}) cm^2/s and $G_L = 10.0$ K/cm, the critical concentrations are 2.09 (10^{-4}), 5.06 (10^{-4}), and 3.46 (10^{-3}) wt.% for V = 0.5, 1.0, and 2 0 μm/s, respectively. The highest velocity corresponds to an oscillatory convective instability with non-oscillatory convective instability occurring at the lower velocities. For comparison, for D = 1.0 (10^{-5}) cm^2/s and $G_L = 10.0$ K/cm, the critical concentrations are 2.63 (10^{-4}), 4.58 (10^{-4}), and 1.20 (10^{-3}) wt.% for V = 0.5, 1.0, and 2.0 μm/s, respectively. Thus, the critical concentration curves (as function of velocity) for the two different diffusion coefficients cross each other. The critical concentration for morphological instability is proportional to D for small velocities, and hence decreases with decreasing D.

In order to obtain an estimate of the rate at which instabilities develop, linear stability calculations of σ for a fixed concentration of ethanol were carried out. For D = 1 (10^{-5}) cm^2/s, $G_L = 10$ K/cm, and $c_\infty = 10^{-2}$ wt.%, and crystal growth velocities of 1.0, 2.0, and 4.0 um/s, the maximum values of σ_r for convective instability are 4.9 (10^{-2}), 3.7 (10^{-2}), and 6.6 (10^{-3}) s^{-1} at spatial frequencies of 22, 24, and 28 cm^{-1}, respectively. For V = 2.0 and 4.0 μm/s, the maximum values of σ_r for morphological instability are 1.1 (10^{-2}) and 0.12 s^{-1} at spatial frequencies of 440 and 950 cm^{-1}, respectively. For V = 1.0 μm/s, the system is morphologically stable, i.e., the maximum value of σ_r for morphological instability is negative. For example, at V = 1.0 μm/s,

the amplitude of the convective instability will increase by a factor of ten in 50 s; during this time the crystal will grow 0.005 cm.

In order to gain some insight into the interaction between convective and morphological instabilities, we have modified certain parameters in the calculations so that only one type of instability can occur. Physical parameters appropriate to the solidification of lead containing tin were used with $V = 40.0$ μm/s and $G_L = 200$ K/cm. If the gravitational acceleration g is identically zero, then convection does not occur and only morphological instabilities are possible. The critical concentration of tin as a function of the spatial frequency ω of a sinusoidal perturbation with $g = 0$ is shown in Fig. 7; the minimum value of c_∞ is 0.215 wt.% at $\omega = 690$ cm^{-1}. By requiring that the solid-liquid interface not deform, we can eliminate the morphological instability and allow only convective instabilities. The boundary conditions at the solid-liquid interface are based on con-servation of enthalpy and solute and a relationship between freezing point and solute concentration. In order to simultaneously satisfy these three boundary conditions, the solid-liquid interface must be free to deform. If we require a planar interface, one of the boundary con-ditions can not be satisfied. We have required that the interface be rigid (planar) and satisfied the conservation laws but ignored the relationship between freezing point and solute concentration. The critical concentration as a function of ω for this rigid interface model is shown in Fig. 8; the minimum value of c_∞ is 0.15 wt.% at $\omega = 45$ cm^{-1}. The results for the coupled problem, i.e., $g = 980$ cm/s^2 and interface free to deform is shown in Fig. 9. The minimum value of c_∞ is 0.136 wt.% at

$\omega = 45\ cm^{-1}$ for convective instability while the minimum for the morphological instability is essentially identical to that computed with $g = 0$. While there is a 25% difference in the critical concentrations for convective instability between the rigid and free interface, the most striking difference between Fig. 9 and Figs. 7 and 8 are the appearance of oscillatory modes ($\sigma_i \neq 0$) in the coupled problem. These oscillatory modes are apparently the result of the coupling between the convective and morphological instabilities, and would not be expected in the absence of this coupling. Oscillatory modes do arise in double diffusive convection, but in the simple models which can be treated analytically, only when the temperature field is destabilizing and the solute field stabilizing, which is not the case treated here. The calculations for the succinonitrile-ethanol system have indicated that the onset of instability can occur by an oscillatory mode.

The main theoretical effort of this task is now directed toward developing mathematical models of the fluid flow and resultant solute segregation under conditions for which the linear analysis predicts convective instability; this research is being carried out in collaboration with R. G. Rehm of the Mathematical Analysis Division. Numerical algorithms are being developed and implemented to solve the time dependent partial differential equations for fluid flow and heat and mass transfer in two spatial dimensions with a planar solid-liquid interface.

During the past year, a paper "Effect of Gravity on Coupled Convective and Interfacial Instabilities During Directional Solidification," by S. R. Coriell, M. R. Cordes, W. J. Boettinger and R. F. Sekerka, was

presented at the XXIII COSPAR meeting and will be published in the proceedings. An article, "Solutal Convection Induced Macrosegregation and the Dendrite to Composite Transition in Off-Eutectic Alloys," by W. J. Boettinger, F. S. Biancaniello, and S. R. Corieli, which describes previous work of this project, has been published in Metallurgical Transactions [2].

Experimental Procedures

Because no methods are available for the detailed measurement of fluid flow patterns in liquid metals, a transparent system is used. Succinonitrile is chosen as the major constituent because of its metal-like solidification behavior and well-characterized physical properties (Table I). Extremely high purity can be attained in this substance by multiple distillation and zone refining [3]. Unfortunately, it has a rather low density, so the choice of solutes having lower density is extremely limited. Ethanol has been selected for this purpose on the basis of its low density, relatively high boiling point compared to other low density materials, and similarity of molecular structure to succinonitrile.

For input to the stability calculations we need to know the succinonitrile-rich end of the succinonitrile-ethanol phase diagram. This was determined by observations of samples immersed in a stirred water thermostatic bath. Temperatures were measured with precision thermometers on which temperature differences as small as 0.002 K can be read. The temperatures are not known with comparable precision on an

absolute scale, but only the accurate temperature differences are important for this experiment. The succinonitrile-ethanol system has a liquid-phase miscibility gap, as does succinonitrile with several other alcohols. The liquidus curve (Fig. 10) was determined from samples weighed out and sealed under air. A monotectic point was found at approximately 11 °C and 23 wt.% ethanol. The miscibility gap is rather low but was not studied in detail because the region of interest lies at very low concentrations of ethanol. The liquidus curve is essentially linear at concentrations of ethanol of less than 6 wt.%, and its slope in this region is 3.6 K/wt.%.

The solidus curve is very steep and its determination could only be carried out with samples held under vacuum, because dissolved air acts as a significant impurity. Such samples are difficult to prepare with accurate compositions because the vapor pressure of ethanol is high at the melting point of succinonitrile. Therefore, the apparatus shown in Fig. 11 is employed. Zone-refined succinonitrile is first loaded into the larger chamber, melted and frozen several times with active pumping to remove all dissolved air, and this side of the chamber is then hermetically sealed. The mass of the succinonitrile is determined by weighing. Ethanol is then loaded into the capillary chamber and part of it is frozen unidirectionally by lowering the capillary into a bath of liquid nitrogen. This side of the chamber is then evacuated and sealed.

Additions of ethanol to the succinonitrile are carried out by opening the teflon valve and gently applying heat to the top of the ethanol column to distill over a small amount. An estimate of the

amount transferred is obtained by noting the drop in the ethanol level in the capillary. A more accurate measure of the concentration of ethanol is obtained from the measured liquidus temperature (the temperature at which only a minute fraction of the sample remains solid, and the solid is neither melting nor freezing). The concentrations determined by these two methods agreed well. The solidus temperatures were determined as the lowest temperature at which melting was first observed (at grain boundaries) after the sample had been homogenized by rapid freezing. The results of these experiments are shown in Fig. 12, and the slope of the solidus curve is found to be 81 K/wt.%.

The distribution coefficient k_o is a key parameter in the theory of solutal convection since this coefficient determines the proportion of solute rejected at a solidifying interface. With the above data, this parameter can be calculated from the ratio of the liquidus slope to the solidus slope at small solute concentrations to be $k_o = 0.044$.

To investigate the convective and interfacial instability of succinonitrile-ethanol solutions, the calculations have indicated that one should grow crystals in the solidification velocity range 0.5 to 10 μm/s. For these experiments the sample is sealed in a round pyrex tube, 19 mm in diameter. This tube is drawn downward at the desired velocity through the apparatus shown in Fig. 13. This apparatus contains an upper water jacket, maintained at a temperature above the melting point of succinonitrile, and a lower jacket maintained below the melting point. Between these reservoirs, the round sample tube is enclosed in a fluid-filled jacket with flat glass walls. The fluid in this jacket is a mixture of water and ethylene glycol having a refractive index such that the optical distortion of the material within the round sample tube is minimized [3]. The upper and lower water jackets are maintained by circulating controllers

at temperatures constant within ± 0.001 K. The apparatus is heavily insulated and the sample is viewed in the region of the solid-liquid interface through small double-walled glass windows.

Convection is measured by photographic tracking of the motion of small particles suspended in the liquid. Laser Doppler Velocimetry (LDV) was considered as a measurement technique but rejected because at the extremely slow flow velocities (down to 1 μm/s) expected in these experiments, the LDV technique would be overly sensitive to mechanical vibration and electronic noise, and because it is more important for these experiments to determine the overall pattern of the flow than to obtain statistical information on velocities at a fixed point in space, as one normally does with the LDV method.

The particles used for tracking the fluid flow are polyvinyltoluene spheres 2.02 μm in diameter. The small difference between the density of these spheres and that of the liquid succinonitrile, together with their small size, results in a rate of gravitational precipitation calculated from Stokes Law to be 0.05 μm/s, so that the spheres follow almost perfectly the flow of the liquid. The particles are readily visible through a microscope, when illuminated by low-angle dark field illumination. Photographs are recorded with exposure times usually between 30 seconds and 2 minutes, to give adequate travel distance for flow rate measurements. The particles are illuminated by a microscope light, with a heat-absorbing solution in the optical path to prevent radiant heating of the specimen.

Experimental Results

During slow solidification, the particles are pushed by the solid/liquid interface, often accumulating in the small grooves which are present where grain boundaries intersect the solid/liquid interface.

43

When the particles accumulate into large clusters, or when the interface velocity becomes rapid, the particles are incorporated into the solid. No quantitative measurements of this effect have been recorded, and it does not interfere with the convection measuremencs. Convection measurements to date have used a sample of ultra high purity succ_nonitrile in which all convection must be attributed to thermal effects. This sample was prepared by the same techniques which were previously found [3] to reduce the level of impurities to approximately 5×10^{-7} to 5×10^{-8} mole fraction. The melting and solidification of this sample shows no indication of irpurities, such as grain boundary melting or morphological instability. The objective of the measurements with the high purity sample is to establish a baseline of residual thermally-induced convection to which convection in ethanol-doped samples can be compared.

When the temperature reservoirs of the crystal growth apparatus ᵔre adjusted to give a gradient of about 10 K/cm in the liquid, and the sample tube is held stationary (no crystal growth), the solid-liquid interface is planar and horizontal, and convective flow rates in the liquid are generally found to be in the range of 1-5 μm/ᵤ. The flow pattern is somewhat erratic. An occasional source of higher flow rates under these conditions was seen when a large void, which had originated as a shrinkage cavity when the sample was originally solidified, migrated vertically upward through the solid under the influence of the temperature gradient. Shortly before this void reached the solid-liquid interface (where it collapsed), it was seen to have an influence on the convective flow field such that there was a visible upward flow of the liquid above

the void. The thermal distortion which produced this flow, however, was not sufficient to produce a measurable distortion of the solid-liquid interface.

When a stationary sample is suddenly repositioned downward, crystal growth starts almost immediately, with the most rapid growth along the tube walls. As expected, convective flow is greatly accelerated. Several hours are required before the interface returns to its original position and the convective flow again diminishes to velocities characteristic of stationary samples. When the sample was displaced 1 cm, the flow rate along the sample axis was 20 μm/s at 40 minutes after the displacement. The flow pattern was a steady flow upward along the sample axis and downward along the walls.

When the mechanism for pulling the sample downward at constant velocity is activated, the solid-liquid interface moves downward and eventually reaches a new steady-state position. Typically 2-3 hours are required before the interface position becomes effectively stationary. In addition, the interface changes from the planar horizontal configuration to an upwardly concave shape. For a sample which was drawn downward at a velocity of 2 μm/s, convective flow rates were found to increase as the interface became more concave, so that one hour after the tracking mechanism was started, flow rates were 15-20 μm/s.

Although the convective flow during constant velocity growth is too small to be readily visible to the eye when viewed through the microscope, it is desirable to modify the apparatus such that this purely thermal effect is minimized. To this end, experiments will be carried

out with auxiliary heaters in the index-matching fluid so that the discontinuity of temperature gradient induced by the latent heat of fusion can be approximated in this fluid. Experiments with ethanol-doped samples will be commenced to determine the relative magnitude of the flow rates in pure and doped samples. Simultaneously improvements in sample illumination will be sought which can reduce the intensity of light scattered from extraneous sources such as the chamber walls and thus allow a much wider range of velocity measurements from a single exposure.

Acknowledgments

References

1. S. R. Coriell, M. R. Cordes, W. J. Boettinger, and R. F. Sekerka, J. Crystal Growth 49, 13 (1980).

2. W. J. Boettinger, F. S. Biancaniello, and S. R. Coriell, Met. Trans. 12A, 321 (1981).

3. R. J. Schaefer, M. E. Glicksman, and J. D. Ayers, Phil. Mag. 32, 725 (1975).

4. C. A. Wulff and E. F. Westrum, J. Phys. Chem., 67, 2376 (1963).

5. M. J. Timmermans and Mme. Hennaut-Roland, Journal de Chimie Physique, 34, 693 (1937).

6. H. Fontaine and M. Bee, Bull. Soc. Franc. Mineral. Crystallogr., 95, 441 (1972).

7. R. M. MacFarlane, E. Courtens, and T. Bischofberger, Mol. Cryst. Liq. Cryst., 35, 27 (1976).

8. M. E. Glicksman, R. J Schaefer, and J. D. Ayers, Met. Trans., 7A, 1747, (1976).

Table I. Properties of Succinonitrile

Property	Symbol	Value	Ref.
Molecular Weight	W	80.092	4
Density of Solid	ρ_s	1016kg/m^3**	4*
Density of Liquid	ρ_ℓ	988kg/m^3**	5
Thermal Expansivity of Solid	α_s	$-5.6 \times 10^{-4}/\text{K}$	6
Thermal Expansivity of Liquid	α_ℓ	$-8.1 \times 10^{-4}/\text{K}$	5*
Shear Viscosity	η	$2.6 \times 10^{-3} \text{Pa-s}$**	5
Kinematic Viscosity	ν	$2.6 \times 10^{-6} \text{m}^2/\text{s}$**	***
Surface Tension (Liquid-Vapor)	$\gamma_{\ell V}$	46.78mJ/m^2	5
Surface Tension (Solid-Liquid)	$\gamma_{s\ell}$	8.9mJ/m^2	3
Refractive Index (Solid)	n_s	1.4340**	7
Refractive Index (Liquid)	n_ℓ	1.4150**	7
Equilibrium Temperature (Triple Point)	T_E	331.23K	8
Latent Heat of Fusion	L	$4.70 \times 10^4 \text{J/kg}$	4
Entropy of Fusion	ΔS	$1.42 \times 10^2 \text{J/kgK}$	4
Heat Capacity of Solid	C_{Ps}	1913J/kgK**	4
Heat Capacity of Liquid	$C_{P\ell}$	2000J/kgK**	4
Thermal Conductivity of Solid	k_s	0.225J/mKs**	3
Thermal Conductivity of Liquid	k_ℓ	0.223J/mKs**	3
Thermal Diffusivity of Solid	κ_s	$1.16 \times 10^{-7} \text{m}^2/\text{s}$**	***
Thermal Diffusivity of Liquid	κ_ℓ	$1.12 \times 10^{-7} \text{m}^2/\text{s}$**	***
Unit Supercooling	$L/C_{P\ell}$	23.5 K	***
Distribution Coefficient for Ethanol in Succinonitrile	k_o	0.044	****
Liquidus slope for Ethanol in Succinonitrile	m_ℓ	3.6K/wt.%	****
Solidus slope for Ethanol in in Succinonitrile	m_s	81K/wt.%	****

* Indicates value derived from properties given in cited reference.
** Indicates value of property at melting point, 331.23K.
*** Indicates property derived from other properties in the table.
****Indicates properties measured in current work.
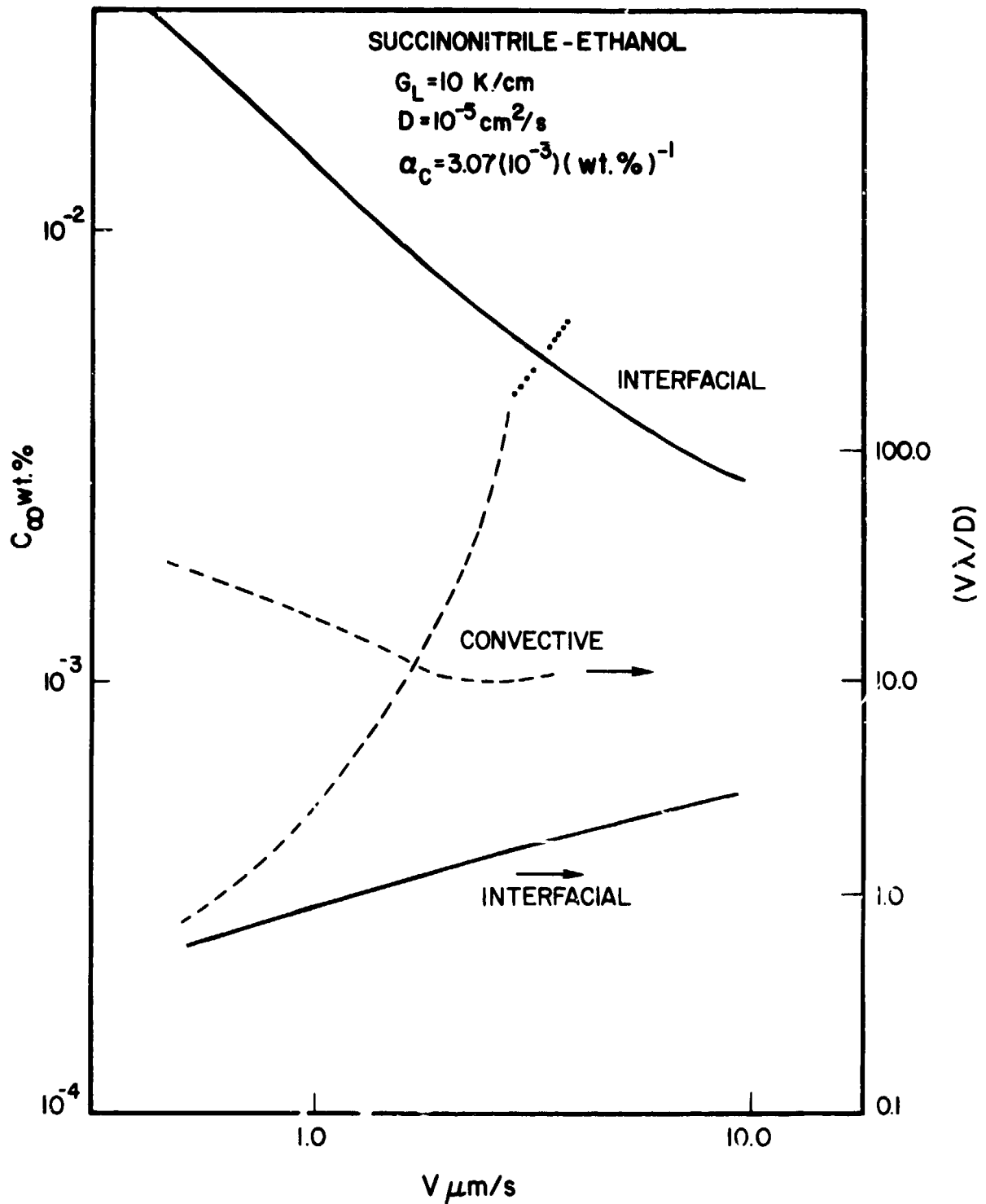
Fig. 1. The critical concentration c_∞ of ethanol in succinonitrile above which instability occurs as a function of the velocity V of directional solidification for a temperature gradient in the liquid of 10 K/cm. The ratio of the instability wavelength, λ, to the diffusion boundary layer thickness, D/V, is also shown. The solid and dashed lines correspond to interfacial and convective instabilities, respectively, while the dotted line denotes an oscillatory convective instability.
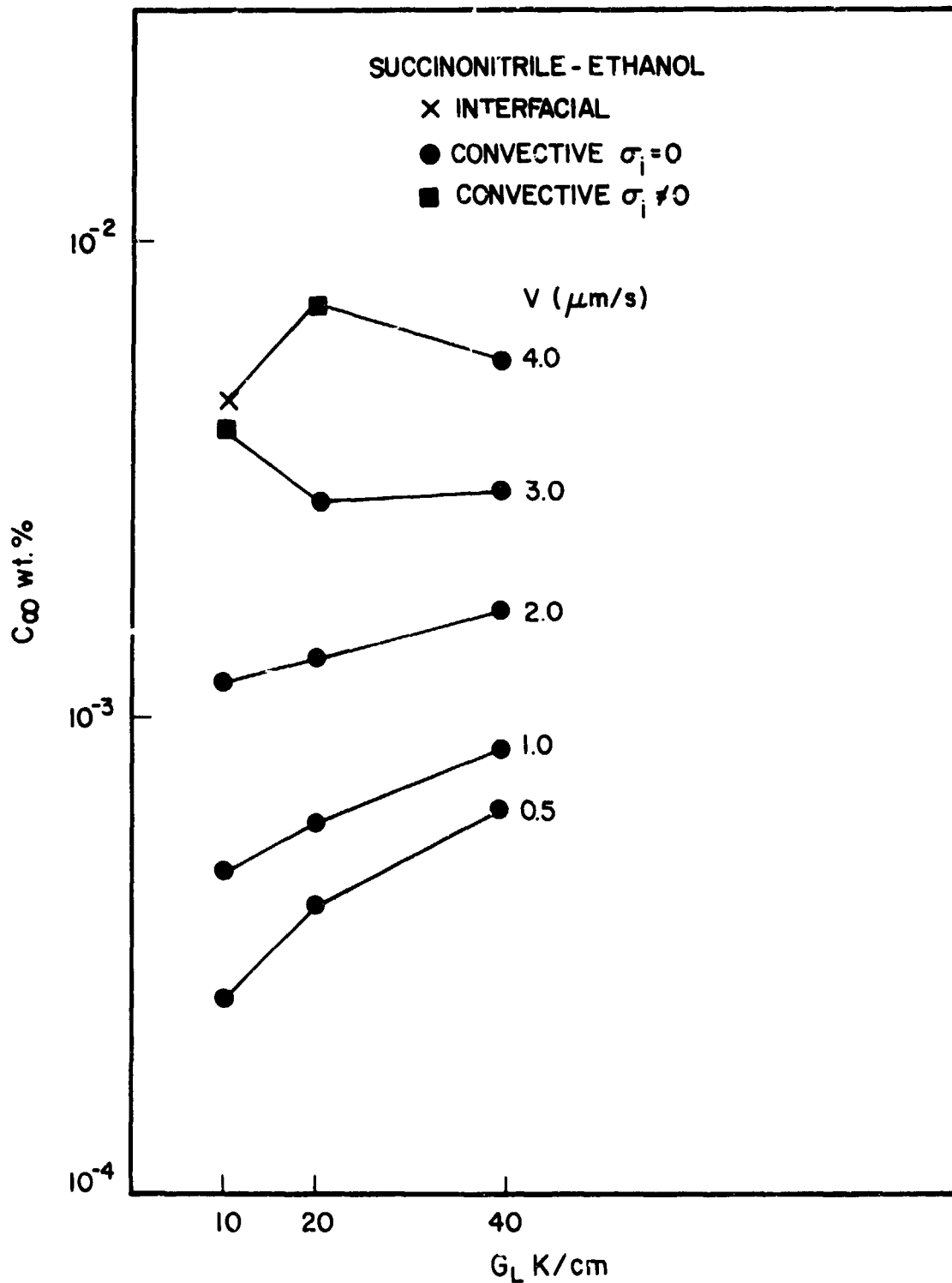
Fig. 2. The critical concentration of ethanol in succinonitrile above which instability occurs for crystallization velocities of 0.5, 1.0, 2.0, 3.0, and 4.0 μm/s, and temperature gradients in the liquid of 10.0, 20.0, and 40.0 K/cm. The x, circles, and squares indicate morphological, convective, and oscillatory convective instabilities, respectively.

Fig. 3.   The concentration of ethanol in succinonitrile at the onset of
instability during directional solidification at V = 2.5 μm/s as
a function of the spatial frequency ω of a sinusoidal perturbation.
The solid curves mark the onset of non-oscillatory instabilities
(σ_i=0); whereas the dashed curves mark the onset of oscillatory
instabilities (the value of σ_i is given on the right hand side).
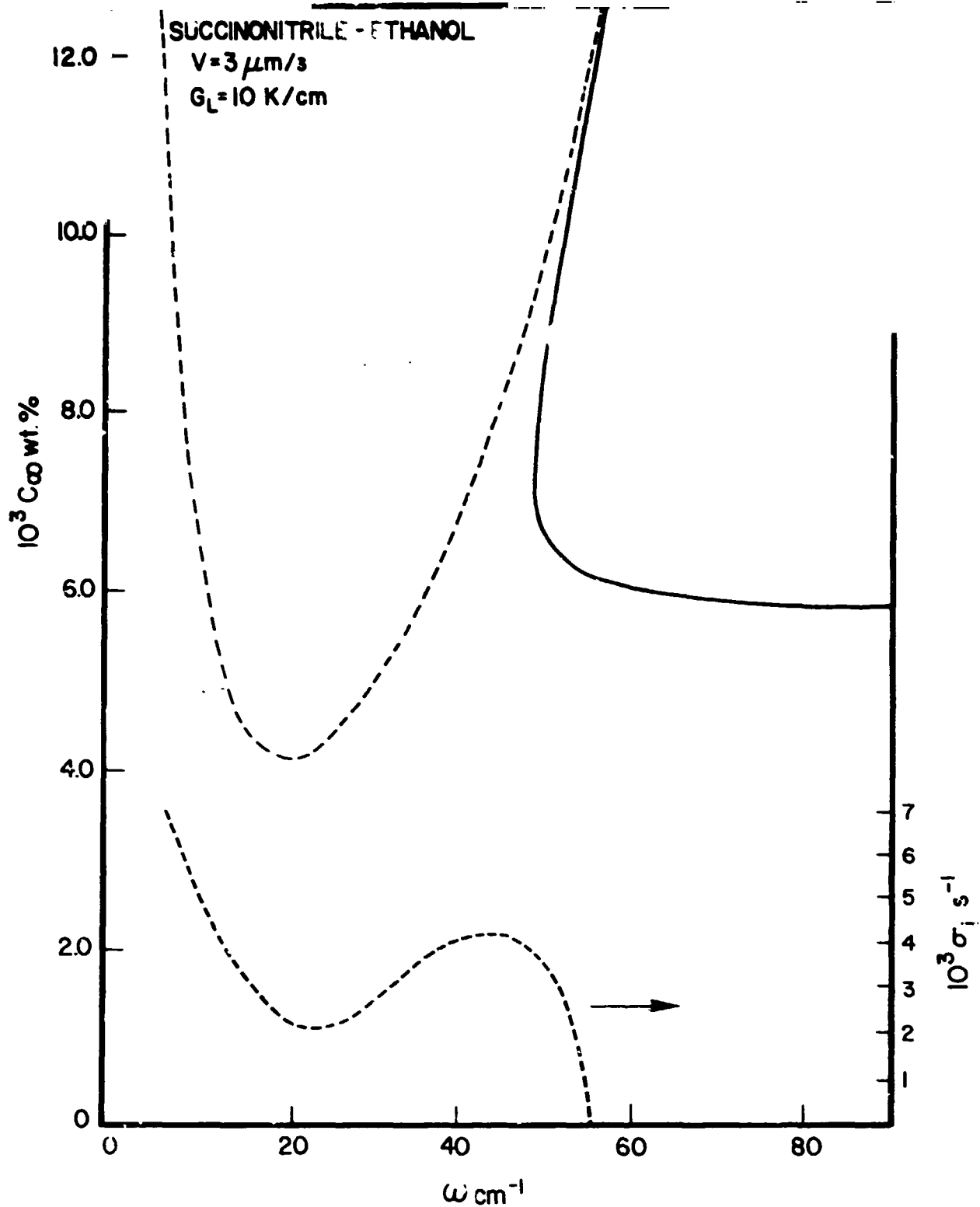
Fig. 4. The concentration of ethanol in succinonitrile at the onset of
instability during directional solidification at $V = 3.0$ μm/s as
a function of the spatial frequency ω of a sinusoidal perturbation.
The solid curves mark the onset of non-oscillatory instabilities
$(\sigma_i = 0)$; whereas the dashed curves mark the onset of oscillatory
instabilities (the value of σ_i is given on the right hand side).

Fig. 5. The concentration of ethanol in succinonitrile at the onset of
instability during directional solidification at V = 3.5 μm/s as
a function of the spatial frequency ω of a sinusoidal perturbation.
The solid curves mark the onset of non-oscillatory instabilities
(σ_i=0); whereas the dashed curves mark the onset of oscillatory
instabilities (the value of σ_i is given on the right hand side).

Fig. 6. The concentration of ethanol in succinonitrile at the onset of
instability during directional solidification at $V = 4.0$ μm/s as
a function of the spatial frequency ω of a sinusoidal perturbation.
The solid curves mark the onset of non-oscillatory instabilities
($\sigma_i = 0$); whereas the dashed curves mark the onset of oscillatory
instabilities (the value of σ_i is given on the right hand side).

54

Fig. 7. The concentration of tin in lead at the onset of instability during directional
solidification at V = 40.0 μm/s as a function of the spatial frequency ω of a
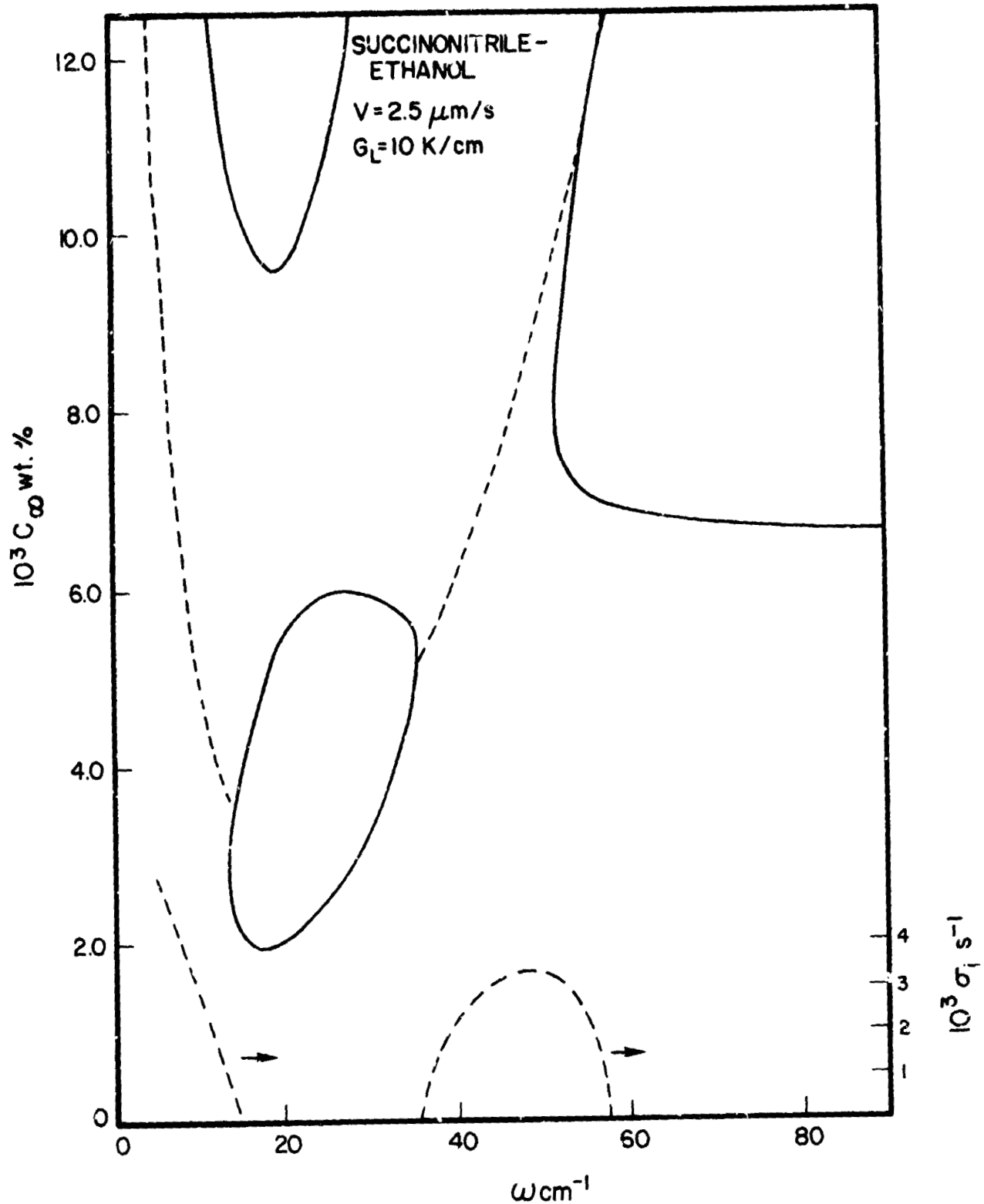sinusoidal perturbation. The gravitational acceleration g = 0 so that only
morphological instability can occur.
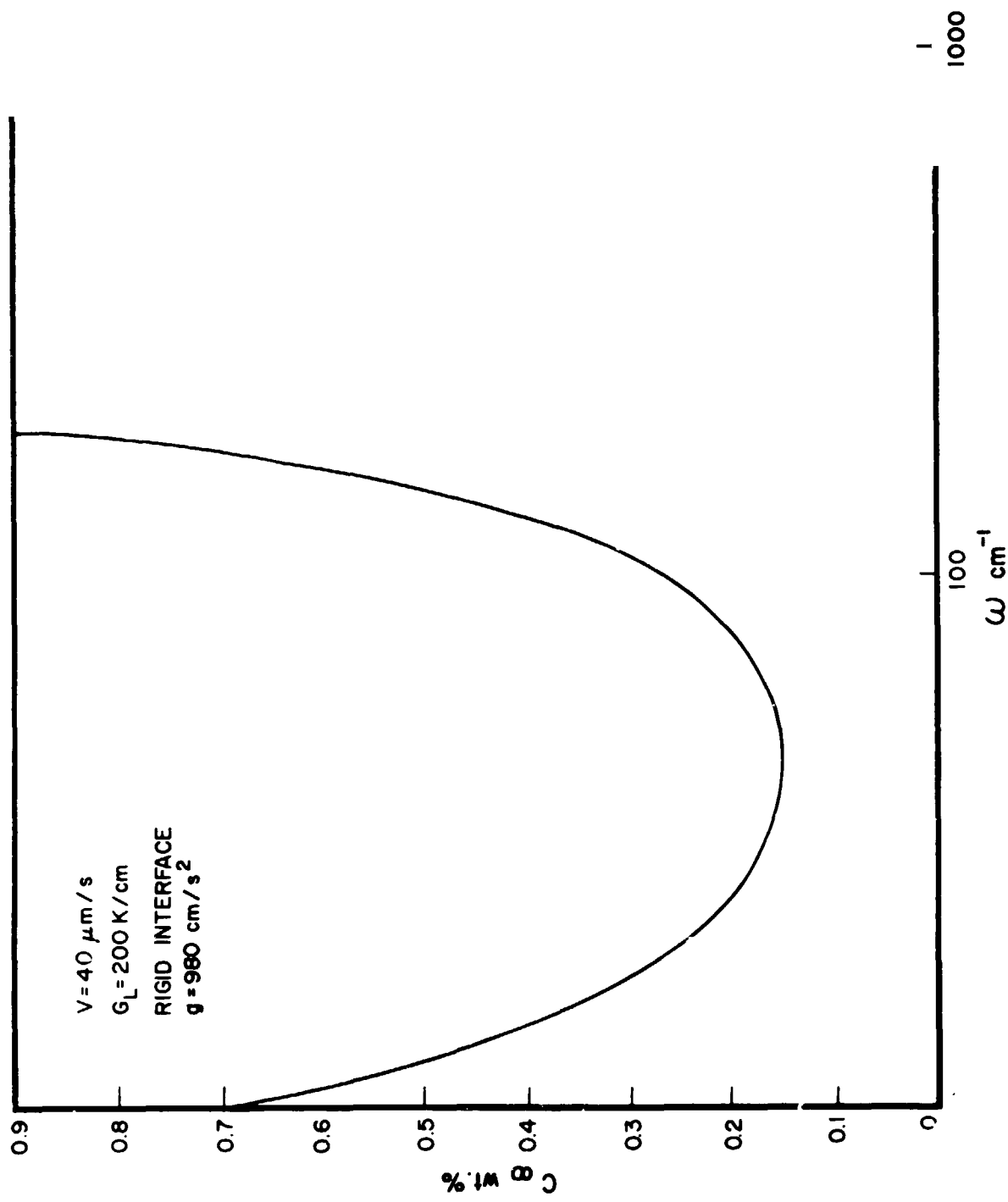
Fig. 8.   The concentration of tin in lead at the onset of instability during directional solidification at $V = 40.0$ µm/s as a function of the spatial frequency of a sinusoidal perturbation. The solid-liquid interface is rigid (planar) so that only convective instability can occur.
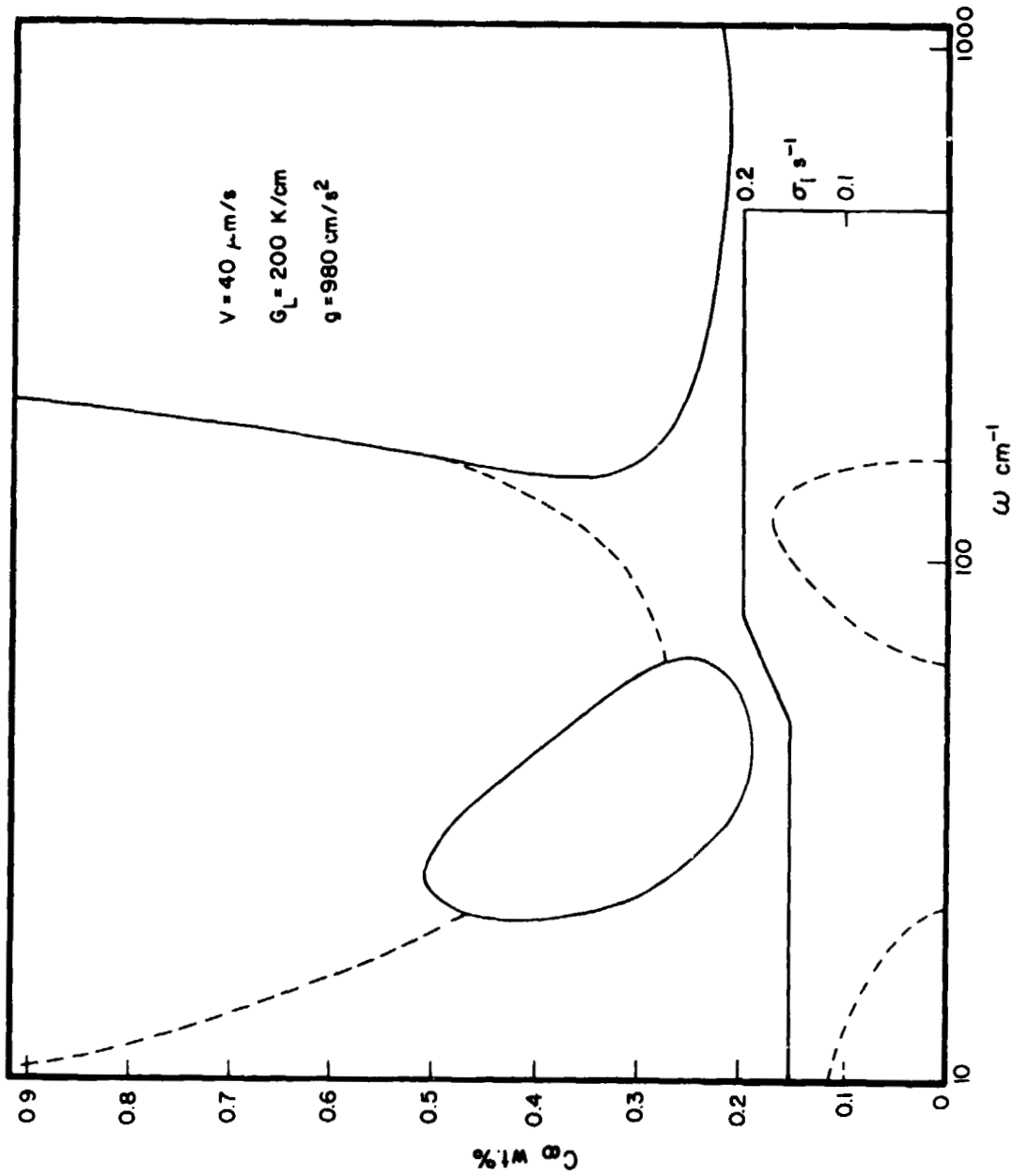
Fig. 9. The concentration of tin in lead at the onset of instability during directional solidification at V = 40.0 μm/s as a function of the spatial frequency ω of a sinusoidal perturbation. Both convective and morphological instabilities can occur; compare with previous two figures. The solid curves mark the onset of non-oscillatory instabilities ($\sigma_i=0$); whereas the dashed curves mark the onset of oscillatory instabilities (the value of σ_i is given on the right hand side).
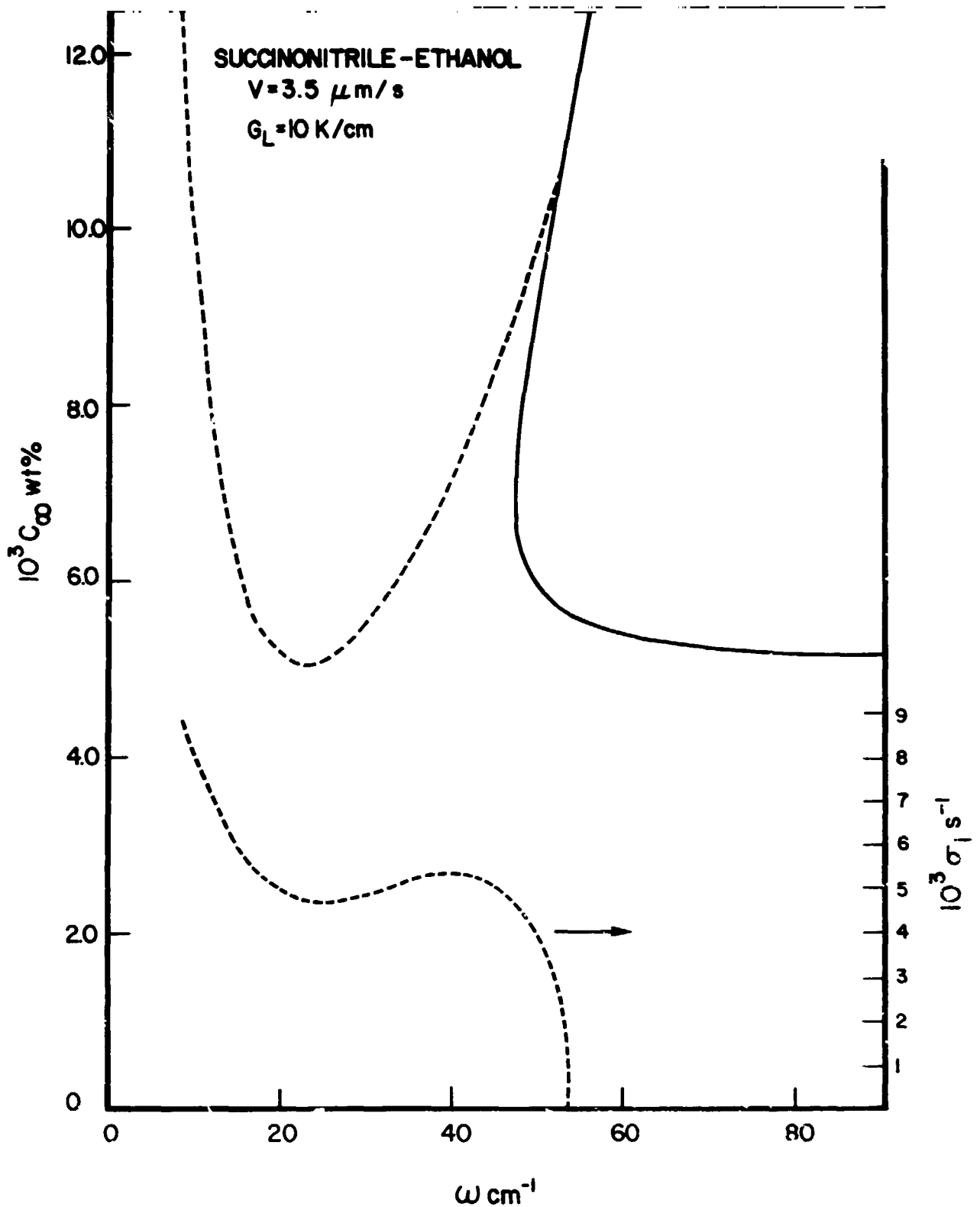
57
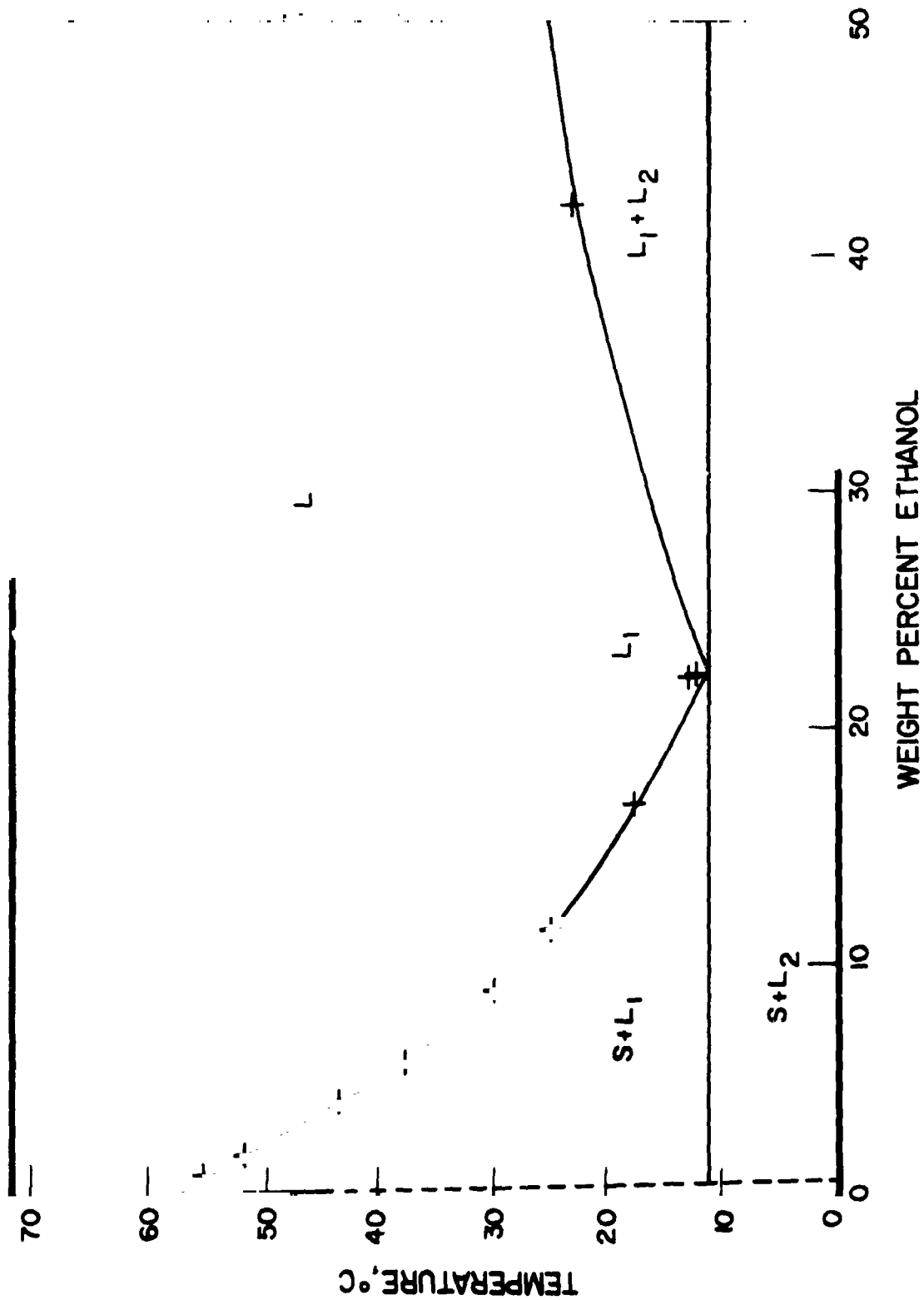
Fig. 10. Partial phase diagram of the succinonitrile–ethanol system, showing liquidus curves data points.

Teflon Valve

Succinonitrile

chamber

Ethanol

Capillary
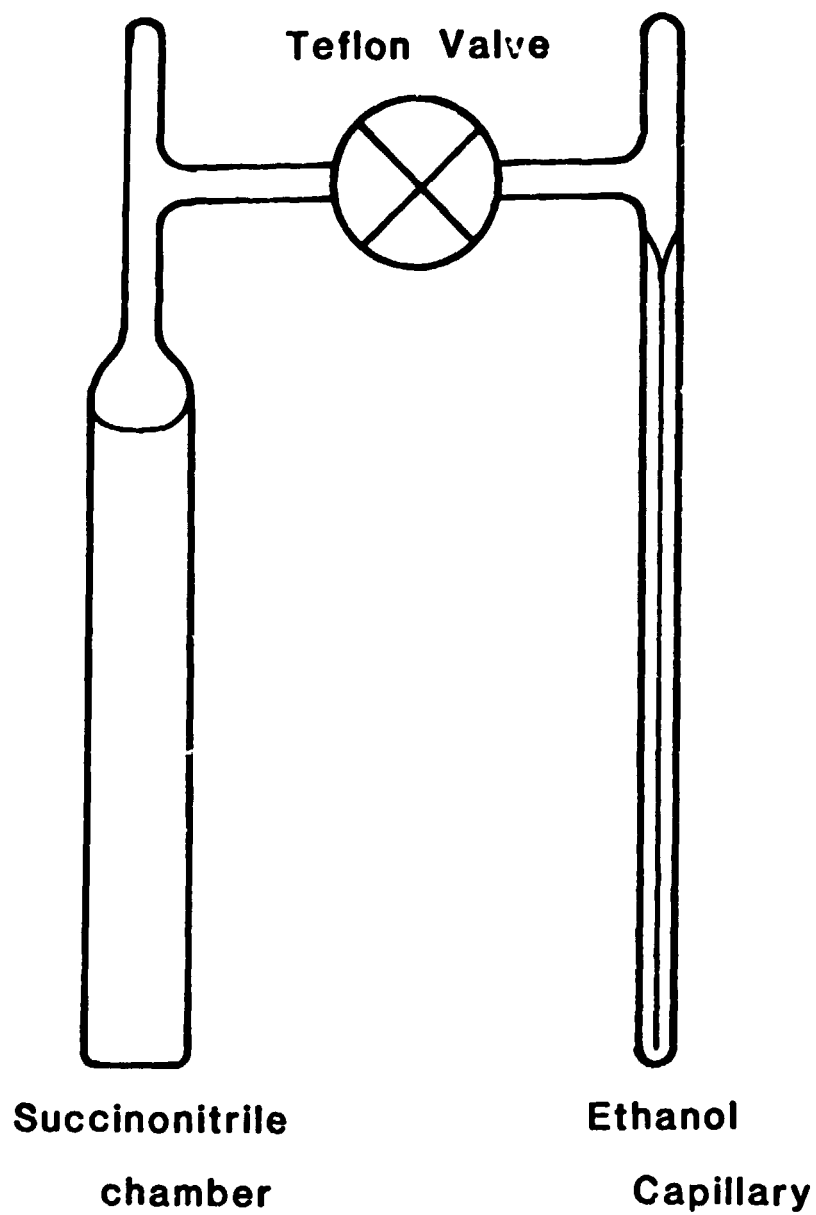
Fig. 11. Apparatus for the preparation of succinonitrile-ethanol mixtures under vacuum.
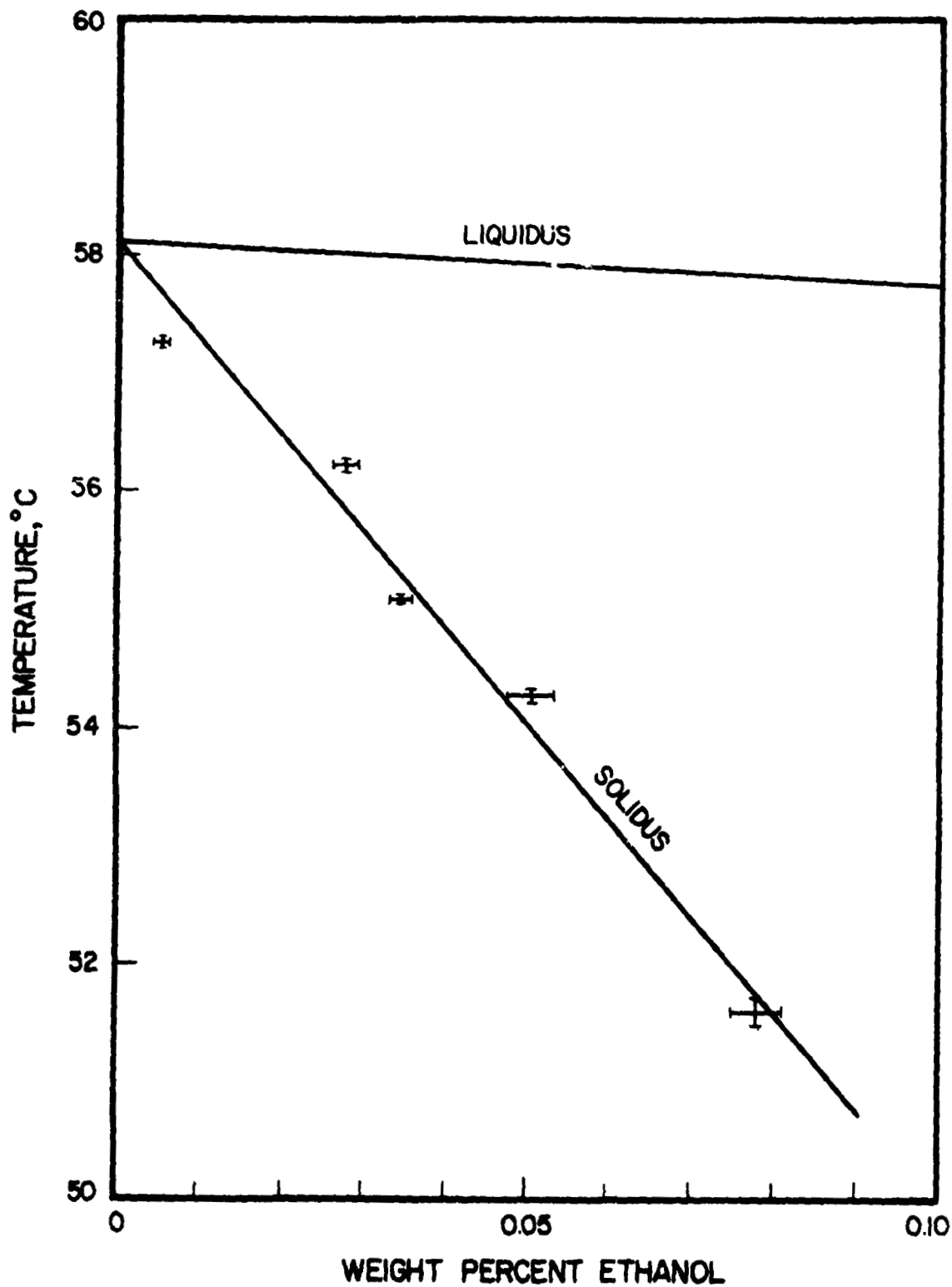
Fig. 12. Detail of succinonitrile-ethanol phase diagram at very small
concentrations of ethanol, showing data points used to determine
the solidus slope.
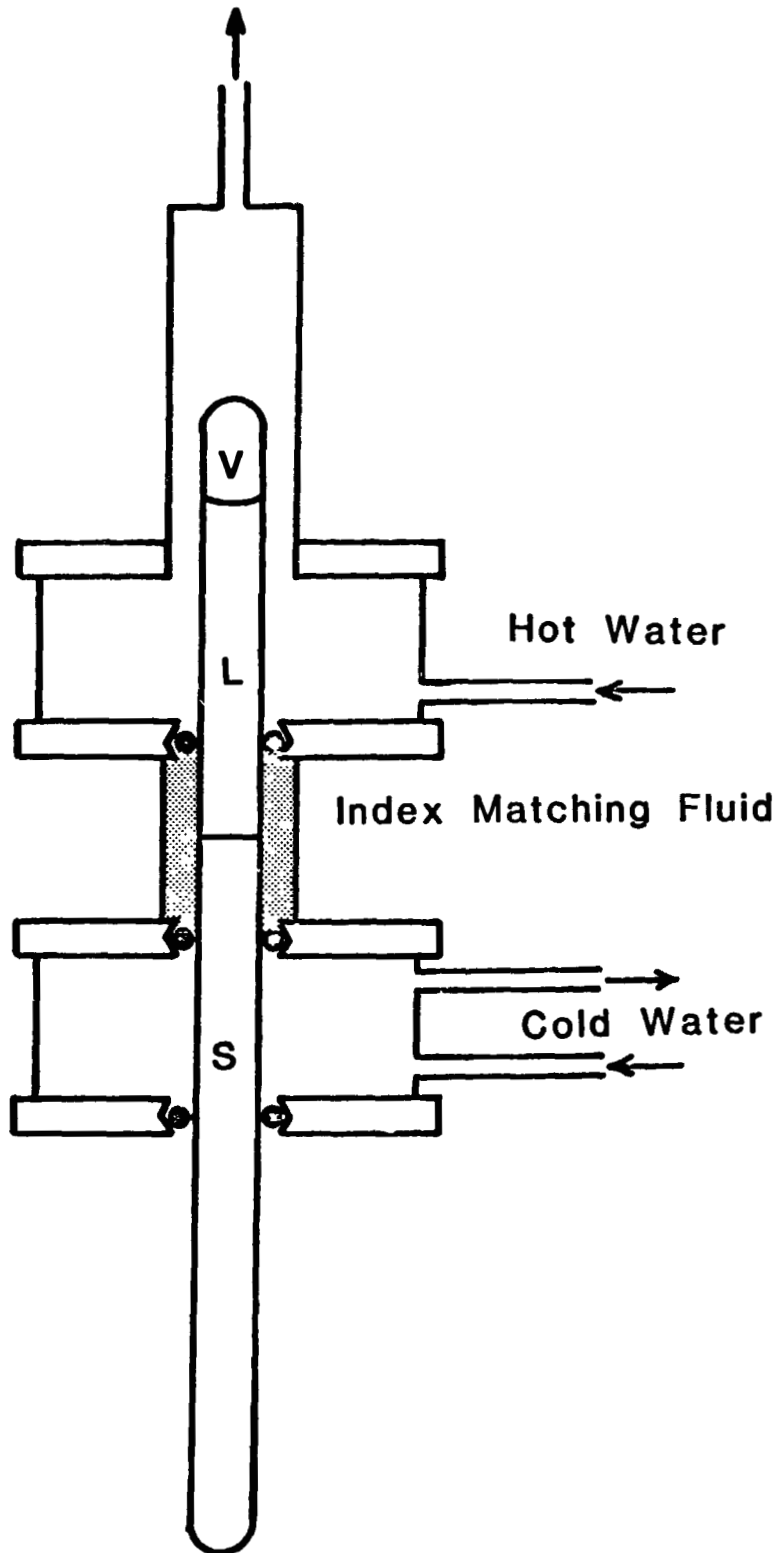
Fig. 13. Unidirectional crystal growth apparatus. The sample is drawn
downwards to produce crystal growth. Thermal insulation surrounding
the water jackets and sample tubes is not shown.

Task 3

Measurement of High Temperature Thermophysical Properties of Tungsten Liquid and Solid

D. W. Bonnell
Chemical Stability and Corrosion Division
Center for Materials Science

SUMMARY

The combined General Electric Advanced Applications Laboratory
(GE), Rice University (RICE), National Bureau of Standards (NBS) effort
has reached the end of its second phase. This phase was intended to
complete the physical connection of the RICE calorimetric system to the
GE levitation facility, and establish the limits of the system for the
acquisition of solid and liquid enthalpy increment data for tungsten in
an actual measurement effort. These limits have been established,
indicating that data are obtainable on solid tungsten up to the melting
point with a precision comparable to prior high temperature levitation
studies. It appears, however, that while liquid data are obtainable,
the reliability of drop successes is so low that it will be necessary to
completely automate the calorimeter system in order to accommodate the
extremely unreliable holding characteristics of the levitation system.
This unreliability is exacerbated by the nature of the calorimetric
measurement requirement.

A number of necessary improvements in the general system have been
made, particularly in the temperature measurement area, which allow
calorimetric quality heat content measurements to be related to an
accurate temperature. These improvements are expected to form a model

which GE will use in a variety of areas, and will hopefully provide the basis for a generally available very high temperature imaging pyrometric device.

Finally, this second phase effort helped establish in detail the precise requirements and degree of control necessary (1) to provide a major improvement in the ability of this experimental effort to yield accurate data and (2) to act as a model for future efforts in high temperature calorimetry, such as space based experiments where only a single operator will be available. Such an operator will, of necessity, need to depend on the instrumentation to control details and provide appropriate feedback, in order to be free to pursue the goals of the experiment, without being lost in the simple achievement of operation of the experiment.

INTRODUCTION

The primary aim of this task has been to evaluate experimental procedures used in the interaction between the General Electric Advanced Applications Laboratory (GE) and the Rice University (RICE) to measure the high temperature enthalpy increments of liquid and solid tungsten. GE has demonstrated a unique apparatus capable of levitating molten tungsten [1] and RICE has wide experience in high temperature enthalpy increment measurements, being particularly successful in the use of drop-type isoperibol calorimeters with levitation heating [2;3a,b;4]. It seemed a natural cooperative effort for RICE to provide the calorimetric apparatus and GE to provide the levitation facility in order to measure the high temperature enthalpy function of tungsten.

The results of this research are of great theoretical and engineering interest. From the scientific viewpoint, the unique location of tungsten at the upper extreme of the metal and element melting point scale should provide a key part in any extrapolation/interpolation procedure. Models, such as the well-known Tamman [5] rule and periodic table correlations [6], are currently used for extrapolation. A definitive value for the heat of fusion of this element will provide a valuable test of such models, perhaps indicating a significant deviation in such predictions based on lower melting refractory metals. Questions concerning the liquid state heat capacity function, i.e., whether it is constant as would be suggested from studies of lower melting refractory metals (see, for example, [7]) and whether current estimates [8;9] of the discontinuity from $Cp(s)$ to $Cp(l)$ are even reasonable, are crucial in testing theoretical models and may provide clues to establishing new parameters in existing

65

or new models. The engineering applications begin with the fact that, without knowledge of the heat of fusion and liquid enthalpy function, melting, forming, and casting equipment must of necessity be overdesigned to allow a satisfactory safety/performance margin. These engineering effects pervade all high temperature uses of tungsten-containing materials.

In the course of this work, it has een necessary to be present during much of the actual experimental work at GE, and both RICE and GE consult this author concerning the resolution of problems at all phases of the experimental process, from initial design to final data reduction. All modifications to the RICE calorimetric system were designed by this author, and a large amount of available research time has had to be devoted to the adaptation of the GE observation system to be an accurate pyrometric device.

Liquid holding capability has proved to be the current unresolved problem. The solution seems to require a totally automated calorimeter which can be set to detect a falling sample, actuate its gates in real time, and acquire the sample, while performing in real time, the preliminary calculations of data reduction necessary to establish the ready state of the calorimeter, the true heat influx, and when the calorimeter again reaches steady state. Such automation, when coupled to an automatic version of the now operational GE pyrometric system, will provide the basis for future experiment, perhaps in space, where real time data acquisition is not a luxury, but a necessity.

EXPERIMENTAL PROCEDURE

The current experimental configuration is shown schematically in Figure 1 (a,b). The sample is supported prior to levitation on a movable pedestal, part of a lava and tantalum platform on rails which can be laterally moved clear of the coil bottom during levitation. This platform can be used to load successive spheroidal samples, but has only marginal ability to select the order of introduction among a group of samples. The tungsten radiation gate below the pedestal assembly must be manually rotated clear of the drop path to obtain a successful drop. A micro-switch on the radiation gate actuator detects the opening of the gate, turns off the electron beam, and turns down the RF power to the levitation coil to drop the sample under control.

The work coil has been recently been redesigned. The original design was a lower-coil-only conical design where the molybdenum "shade" ring acted as a dock for field closure [10;11]. On our recommendation, because of severe instability and the inability to melt, the current coil design depicted in Figure 1a. was implemented by GE. This coil style is a conical modification of the coil type used for liquid platinium containment at RICE [4], incorporating an extra bottom turn to reduce coil leakage. The requirement to pass the physically large ($\sim$ 1 cm) spherical samples and the large pedestal results in a bottom coil throat inside diameter of $\sim$ 1.3 cm. This large bott. opening still exaggerates the possibility of sample loss due to dripping, as was the case for the original coil, and it is certain that more work needs to be done by GE in this area. The incorporation of an upper coil turn does, however, allow higher coil power to be used to improve stability and lessen the

67

probability of coil dripping. The shade ring over the coil has been retained to continue to serve as electron beam s$_{r}$ill protection for the work coil.

The levitation coil is driven by a 25 kW, 450 kHz General Electric induction furnace. The vacuum feedthrough to the coil is a GE coaxial design; the entire transmission line including inductive coupling (matching transformer) allows power factors > 0.8.

The levitation coil is not designed to provide sufficient heating to melt the sample. The maximum temperature reached by induction power alone is approximately 2800 K. A simple calculation for the 1 cm diameter samples of this work using the Stefan-Boltzmau Law, i.e.,

$$dH/dt = E_T A \sigma \Delta(T^4)$$

(where dH/dt is the rate of radiant energy loss for a body of area A, total hemispheric emissivity E_T at a differential temperature $\Delta(T)$ to its surroundings. σ is the Stefan-Boltzmann constant of proportionality, 5.67032 x 10^{-12} W·cm^{-2}·K^{-4} [12]) gives the 2800 K radiation loss as about 310 watts when a value for E_T of 0.28 [13] is chosen for tungsten.

At the melting point of tungsten, 3695 K [14], the loss is expected to be about 1000 watts. This additional power is provided by electron beam (e-beam) heating. In the levitation environment, e-beam heating is possible only at temperatures where secondary electron emission is high enough to maintain approximate charge neutrality. Tungsten's secondary emission characteristic meets this criterion even for electron power fluxes much in excess of 1 kW [15]. The electron beam gun shown in Figure la directs a 35 kV, 150 mA focused electron beam onto the top of a levitated specimen. This power is clearly sufficient to achieve

melting even with considerable loss due to charging. A significant problem in this form of heating is the localized influx of energy due to spot focusing. While the sample is solid, the top to bottom temperature gradient is of the order of 50 K, with some uncertainty due to the fact that the single point of view of the pyrometer provides only an oblique view of the top and bottom.

Sample outgassing can release large bursts of gas. In the work coil region, a pressure burst can raise the pressure to a level where an RF discharge can be supported. When this happens, safety interlocks must necessarily shut down power to protect the apparatus. Approximately two thirds of all fresh samples are lost prior to or near the melting point from this cause. In addition, a major portion of the lower temperature deposition on the internal optics appears to occur from fresh samples. It is clearly necessary to preprocess all samples before use to alleviate these problems.

The calorimeter proper is a chrome-over-gold plated copper cylinder 20.3 cm high and 13 cm in diameter. The center tapered receiving well is a removable copper sleeve 5-1/4 cm top inside dimension and 11 cm overall in length. A similar sleeve, wound with a manganin wire heating element, was used for electrical calibration. The calorimeter receiving well is lined with 0.010 inch tungsten foil and a variety of shards of tungsten stand in the well to prevent splash back. The splash protection has not been tested due to lack of liquid drops, but slightly surface melted samples have impacted the well with no damage and good heat transfer. This technique of splash protection has worked well for a variety of other systems [2;4].

The total 25 °C heat capacity of the calorimeter as calibrated was 7893 ± 7 J/°C. The basic uncertainty in total heat using this system, exclusive of sample loss errors, radiant or electron beam power influx, but inclusive of reasonable jacket temperature excursions, thermometer errors, receiving well and foil liner weight errors, etc., is expected to be much less than 0.5 percent.

A primary problem in this research effort has been the high temperature measurement capability. Under 35 kV electron bombardment, tungsten emits copious x-radiation. For this reason, visual access is highly restricted and a special imaging pyrometry system is needed. A General Electric silicon charge injection diode array camera is used to provide a 30 frame/sec oscilloscope image of the sample and work coil area at an image magnification of about 5x. The levitated sample typically covers about half of the 10,000 diodes of the 100 x 100 camera area. A GE constructed address/sample-and-hold unit allows selection of any one of the diode elements for analogue intensity output. The diodes have a dynamic range of about 20 (max. signal/avg. noise) and a linearity a. long term stab. ity of better than one part in 10,000. The spectral response, however, (characteristically shown in figure 2) is quite non-linear. A major portion of this task effort has been devoted to implementing techniques necessary for conversion of this device into a pyrometrically reliable tool. The initial effort by GE was to simply extrapolate the optical response of a selected diode by an exponential function from ribbon filament temperatures to the region of temperature interest. Given the fixed reference point of the melting point of tungsten, this technique should be good to 2 or 3 percent near the

reference point. As will become apparent in the following discussion, this extrapolation is potentially poor, especially if the fixed reference point is not well identified. The probable error without considerable precaution could be of the order of 5 percent, i.e., perhaps as much as 200 K. A reasonable goal in enthalpy determinations is one to two percent overall. This requires significantly better than one percent pyrometric accuracy to achieve this error level in the face of emissivity uncertainties, sample temperature inhomogenieties, and the general problem of optics coating occuring due to sample outgassing and tungsten deposition.

The optical path arrangement for pyrometry currently in use is shown in Figure 1b. The consequences of restricted access, the camera characteristics, vapor deposition problems, and the lack of black body conditions to the implementation of accurate pyrometry require consideration of the theory and practice of optical pyrometry.

Plank's law provides the basis for pyrometric measurements, relating spectral radiant flux to temperature by

$$J_\lambda = \frac{c_1 \lambda^{-5}/\pi}{\exp(c_2/\lambda T)}$$

where c_1 and c_2 are the first and second radiation constants (c_1 = 3.741832 x 10^{-16} W·m; c_2 = 1.438786 x 10^{-2} m·K), λ is the spectral wavelength, and T is the absolute temperature. J_λ is then the radiant flux per unit area, per unit solid angle, per unit wavelength. The basis for the current International Practical Temperature Scale (IPTS-68) [16] at temperatures above the gold point, 1336.15 K is the

ratio of the flux at temperature, T, to that from a body at some reference temperature, T(ref). Figure 3, using the right scale, shows the temperature behavior of this ratio for a fixed reference temperature of 1600 K and an ideal filter with unit transmission in a pass band 1 nm wide centered at the wavelengths given. This technique is usually referred to as brightness pyrometry.

Traditional pyrometry operates at a center wavelength of 650 nm with a typical band pass (including the observer's sensitivity) of about 350 to 400 nm. Photoelectric pyrometers typically use band pass filters with a transmission window ∿ 35 nm wide. It is clear from Figure 3, that in the realm of 2500 to 4000 K temperature measurements, significently more sensitivity in temperature measurement is possible if shorter wavelengths are used. In this temperature region, there is still, however, more than a factor of two difference in absolute flux, favoring the longer wavelengths. At 3700 K, a 25 K change in temperature produces an absolute flux change of 6 percent at 450 nm, 5 percent at 550 nm and ∿ 4 percent at 650 nm.

At lower temperatures, another form of pyrometry has been used. Called two-color or ratio pyrometry, it uses the ratio of the fluxes at two wavelengths as the measured function of temperature. For any given wavelength pair, the sensitivity falls rapidly with increasing temperature (see Figure 3, left scale and ratio curves). The high sensitivity curves use wavelengths where the flux at the shorter wavelength is very low at low temperature. However, a multicolor measurement using appropriate band passes can provide redundant temperature measurement.

Further, to the extent that emissivity on optics absorption is just independent of wavelength the measured temperature is independent of emissivity and changes in absorbance. With multicolor redundancy, it is possible to measure emittance directly.

The general spectral response function of a silicon diode, shown in Figure 2, indicates a rapid fall off in sensitivity at shorter wavelengths, and the catastrophic termination of response at larger wavelengths, where silicon becomes transparent. A choice of wavelengths is available in this region and it is not at all clear that the traditional value of 650 nm is necessarily the best choice.

The primary problems plaguing the spectral flux or brightness pyrometry method are the uncertainty in emissivity and absorption effects. The technique obviously requires complete knowledge about the actual transmission of all optical train elements, but is relatively less sensitive to the spectral behavior of the absorbances in the path as long as they do not change and the pyrometer's spectral response band pass is sufficiently restricted.

In order to implement the brightness pyrometry technique, it was necessary to provide a reference source. Traditional pyrometers superimpose an image of an internal standard lamp on the attenuated image to be measured. The standard lamp flux is then adjusted to match the attenuated source image and the ratio is accomplished as a null measurement. The range of comparison between internal standard lamp and external source generally uses a broad band absorber as the attenuator. The external comparison of a black-body source and a hotter body is accomplished by attenuating the light from the hotter body by a device called

a sector wheel; essentially this is a chopping wheel behaving as a mechanical aperture utilizing the eye as a visual smoothing device. This method can provide for a direct reading instrument of excellent accuracy and stability, but has no capability for dealing with changing absorbance in the optical path, such as occurs when vacuum deposition occurs. Vacuum deposition on the vacuum pyrometer window and reflection mirror changes the transmission of the optical train typically by a factor of two to five in the course of a single experiment. This magnitude of change is equivalent to a temperature change of 300 to 500 K.

The installation of a reference lamp internally within the vacuum system was thus required. The mirror, M1, shown in Figure 1b, reflects an image of the sample through the vacuum window which is located so that no direct line of sight exists between the sample and that window. This essentially eliminates coating of the window and provides x-radiation protection. The small mirror M2 superimposes an image of the internal reference filament at the image plane of the sample, offset to one side about 1/2 cm visually from the sample limb. M2 shades this filament from deposition and its orientation shields its own surface. Mirrors M1 and M2 are 1/4 wave flat first surface mirrors, $\sim$ 7 cm^2 as used, obtained from Edmund Scientific Corp. The installation of a General Electric 18A/6V/T10 strip lamp provides the means to establish an initial temperature scale, by comparison with a Pyro micro optical pyrometer, and the means to make a running measurement of deposition on mirror M1.

The procedure which has been developed involves replacing the levitation coil assembly with a thick glass plate and pumping the system down when a new lamp must be installed. The lamp is then operated over

the region from ∿ 1600 to 2450 K, brightness temperature (∿ 1750 to 2770 K true temperature), while measuring the current drawn by the lamp as a function of brightness temperature monitored by the pyro optical pyrometer observing through the glass plate. The current is measured with a 4½ digit voltmeter monitoring the voltage drop across a high current shunt. Current is supplied to the lamp from a well regulated dc supply. At the same time, the GE camera also monitors the strip lamp through its optical train. The emissivity of tungsten selected [17] was 0.425 for this filament. The procedure must be repeated frequently, as the lamp reference is operated far above its long term stability point [18]. This technique provides a low temperature reference to the IPTS-68 once the absorbance of the thick optical plate is corrected. This is accomplished in a separate experime   by measuring the temperature change, as a function of lamp brightness temperature, with and without the glass plate in the optical path. The sighting path through the plate was identified by physically marking the plate and carefully measuring and preserving the angles of the calibration experiment. The preferred method of performing this correction is to actually measure the absorbance [4] but in most cases, an actual temperature effect measurement is adequate. The Wien approximation to the Planck Law

$$J_\lambda = \frac{c_1 \lambda^{-5}/\pi}{\exp(c_2/\lambda T)}$$

is a good approximation in this temperature wavelength regime. Since transmittance is just

$$\frac{I}{I_0} = e^{-ax} = \text{transmittance}$$

75

and in the Wein approximation, behaves just as an emittance, identifying

the flux change as a transmittance effect gives the relation between

brightness temperature T_B^* observed without the absorber to the observed

temperature $T_{apparent}^*$ with the absorber as

$$\frac{1}{T_B^*} - \frac{1}{T_{apparent}^*} = \frac{\lambda \ln(e^{-ax})}{c_2} = K_{absorber}$$

The glass plate used showed a variation in K of a factor of two over the

temperature range 2300 to 2500 K. This is attributed to a color depen-

dence in the glass transmission, and the $K_{absorber}$ values were applied

at the T_B^* values measured. The effect of this absorber was to lower

observed brightness temperature by 95 to 52 K. The error due to uncer-

tainties in the exact wavelength dependence were estimated from the

direct lamp temperature versus current measurements to be of the order

of 15 K. This plate must be replaced in future measurements by a sheet

of pyrex or quartz whose visible spectral characteristics are known and

well behaved.

The imaging array camera uses a relay lens with an effective aperture

of 1 in. to provide the necessary magnification to nearly fill the frame

with the sample image. To convert this device to a pyrometric device,

it was necessary to control in a known way, both the relative sensitivity

and the true spectral wavelength response of the system. As a result of

early trials, a combination filter holder, aperture control device was

designed and put into service. This device fits on the entrance aperture

of the relay lens and has two manually turned detented wheels. One

wheel holds one inch aperture narrow band ($\sim$ 80 mn FWHM) interference

filters blocked to 10^{-4} or better outside the band pass. The two filters actually calibrated in this work had band passes centered at 651 nm and 451 nm. An auxillary broad band pass neutral density (ND) filter mounted on front of the filter/aperture device was used as a range control. The other wheel has a series of knife edged circular orifices: 1, 5/8, 1/2, 5/16, 3/16, and 1/8 inch in diameter, which were to be prepared to ± 0.0005 tolerance.

Calibration consisted of comparing the output of a specific diode of the imaging array as a function of temperature, filter aperture and ND filter with clean freshly mounted mirrors using the internal cali-brated lamp. A variety of measurements for cross checking redundance were taken to allow the calculation of any observation from others. The one inch aperture was found to be larger than the system aperture, as expected. The 5/16 aperture consistently showed itself to be 7 percent too small in area or 0.010 inch smaller than the manufactured 5/16 (0.312 inch) aperture. On subsequent check, the actual diameter was found to be 0.302 ± 0.001 inch, exactly as predicted. All other apertures, and the transmission factors of the two filters agreed with actual temperature measurements with a reproducibility of better than 0.6 percent. The quality of the fit of data over the lower temperature calibration range fit the Planck Law expression with a maximum error of 15 K and an average error of 5 K. When translated by aperture changes to the tempera-ture range 3500 to 4100 K, cumulative errors in aperture and fixed optical path absorbances are expected to contribute less than an additional 10 K error. With the built-in reference, the remaining problem is changes in the spectral reflectivity of mirror M1. In fact, the very

effort to measure the problem, taking pyrometric measurements at two or
more wavelengths, allows an independent check on temperature when the
wavelength dependence on reflectivity of M1 is measured. Where possible,
experiments are arranged to attempt this, but the inability of the GE
system to provide a significant time of constant temperature liquid
levitation (or even hold on to the completely liquid sample) has restricted
these measurements to stably levitated solids. In that case, the agreement
between the three temperatures, brightness at 650, brightness at 450,
and color ratio between these two measurements has a precision of better
than ± 20 K, indicating accuracy attained of ~ 0.6 percent.

DISCUSSION AND CONCLUSIONS:

The main goal of this phase of this task has been to help RICE install
a calorimetric subsystem on GE's existing and proven [19] liquid tungsten
levitation system. The necessity of converting an approximate temperature
tool into a precision pyrometer was anticipated, and although a variety
of problems were encountered (such as the need to operate around extreme
radio frequency interference (RFI) from adjacent unrelated experiments,
internal problems with the diode select logic, etc.), the procedures
which have been established are workable and meet the initially antici-
pated needs of the project. The calorimetric system has performed
perfectly. The addition of a data logging system at the beginning of
this phase was made to eliminate the need for an observer for the calorim-
eter heat trend. As expected this addition allowed the expansion of
effort from two to as many as six drop attempts per day. The 8 kJ heat
capacity of the calorimeter block and the vacuum insulation still restricts
the effort to one sample in the calorimeter in four hours.

It had been anticipated that if this phase progressed as in fact it did, that we would have obtained several successful liquid drops and be in a position to refine the current value uncertainty in the heat of fusion, H_m(tungsten).

The Tamman Rule [5] ($\Delta H_m/T_m = S_m \sim 2.3$ cal/mol·K) value of 8.5 kcal/mol has been the operational value in all the standard references [9;20]. Dikhter and Lebedev [21] have obtained a value of ΔH_m by an exploding wire technique. Their direct value, 80 ± 4 cal/g, corresponds to a value of 14.7 ± 0.7 kcal/mol. This value is remarkable as is implies a value of $\Delta S_m \cong 4$. The largest value of ΔS_m known for the transition metals is molybdenum, with $\Delta S_m = 3.08$ cal/mol·K [3a]. Even though the general trend in ΔS_m seems to be increasing down each group [4] and tungsten is below molybdenum, this value still appears to be too high. Kubachewski, et al. [22] give a value of 12.1 kcal/mol for ΔH_m(silicon) which was expected [23] to have the highest heat of fusion of any element. Wouch, et al. [19] report a value for ΔH_m of 11 ± 1 kcal/mol obtained by applying a cooling curve model to experimental data. The model ignores supercooling, but provides a value of ΔS_m of 2.98 ± 0.3 cal/mole·K, in line with expectations from the molybdenum data. The value is still very uncertain, as Wouch, et al. [19] repeatedly noted, especially in the weakness of this derivation for non-spherical samples. (Terrestrial levitation). In the course of this work, to establish the GE ability to levitate and melt, a sample was allowed to fall onto a copper plate in a one meter drop tube. The sample splashed as though completely molten, and all (± ∼ 1 percent) fragments were recovered. Since the temperature was estimated to be just above melting, even if ΔH_m is 8.5 kcal/mole,

significant supercooling must have occurred and the Wouch, et al. [19] model for the cooling curve type of determination [24] should not apply.

Unfortunately, even though the calorimetry and pyrometry are now functional, the levitation process itself has been plagued with problems. Although outside the area of this task, improvement in this area is essential to the task and efforts to deal with the problems have been made. The work coil was changed at our suggestion. The problem of the so-called "hot short", where samples would deform, "melt", or explode at temperatures hundreds of degrees below the melting point of tungsten was again encountered. Previously, this problem had been diagnosed as being caused by hydrocarbon contamination during machining of the specimens. This recurrence was identified as vapor deposition of volatile metals from the soft solders used in the coil area. Figure 4 shows the effect of this problem on a group of samples. In addition to the loss of samples, the shape change can be mistakenly interpreted as melting, making the use of visual observation of "melting" as an internal pyrometric calibration point unreliable.

The most serious problem has been the inability of the levitation system to melt and hold tungsten. More than 30 samples have been levitated and successfully e-beam heated in full dress calorimetric runs In no run has it been possible to contain the liquid for more than 1 to 2 seconds before inadvertant pouring from the coil occured. With the current level of hand operations necessary, the very short, unpredictable containment times give an intolerable failure rate. The consequences of the levitation containment problem are quite important the eventual

success of this program. The current implication under consideration is that the surface tension/density ratio of liquid tungsten is perhaps as low as that for gold or lower. This problem was encountered at RiCE in an effort to measure enthalpy increments for tantalum [4]. The measurement effort for platinum also required special efforts to contain. It is quite possible that this will be a general property of the entire third long period of the transition elements. Improving containment could require a significant additional effort on the part of GE to improve their levitation facility

Because of the containment pr   , it has been necessary to suspend experimentation in this effort. At a minimum, it will be necessary to automate the calorimetric system to improve the system response time to the point where the ability of the calorimeter gate structure to respond no longer requires long or predictable containment times. The general characteristics of such a system have already been examined and will be the subject of future reports when the various aspects have been discussed fully with RICE and GE. RICE is expecting a new post-doctoral student to enter this project and the final form of the plans will, of course, depend on this.

The advantages of an automated calorimeter system extend beyond the immediate application. It is expected that calorimetric studies will be among those selected for microgravity experiments. The current effort requires three or four researchers to operate the apparatus and take data. The reduction of data   heat content and temperature requires some time as well. The effort of automating the calorimetric system and integrating the pyrometry system into such automation obviously is a

step which will be done in the normal progress of this experimentation. This seems to be the obvious time to implement such automation. It is recommended in the interest of future efforts, that the pyrometric system be automated as well. The major item necessary to providing an automated pyrometric system is some method of measuring the change in absorbance of the primary mirror, M1 (Figure 1b).

Figure 5 shows a schematic of the hardware portion of a proposed automatic imaging pyrometric system. The motor driven aperture and filter assembly on the pyrometer is a simple extension for computer control. The novel feature is the modulated photodiode assembly. With a chopping wheel modulating the internal filament, a simple photodiode can be used to extract the change in apparent brightness of the reference filament by lock-in amplifier techniques. With this information in real-time as well as the output from the imaging array, a microcomputer can, with careful calibration as has already been developed and described in this report, provide an almost real-time display of true temperature, and report the onset of problems in temperature measurement from the multiple redundancy inherent in multicolor pyrometry.

The same computer can easily have the capability to handle the calorimeter automation and data logging requirement. The same data system, with auxiliary floppy disk storage, can provide complete data reduction in a few minutes after the experiment ends. In fact, a running monitor of the final period of the experiment may be able to significantly shorten the 4 hour per run time period currently necessary for best work.

REFERENCES

1. G. Wouch, "Containerless Melting and Solidification of Metals and Alloys in the Terrestrial and Space Environment", Ph.D Thesis, Drexel Univ. (1978).

2. A. K. Chaudhuri, D. W. Bonnell, A. L. Ford, and J. L. Margrave, High Temp. Sci., 2, 203 (1970).

3. J. A. Treverton and J.L. Margrave,
   (a) J. Phys. Chem. 75, 3737 (1971).
   (b) J. Chem. Thermodynam. 3, 473 (1971).

4. D. W. Bonnell, "Property Measurements at High Temperatures--Levitation Calorimetry Studies of Liquid Metals", Ph.D Thesis, Rice Univ. (1972).

5. G. Tammann, Z. Phys. Chem. 85, 273 (1913).

6. J. L. Margrave, High Temp.-High Press. 2, 583 (1971).

7. D. W. Bonnell, A. J. Valerga, and J. L. Margrave, "Radiation and Conduction Loss Corrections to Free Drop Calorimetry," in preparation (1981).

8. JANAF Thermochemical Tables, (Joint Army, Navy, Air Force) Second Edition, D. R. Stull et al. (Eds.), NSRDS-NBS 37, U. S. Government Printing Office (1971).

9. R. Hultgren, P. D. Desai, D. T. Hawkins, M. Gleiser, K. K. Kelley, and D. D. Wagman, Selected Values of the Thermodynamics Properties of the Elements, Amer. Soc. for Metals, Metals Park, OH (1973).

10. R. J. Begley, G. Comenetz, P. A. Flinn, and J. W. Salatka, Rev. Sci. Instr. 301, 38 (1959).

11. J. C. Lewis, H. R. J. Neumeyer, and R. G. Ward, Rev. Sci. Instr. 39, 569 (1962).

12 E. R. Conen and B. N. Taylor, J. Phys. Chem. Ref. Data 2, 663 (1973).

13. C. C. Jun, S. Ebrahim, and M. Hoch, High Temp.-High Press. 2, 43 (1970).

14. A. Cezairliyan, High Temp. Sci. 4, 248 (1972).

15. R. T. Frost, Private Communication (1975).

16. The International Practical Temperature Scale, Metrologica 5, 35 (1969).

17. R. D. Larrabee, J. Opt. Soc. Am. __49__, 619 (1959).

18. H. J. Kostkowski and R. D. Lee, Theory and Methods of Optical Pyrometry, NBS Monograph 41, U.S. Government Printing Office, Washington, DC (1962).

19. G. Wouch, E. L. Gray, R. T. Frost, and A. E. Lord, Jr., High Temp. Sci. __10__, 241 (1978).

20. K. K. Kelley, U. S. Bureau of Mines Bull. No. 584 (1960).

21. I. Ya. Dikhter and S. V. Lebedev, High Temp.-High Press. __2__, 55, (1970).

22. O. Kubachewski, E. L. Evans, and C. B. Alcock, Metallurgical Thermochemistry, Fourth Edition, Pergamon Press, London (1967).

23. J. L. Margrave, Private Communication (1972).

24. J. L. Margrave, D. W. Bonnell, and J. Weingarten, "Thermodynamic Property Determination in Low Gravity", Final Report, NASA Contract NAS8-32030 (1977).

---

* The trade names listed in the descriptions of equipment in this report are provided for identification purposes only.

84

FRONT VIEW
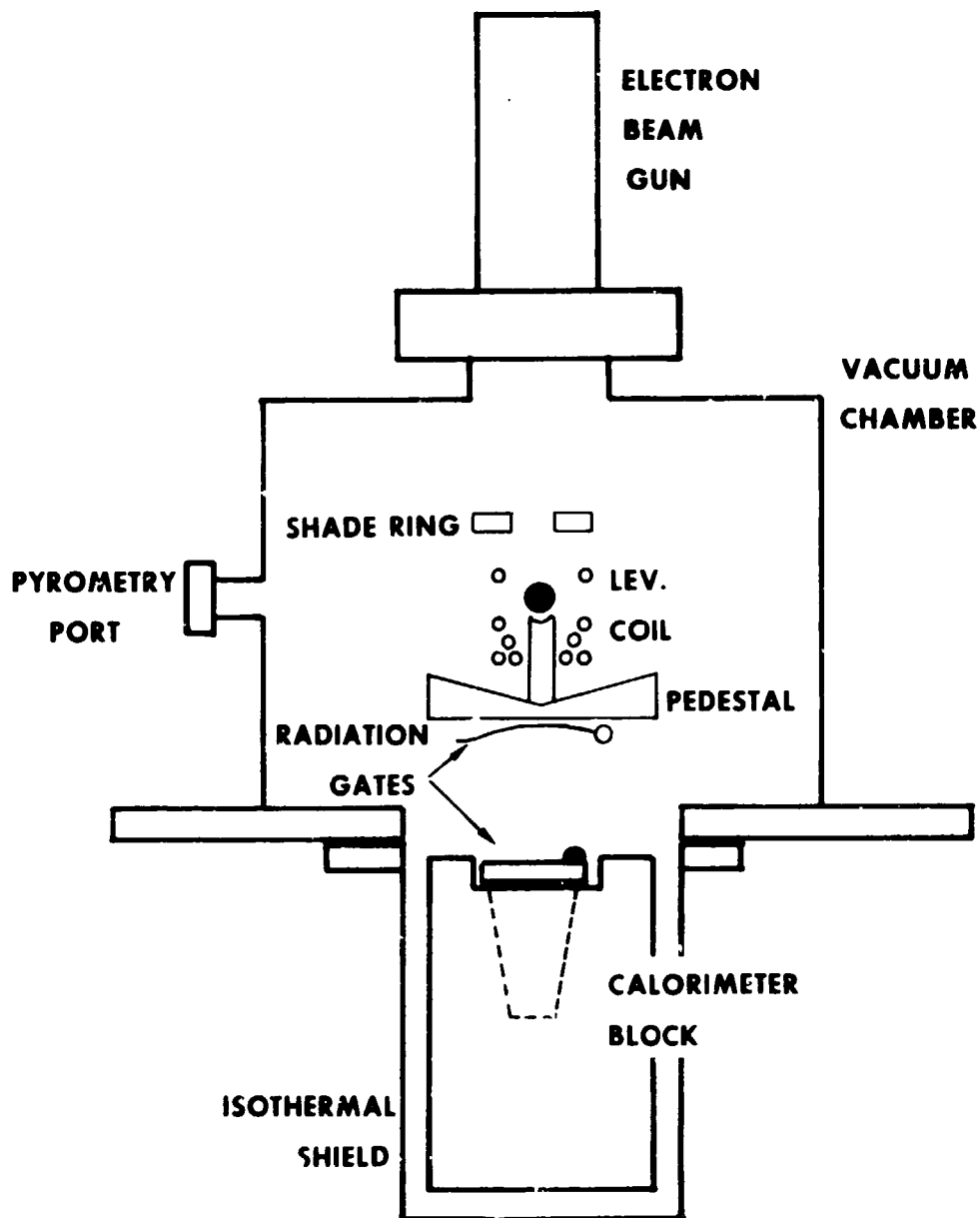
FIGURE 1a

Fig. 1a. Front cross sectional view of the CE-Rice coupled apparatus
showing the relative orientation of major components.

TOP VIEW

REF.
FILAMENT

M1

M2

LEV
COIL

WINDOW

BEAM
SPLITTER

FILTER
HOLDER

IMAGING
ARRAY
CAMERA

RELAY
LENS

DIODE SELECT LOGIC

SAMPLE & HOLD

CHART
RECORDER

DVM

'SCOPE
MONITOR
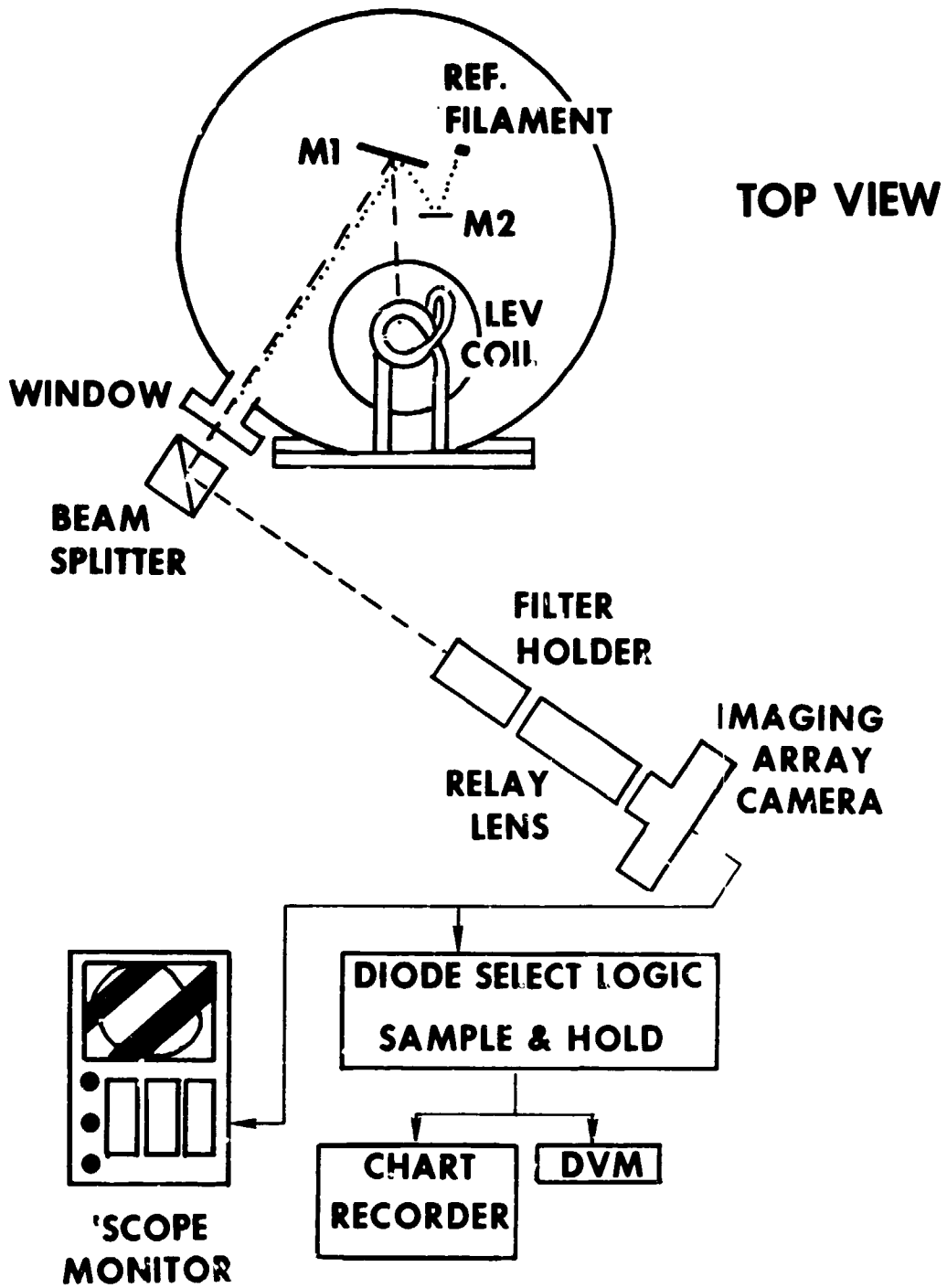
FIGURE 1b

Fig. 1b. A top view showing details of the optical arrangement for pyrometry.

TYPICAL
SPECTRAL RESPONSE
for SILICON DIODES
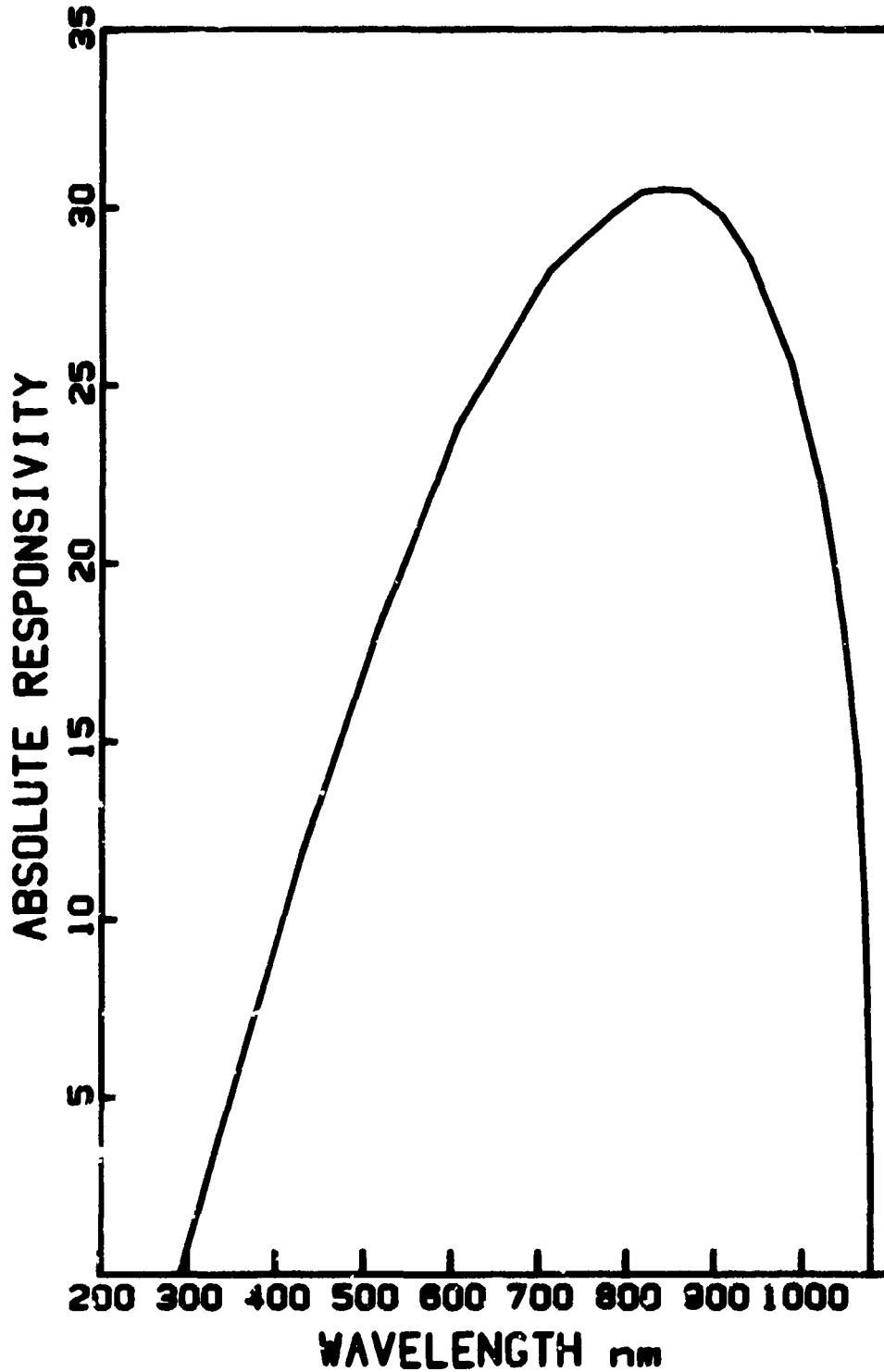
Fig. 2. Characteristic spectral response behavior for silicon photodiode type devices. The GE imaging array elements have a similar response function.
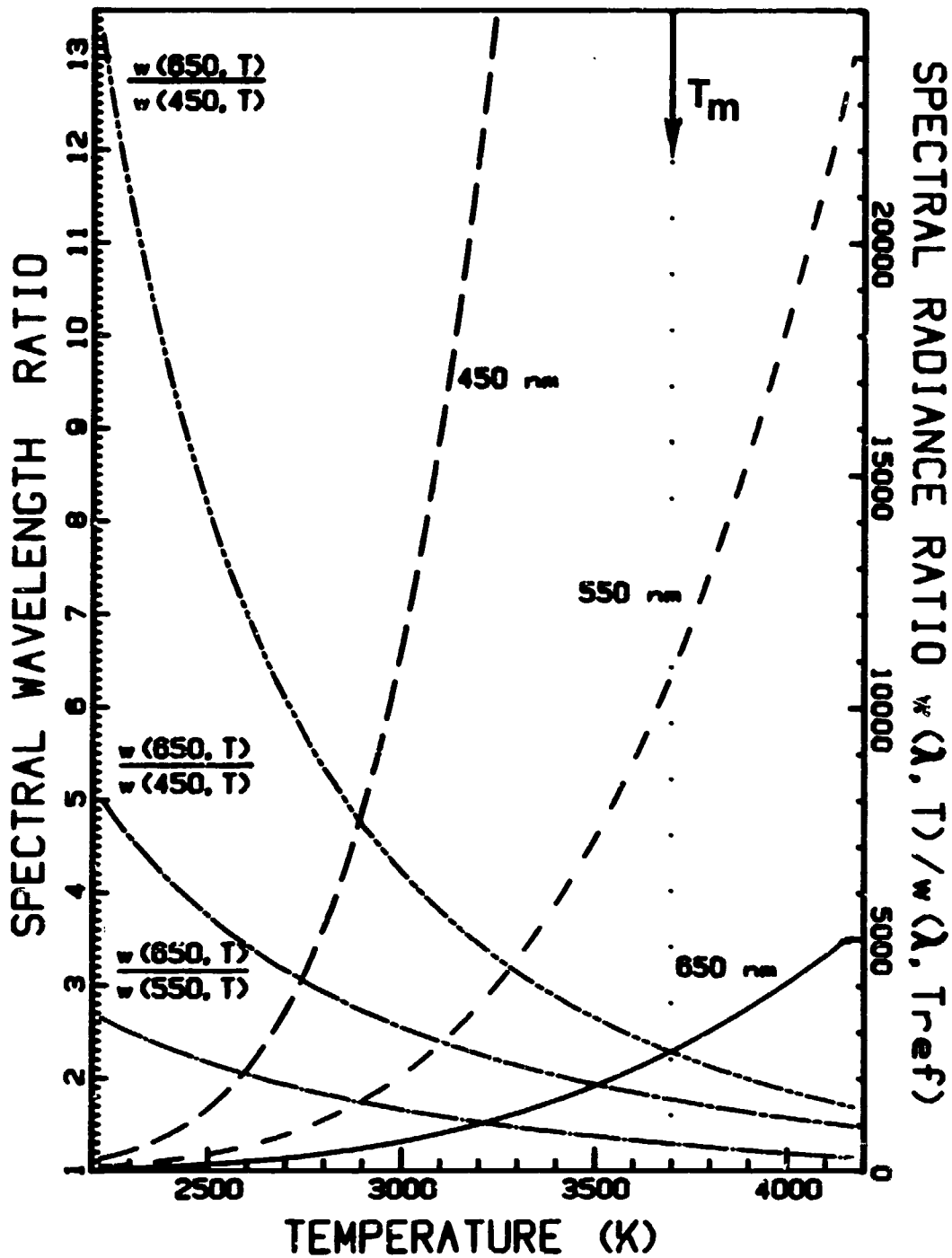
Fig. 3. Plank law functional behavior for two type of pyrometry. The dashed (and solid) curves are spectral radiance ratios (right scale) for the labeled wavelengths for T_{ref} = 1600 K, typical of brightness pyrometry. The dot-dash curves show the flux ratios (left scale) for wavelength pairs, typical for multicolor pyrometry.

"HOT SHORT" SAMPLES
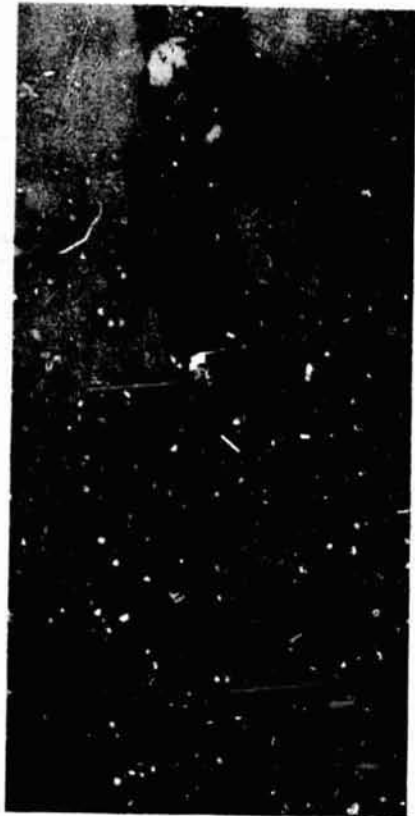
FIGURE 4

Fig. 4. Photographs of assorted recovered "hot short" samples, showing deformation and exploded samples. The interior is granulated, evidence of high vapor pressure along grain boundries, attributed to volitization of vapor deposited metal impurities. Samples were never heated above ~ 3300 K. Note tool marks and degree of deformation.
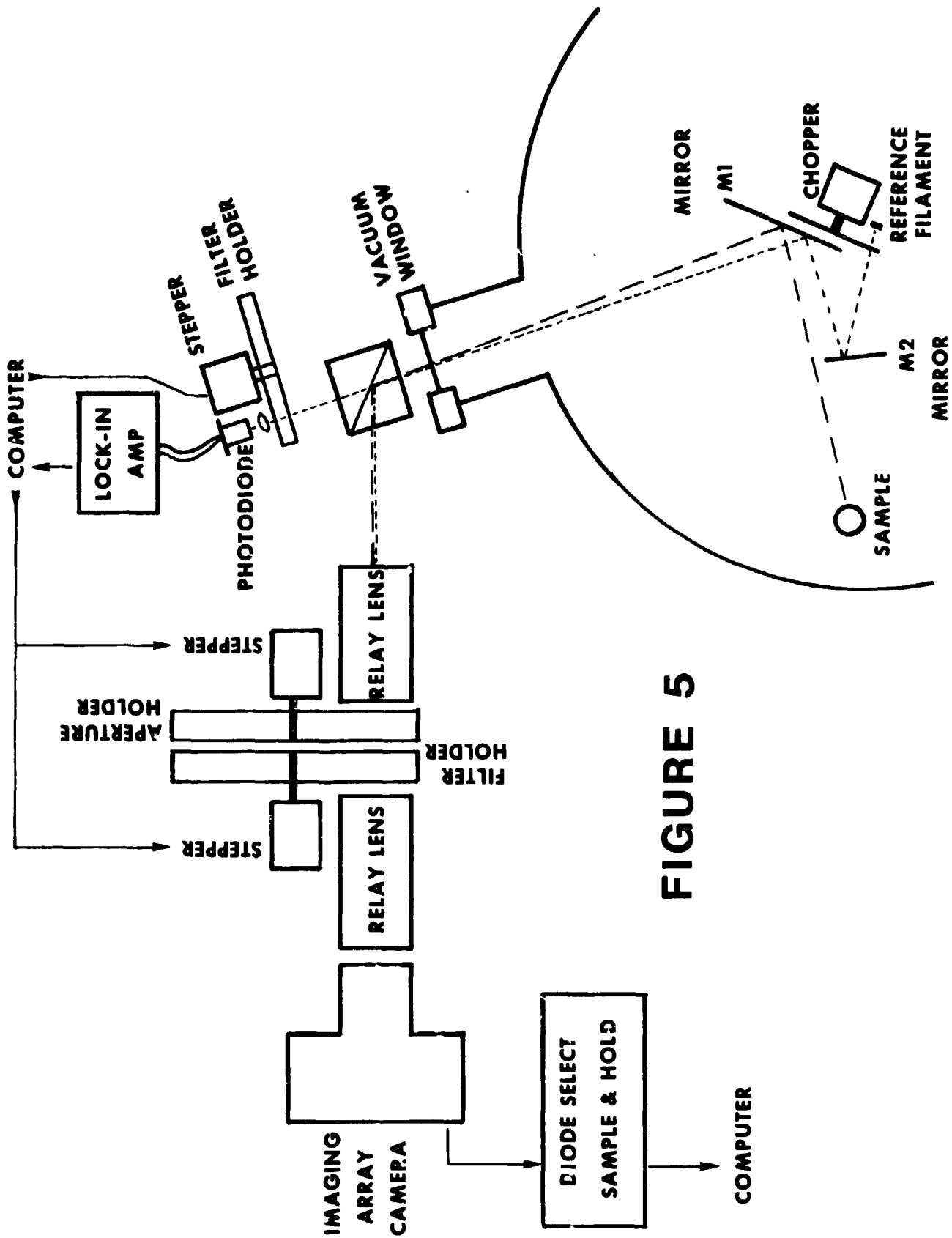
FIGURE 5

Fig. 5. Schematic of optical-mechanical arrangement for a computer operated real time direct reading pyrometric system. See text for discussion.

90

Task 4

High Temperature Thermophysical Properties of Refractory
Materials from Free Cooling Experiments

Jack H. Colwell, Ared Cezairliyan, and Lawrence A. Schmid
Thermophysics Division
Center for Chemical Physics

Summary

Free cooling experiments are to be used to obtain high temperature (1200-4000 K), heat capacities thermal radiative properties, and thermal diffusivities of materials while samples are levitated in a space environment. The data are to be derived from the simultaneous measurement of the total radiant heat loss and the temperature change of spherical samples as they freely cool by radiation alone. Pyroelectric detectors are being investigated for use in making the total radiance measurement. The dynamic response of these detectors have been tested using a millisecond pulse heating apparatus, which permits metal strips to be heated at rates up to 4000 K/s and cooled at rates up to 1500 K/s. In these experiments the pyroelectric detector measures the total normal radiance from an exposed portion of the strip while the radiance temperature of the strip is determined by a high speed pyrometer. A small (~1%) discrepancy between the heating and cooling portions of the experiments is ascribed to the radiance of the strip, not to the behavior of the detector. Normal total emittances derived from these high speed measurements are in excellent agreement with the steady state results of others. The large temperature gradients that can develop in rapidly-cooling spherical samples complicates the interpretation of the free cooling experiments. Mathematical expressions have been derived for values of the physical parameters of materials from the observed time dependence of a sample's surface temperature and total radiance.

Introduction

The objective of this research is to measure the high temperature (1200-4000 K) thermophysical properties, viz., heat capacities, thermal emittances, and possibly thermal diffusivities, of refractory materials. The experiments will exploit the microgravity environment of space to maintain the samples, when hot, without physical contact. RF induction will be used to heat samples, and subsequently, will be used at low power levels to maintain the position of the samples. Samples will be spherical, fabricated in that form as solids and, when liquid, maintained in that form by their surface tension. Experiments will consist of heating the samples to a high temperature in a cold-walled vacuum chamber and then allowing the samples to freely cool by radiation. As the sample cools, its surface temperature will be determined by multicolor radiation pyrometry and the total radiative heat loss will be determined simultaneously by a wide-band pyroelectric detector. The spherical geometry of the sample makes it possible for the total radiance measurement to be made with a single detector. A unique feature of these experiments is that it will permit liquid samples to be followed into the supercooled region all the way to their point of recalescence, thus yielding thermophysical data on supercooled liquids and possibly kinetic data on the solidification process. Containerless liquid refractory metals undergoing free cooling may be ex. ted to supercool by as much as 1000 K.

The cooling rates of the samples will be a function of the temperature and the size of samples[1,2]. For smaller samples, less than 5 mm diameter, at 4000 K, the cooling rate will exceed 1000 K/s. Larger samples, 10 mm diameter at 1500 K will be cooling at rates of the order of 10 K/s.

Because of the dynamic nature of the cooling experiments, temperature gradients will exist within the samples[2]. For metals with a high thermal diffusivity, the total temperature differential from surface to center will be a maximum of tens-of-degrees and will have little effect on the measurements. For materials of lower diffusivity, the temperature differentials can reach hundreds-of-degrees. The temperature differential is, however, an inverse function of the sample radius, so by measuring different sized samples the physical parameters can still be determined. For materials within a particular range of diffusivities, the diffusivity itself can be obtained. The mathematical procedures for determining the values of the material parameters from the experimental observables is described in detail in Part B of this report.

One of the innovative aspects of this work is the use of pyroelectric detectors in dynamic measurements of the total radiance. In Part A of this report we describe the experiments with a pyroelectric detector using the rapid electrical heating apparatus[3] of the Dynamic Measurements Laboratory at NBS. In these experiments, metal strips are heated to a given temperature in less to one second, and then allowed to cool. The temperature is measured pyrometrically and a portion of one surface is viewed by the pyroelectric detector. The pyroelectric detector gives a determination of the total normal emittance of the surface as a function of temperature. The main advantage of this apparatus is that heating and cooling rates can be generated which are several times faster than expected in the free-cooling experiments, thus thoroughly testing the dynamic response of the detector.

The vacuum assembly is nearly complete and the inductive power supply is now on hand for the ground-based simulation of the free-cooling experiments.

This effort is being detained while we wait for the renovation of a new laboratory which will house the experiments. In addition to the experiment described in this report, we are proceeding with the development of a millisecond-resolution two-color pyrometer which will be tested in the simulation experiments.

Part A:

Experimental Procedures

The millisecond pulse heating apparatus[3] used in these experiments impresses a nearly constant voltage across a conductive specimen for a predetermined length of time. The constant voltages are produced by a bank of batteries. Voltage levels are determined by the number of cells in the circuit and an adjustable series resister. By the time the sample reaches the temperature where measurements can begin, $T > 1200$ K, all switching transients have died away and the current is constant except for the slow decrease caused by the increase in the resistance of the specimen as its temperature rises. The duration of the pulse is determined by the circuit characteristics and a temperature limit, and generally is less than one second.

The sample was viewed from one side with a high speed pyrometer which focused on a target area of 0.2 mm diameter at the center of the specimen. The pyrometer uses a photomultiplier tube as a detector, which is alternately exposed to light from the specimen and from a calibrated strip lamp. The sequence of measurements made by the pyrometer is governed by a 12 aperture chopper rotating at 200 Hz. Six apertures admit light from the specimen and are completely open as are two of the apertures admitting light from the lamp. The other four apertures contain two pairs of light attenuators. With each rotation of the chopper, six observations of the specimen are made, interspersed with six reference observations of the lamp. The pairs of reference attenuators used in the chop r are not perfectly matched so their signals show up as two closely spaced doublets on the output (see Fig. 1). The specimen temperature is determined only when the signal lies between the upper and lower reference lines; this constitutes a change of 20-25 percent in the brightness temperature of the specimen depending on

95

the particular temperature range. Temperatures in different ranges are obtained by placing calibrated neutral-density filters in the light path from either the lamp or the specimen. To cover a wide range of temperature, therefore, successive experiments must be run with different filter combinations to cover each successive temperature range.

The electrode assembly that holds the specimen is enclosed in a cylindrical vacuum chamber that is sealed by an O-ring to the bottom plate. The pyrometer views the specimen through a glass window in the side of the vacuum chamber, with the objective lense 15 cm from the specimen. The pyroelectric detector is on the opposite side of the specimen, mounted in a side tube of the vacuum chamber so that no windows need intervene between the specimen and the detector. The light chopper, which is required for pyroelectric detection, is a small (30mm diameter) rotating sector device and is operated at a chopping frequency of 200 Hz. The chopper motor has teflon bearings and has now been operated for tens of hours in a vacuum with no apparent overheating or other ill effects.

The portion of the specimen viewed by the pyroelectric detector is determined by a pair of horizontal knife edges that obscure the top and bottom portions of the strip, so that the detector views only the central portion. The knife edges are mounted on the electrode support assembly, 5 cm from the specimen. The detector is 25 cm from the specimen so the effective sample length is 25% larger than the slit width. The active area of the detector is 1 mm in diameter so the penumbra region increases the effective length of the specimen by 0.2 mm. In these experiments, the gaps between the knife edges were 12 to 15 mm, so any error in the penumbra correction should have a negligible effect on the measurement. Our first experiments were with tungsten strips, 6.35 mm wide, 0.25 mm thick, with

45 mm of length exposed between the electrodes. The opening between the knife edges was 14.6 mm. The outputs of the pyrometer and pyroelectric detector were recorded with two dual-trace oscilloscope-camera combinations. Numerical values were obtained from the photographs using a traveling microscope. A subsequent set of measurements was made with niobium strips of the same size as the tungsten strips and with a knife edge opening of 12.7 mm. For this second set of measurements, data were recorded us‡rg a pair of digital oscilloscopes from which the data could be transferred directly to the PDP-11 computer for processing. The light chopper for the pyroelectric detector was synchronized with the pyrometer chopper so that the two sets of data could be accurately correlated.

The linearity of the response of the pyroelectric detector was established using the inverse distance law. A DXW 1000 W tungsten halogen lamp was used as a light source. The detector was moved over distances from 50.0 to 141.4 cm from the lamp. Measurements were made for irradiances covering more than three orders of magnitude from 32 mW/cm^2 to 20 $\mu W/cm^2$. After values were measured from 50 cm out to 141.4 cm, the lamp power was reduced until the detector signal was the same at 50 cm as it was previously at 141.4 cm. The process was then repeated. These tests showed that the linearity of the detector was better than '% over this wide range. The principal uncertainty in the calibration procedure comes from the geometric distribution of the filament in the light source. The filament of the lamp is a coiled-coil construction, approximately 20 mm long and 5 cm in diameter. There is some uncertainty in the point taken as the origin for the distance measurement. Also, the angle of the lamp to the light path to the detector has an effect, probably due to changes in the amount that the front coils of the lamp obscure the back coils at different detector

distances. Care has to be exercised that the lamp had reached thermal equilibrium after each power change.

Experimental Results

Oscillographic traces of one of the tungsten strip heating experiments are given in Fig. 1. The two oscillograms are of the same experiment with the data collected at different sweep rates on separate oscilloscopes. The upper trace in each oscillogram is the pyrometric temperature signal, increasing to the point where the current is cut off and then decreasing as the specimen cools. The horizontal bands are the pyrometer reference levels, their corresponding radiance temperatures are indicated on the lower oscillogram. The lower trace on each oscillogram is the AC signal from the pyroelectric detector, the peak-to-peak distance being a measure of the total radiant energy. The shape of the pyroelectric signal was puzzling when first observed. With slowly varying light intensities, the two halves of the AC signal are found to be symmetrical, so the asymmetric signal observed in the rapid heating experiments was unexpected. The upper half of the pyroelectric signal in the oscillograms corresponds to light falling on the detector, and the lower half to the detector obscured by the light chopper. A clue to the explanation of the asymmetric signal is found in Fig. 2 which is the response of the detector when suddenly exposed to a constant radiation source. The initial response is a large positive signal during the exposed half of the cycle, and a very small negative signal during the obscured half of the cycle. With time the positive peaks decay and the negative peaks increase until they are symmetrical about the zero signal axis; the relaxation time, τ, for this process is approximately 100 ms for this detector. τ is the thermal relaxation time of the detector and is determined by its heat capacity, c, and the thermal conductance, h,

between the detector element and its mounting, so that $\tau = c/h$. The initial response in Fig. 2 is when the detector is first heated above ambient, the temperature increase is large in the exposed cycle and small in the obscured cycle because little heat is being lost to the heat sink. As time goes on, the average temperature of the detector increases and more heat is being lost to the heat sink, so that the temperature increase during the exposed cycle becomes less and the decrease during the obscured cycle becomes greater, eventually becoming equal when the steady state is reached. For a steady light source, as in Fig. 2, this relaxation phenomena introduces no detectable error (~0.3% resolution in this experiment) between the peak to peak voltages at the beginning of the relaxation period and those after the steady state was reached.

A second relaxation phenomena that affects the signal from a pyroelectric detector is the rise time of the device. For the detector used in these experiments the time constant was approximately 0.5 ms. As a consequence of the rise time and the drop in the signal due to the thermal relaxation, the maximum signal with constant irradiation occurs at approximately 2.0 ms into each half cycle.

The series of experiments on tungsten strips covered thermodynamic temperature ranges from 1500 to 3000 K. Heating rates varied from 4000 K/s at the lowest temperatures to 2000 K/s at the highest temperatures and the corresponding cooling rates ranged from 500 to 1500 K/s. A direct comparison of the normal total radiance with the radiance temperature of the specimen showed that the measured total radiance when the specimen was cooling was always 1 to 2% lower than when it was being heated, except for the region near the maximum temperature.

Thermodynamic temperatures were calculated from the measured radiance temperatures using the spectral emittance data of de Vos[4] and Abbott[5]. The Stefan-Boltzmann law and the total normal radiance data were then used to calculate the total normal emittance of the tungsten strips as a function of temperature. The calculated values agree within 1% with the publish values of Abbott[5] which were obtained in steady-state experiments. This close agreement on an absolute scale is fortuitous for the intensity calibration of our detector was not thought to be that precise.

Fig. 3, 4, and 5 are the results of experiments with niobium strips over three different temperature ranges; these are direct computer plots with no intermediate treatment of the data. The plot of normal total radiance (pyroelectric voltage) versus radiance temperature again shows the slight difference between the heating and cooling curves. The difference increases the longer the sample cools and is largest in the higher temperature ranges. Normal total emittance values from these experiments are within 5-10% of the steady-state values determined by Abbott[5], the discrepancies resulting from the lack of precise values for the normal spectral emittance required to derive thermodynamic temperatures.

Fig. 6 presents the normal total radiance and radiance temperature measurements during the melting of a niobium strip. The radiance temperature shows the flat plateau, characteristic of melting curves in these dynamic experiments[6]; the radiance temperature drops by only 2-3 K in a period of 200 ms. The normal total radiance, however, has a short plateau and then drops off steadily (down 3-4% after 100 ms) until it finally drops precipitously as tne specimen melts through. In an earlier melting experiment the timer switch stopped the current prior to the specimen melting through, the melting plateau was only about 100 ms wide. The measured width of this partially melted sample after the experiment was found to be 1-2% narrower

100

than it was originally because of the melting at the edges. This indicates that the fall off in the normal total radiance in Fig. 6 may be due to a narrowing of the specimen. The radiance temperature is unaffected by the narrowing of the specimen because it is determined by observing a small spot of the center of the strip.

The melting point of niobium is known, 2750 K[7], so the normal total emittance of liquid niobium at the melting point can be evaluated; it is 0.256.

Conclusions and Discussions

The small discrepancy between the heating and cooling portions of the correlation between the pyroelectric voltage and the radiance temperature is thought to due to changes in the total radiance determinations and not due to any error in the temperature measurement. We feel that the change is most likely due to differences in the total radiance of the strip during heating and cooling. While cooling, the strip will be losing energy from the edges of the strip (4% of surface area) as well as the faces so that the average radiance from a face will be less than the radiance from the center of the face. During the heating period this tendency is mitigated in two ways. The rate of heating is much faster than the rate of cooling, so that the temperature gradients will not be as fully developed. More importantly, however, when heating, the current will tend to follow the path of lowest resistance, i.e. the coolest path, and will suppress the development of the temperature gradients. There is the possibility that the discrepancy is inherent in the pyroelectric detector. Because of the finite rise time (and the thermal relaxation) of the device, a different voltage signal could be obtained for rapidly increasing and decreasing signals. This possibility

has not been investigated, but if it were a major contributing factor to the observed discrepancy, it would be expected to be largest near the peak of the temperature curve were the signals are changing most rapidly; this is not the case. In any case, the heating and cooling rates in these strip heating experiments are several times larger than those that will be encountered in the free-cooling experiments, so errors from this source will be minimal.

The principal aim of this stage of our research is to establish that pyroelectric detectors can be used to make accurate total irradiance measurements in high speed experiments. These experiments have accomplished that.

References

1. J.H. Colwell, NBSIR 79-1767, NBS: Properties of Electronic Materials, J.R. Manning, Ed., p. 103.

2. J.H. Colwell, NBSIR 80-2082, NBS Materials Measurements, J.R. Manning, Ed., p. 88

3. Ared Cezairliyan, J. Res. Natl. Bur. Stand., 75C, 7(1971).

4. J.C. DeVos, Physica, 20 690 (1954).

5. G.L. Abbott: Total Normal and Total Hemispherical Emittance of Polished Metals, Part III. WADD Tech. Rep. 61-94, U.S. Air Force, Sept. 1963, W.J. Parker and G.L. Abbott, NASA SP-55, S. Katzoff, Ed., p. 11.

6. Ared Cezairliyan, J. Res. Nat'l. Bur. Stand., 77A, 333 (1973).

7. Ared Cezairliyan, High Temp.-High Pres. 4, 453 (1972).

1930 K

1680 K
1530 K
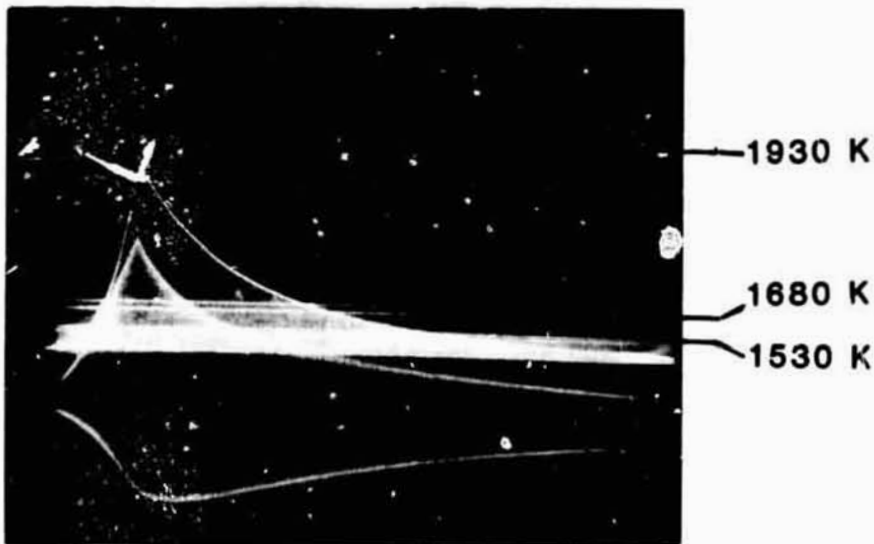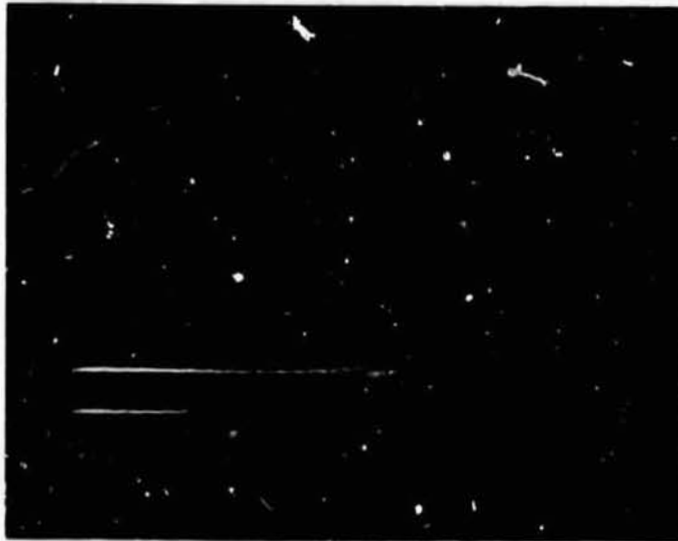
Fig. 1   Tungsten strip heating experiment. Two oscillograms of the
         same experiment at different sweep rates, 50 ms/cm in the top
         oscillogram, 200 ms/cm in the bottom. The top curve in each case
         is the pyrometer output, the bottom pair of curves is the ac
         pyroelectric voltage. The horizontal traces are the reference
         levels of the pyrometer and their corresponding radiance temperatures
         are indicated on the lower oscillogram. The radiance temperature at
         the peak is 1912 K which corresponds to a thermodynamic temperature
         of 2056 K.
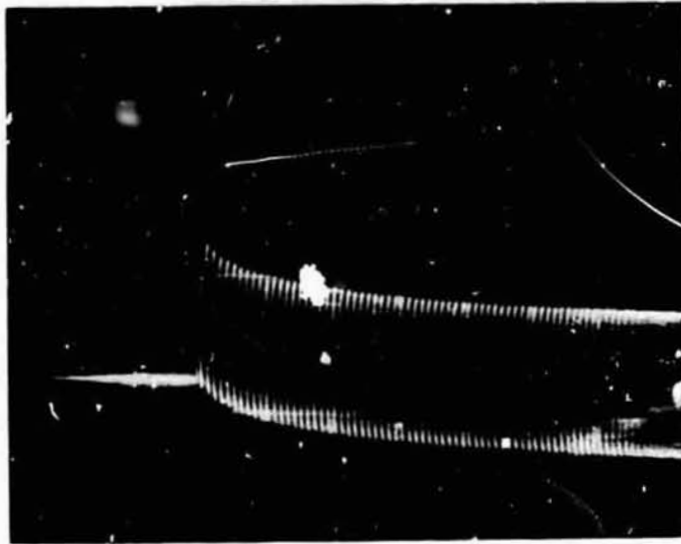
Fig. 2   The pyroelectric response upon instantaneous exposure to a
constant light source. Sweep rate is 50 ms/cm, pyroelectric
chopping frequency is 200 Hz. Variation of the two voltage levels
is due to thermal time constant of the detector; the peak-to-peak
voltage is not affected by the relaxation process.
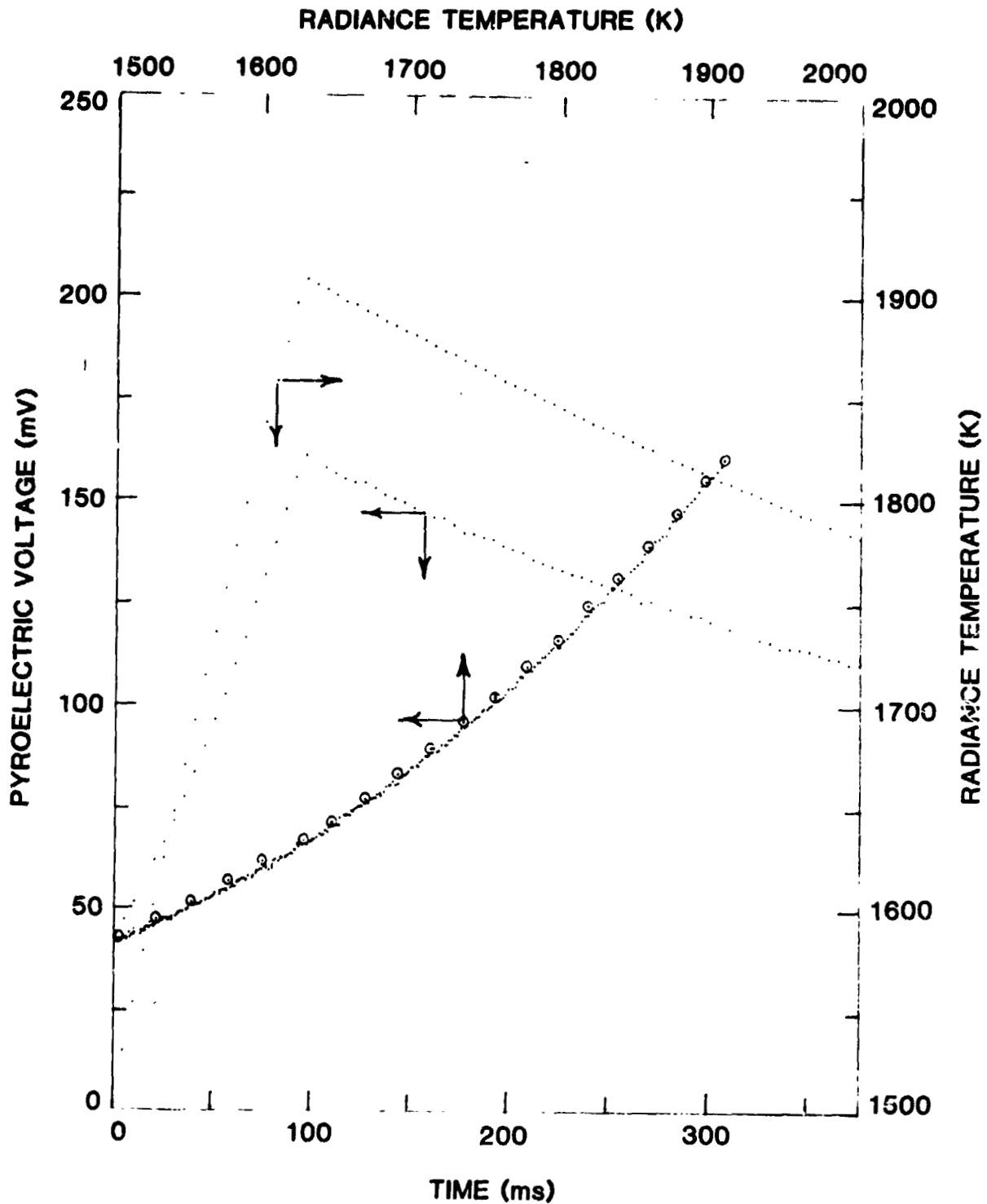
Fig. 3   Niobium-strip heating experiment to 1900 K. Arrows on curv s
indicate scales to be used. The pyroelectric voltage (proportional
to normal total radiance) and the pyrometrically determined radiance
temperature are shown as a function of time, and also plotted
against each other. On the latter curve the encircled points are
those with the temperature increasing. Near the maximum temperature,
the heating rate is 4200 K/s and the cooling rate is 500 K/s.
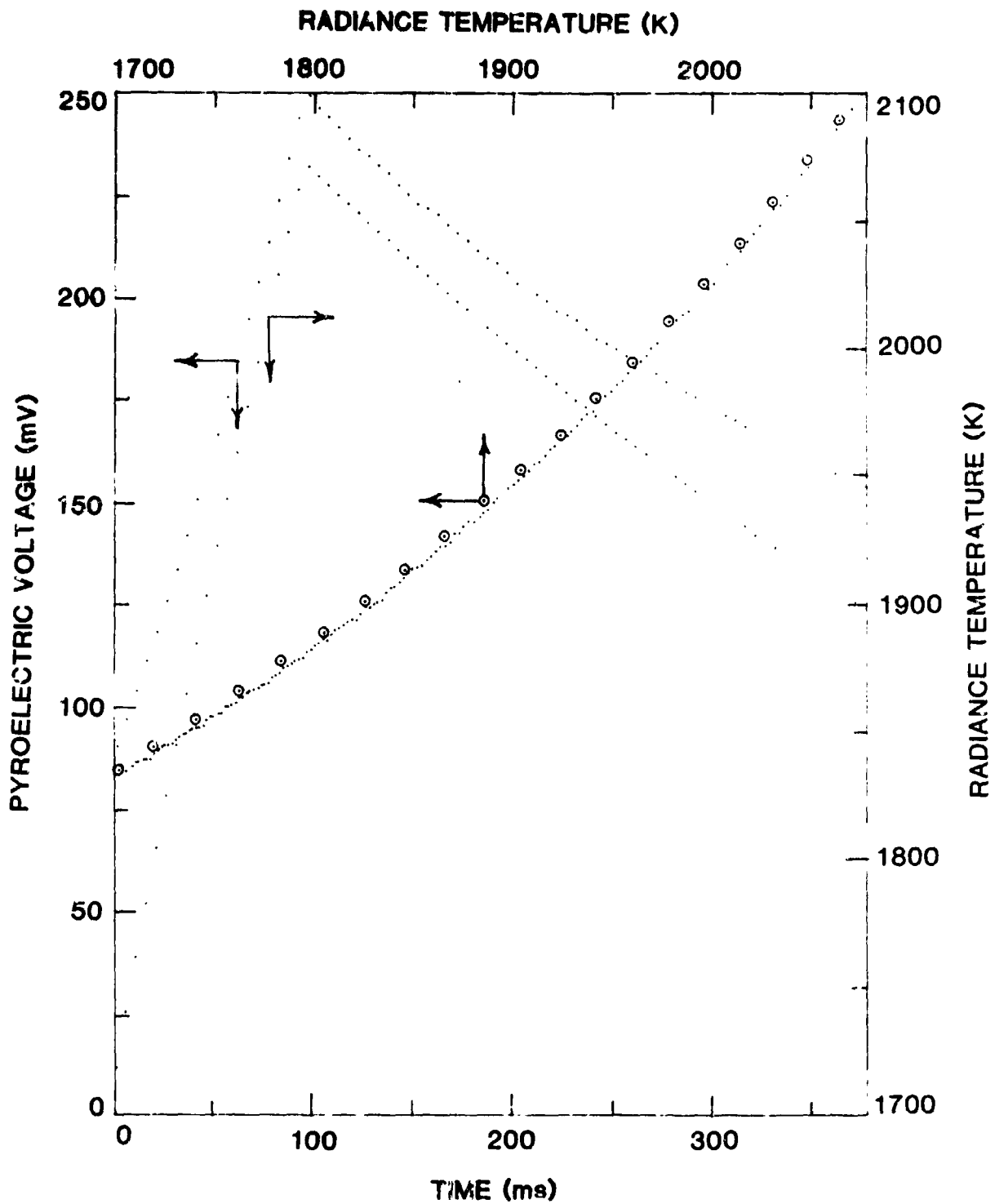
Fig. 4   Niobium-strip heating experiment to 2100 K. Arrows on curves
         indicate scales to be used. The pyroelectric voltage (proportional
         to normal total radiance' and the pyrometrically determined radiance
         temperature are shown as a function of time, and also plotted
         against each other. On the latter curve the encircled points are
         those with the temperature increasing. Near the maximum temperature,
         the heating rate is 3600 K/s and the cooling rate is 700 K/s.
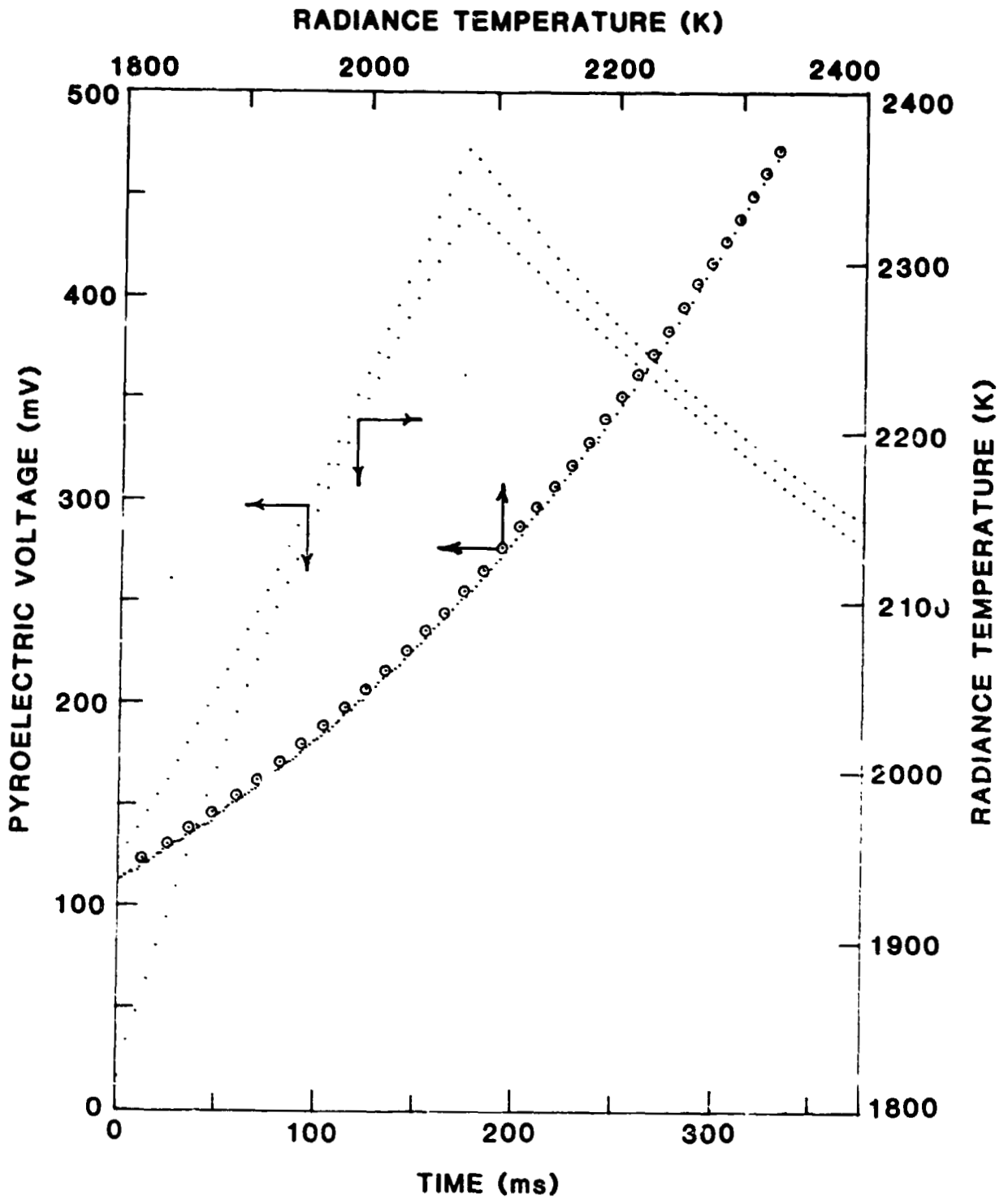
Fig. 5   Niobium-strip heating experiment to 2375 K. Arrows on curves
indicate scales to be used. The pyroelectric voltage (proportional
normal total radiance) and the pyrometrically determined radiance
temperature are shown as a function of time, and also plotted
against each other. On the latter curve the encircled points are
those with the temperature increasing. Near the maximum temperature,
the heating rate is 200 K/s and the cooling rate is 1200 K/s.
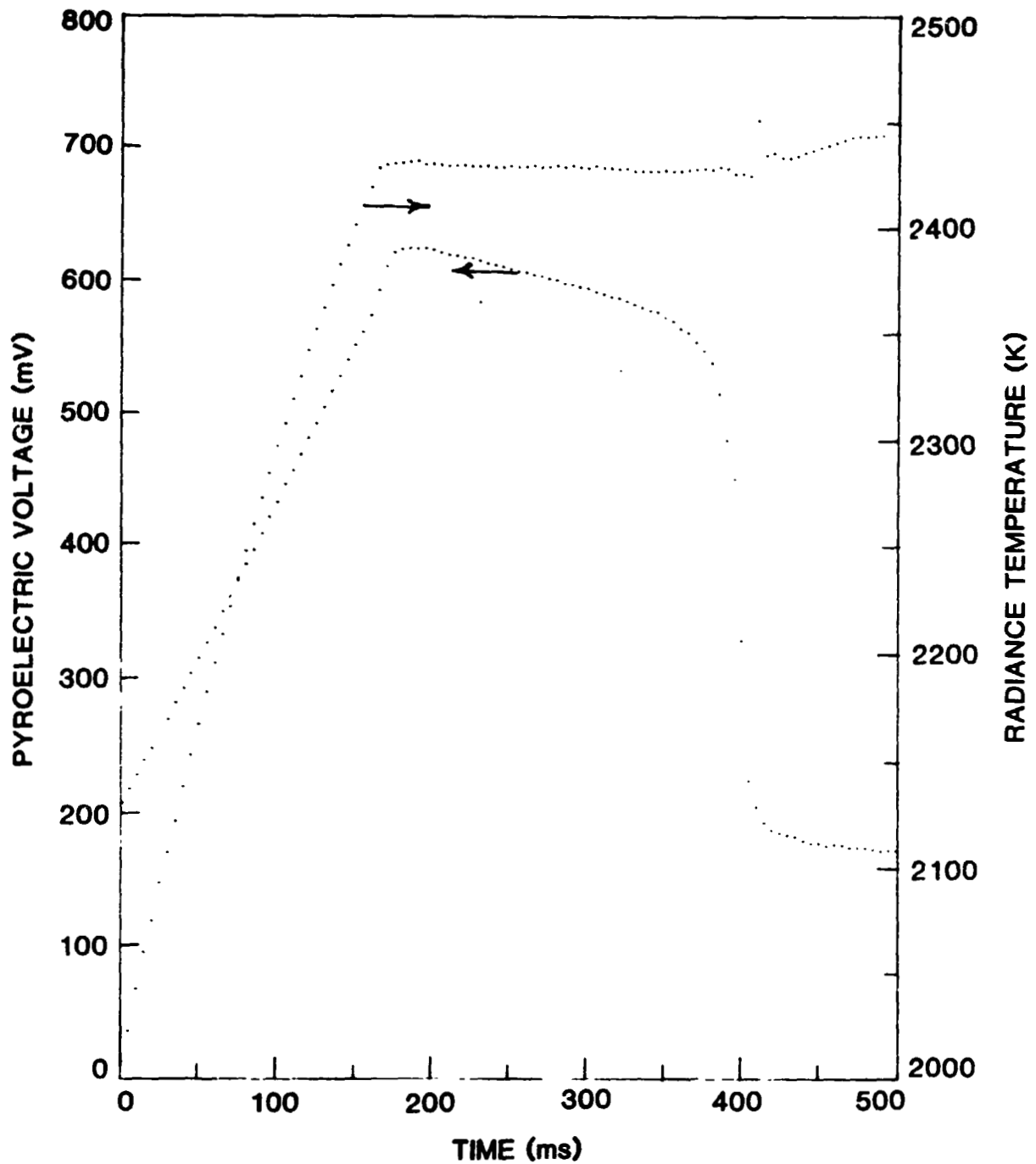
Fig. 6   Niobium-strip melting experiment. The pyroelectric voltage
(proportional to normal total radiance) and the pyrometrically
determined radiance temperature are shown as a function of time.
The plateaus of the curves indicate the period where the surface of
the specimen is melting. The precipitous drop in the pyroelectric
voltage indicates the point that the specimen melts through and
collapses. The melting point of niobium is 2750 K.

Part B:

Mathematical Analysis of the Free-Cooling Sphere

1. Overview of the Analysis

The free-cooling calorimetric method discussed in this report aims at the determination of the temperature dependence of the thermal parameters (heat capacitance, diffusivity, and emittance) of refractory materials at high temperatures by optical observations of the time dependence of the surface temperature $T_s(t)$ and the radiance $E(t)$ (radiated heat flux per unit area) of a hot solid sphere of the material as it cools down. (The possibility of melting will not be discussed in what follows. This will be the subject of future research.)

The emittance $\varepsilon(T_s)$ of the surface is simply given by

$$\varepsilon = E/(\sigma T_s^4) \tag{1}$$

where σ is the Stefan-Boltzmann constant. Thus the real problem is to express the diffusivity α and the heat capacity per unit volume c in terms of $E(t)$ and $T_s(t)$. In the limit $\alpha \to \infty$ (or $R \to 0$ where R is the radius of the spherical sample), the temperature throughout the sample can be taken equal to T_s, and c can be found from the following simple relation:

$$-(4\pi R^3/3)c\,dT_s/dt = 4\pi R^2 E \quad \text{or} \quad c = -3E/R\dot{T}_s \tag{2a,b}$$

where $\dot{T}_s \equiv dT_s/dt$. For finite α, however, the temperature inside the sphere is higher than T_s, and so eq. 2b can only be the leading term in a more complicated expression containing higher-order correction terms involving α. Such an expression for c will be derived in what follows, first for the case of constant c and α (cf. eqs. 30 and 37), and then for the case of temperature-dependent parameters $c(T)$ and $\alpha(T)$ (cf. eqs. 56 and 57). Similar expressions will be derived for α as a function of the time derivatives of T_s and E (cf. eqs. 35

109

and 55).

An essential feature of the free-cooling method described in this report is that the temperature field within the sample is assumed to be unknown at the beginning of the experiment. Thus the heater, be it an induction coil, furnace, or some other device, need not be precisely controlled in order to assure that a specified quantity of energy be injected into the sample, or that a specified initial interior temperature field be achieved. The price that must be paid for this freedom is that the readings of $T_s(t)$ and $E(t)$ for a time interval $\Delta t \sim R^2/\alpha$ at the beginning of an observational run after the heater is turned off cannot be used to determine $\alpha(T)$ and $c(T)$, because T_s and E are too sensitive to the details of the unknown initial interior temperature field. It is only when the initial transients have died out and the thermal behavior of the sample enters the "post-transient regime" that the expressions for α and c in terms of $E(t)$ and $T_s(t)$ (and their time derivatives) that are derived in this report can be applied. For the sample sizes contemplated, however, only a couple of seconds are required for the transients to die out in the case of a poor thermal conductor like uranium dioxide, and this is to be compared with a total observation time of nearly 30 seconds. In the case of metal samples the time required for the transients to die out is a much smaller fraction of the total observation time. These estimates are discussed at the end of Section 3.

In order to relate the analysis of this report to the existing literature on the analysis of free-cooling, it should be noted that there are three different kinds of cooling problem which must be clearly distinguished:

(1) the <u>predictive</u> or initial-value problem in which the initial temperature field within the body is given, and it is necessary to calculate $T_s(t)$ knowing the functional dependence $E(T_s)$ of the radiance on the surface temperature;

(2) the _inverse_ problem, in which $E(T_s)$ is known, $T_s(t)$ is given, and it is necessary to calculate the initial interior temperature field;

(3) the _calorimetric_ problem, in which $E(t)$ and $T_s(t)$ are given, and it is necessary to calculate $c(T)$ and $\alpha(T)$. A knowledge of the initial interior temperature field is neither given nor desired. (This category of problem is sometimes also referred to in the literature as the "inverse problem".)

This report will concern itself only with the first and third categories. Only the weak form" of the predictive problem will be discussed, by which is meant the prediction of $T_s(t)$ (and the interior temperature field) in the post-transient regime. Inasmuch as $T_s(t)$ in this regime is determined by the thermal parameters alone, it is possible (in the case of constant parameters) to derive a universal cooling law for this regime. This law has its simplest form when t is expressed as a function of T_s, and an explicit expression for $t(T_s)$ is given for the case of arbitrary (but constant) thermal parameters (cf. eqs. 26 and 27). In the weak form of the predictive problem, the radiance $E(T_s)$ may be regarded as a forcing function that is producing a "forced decay" in $T_s(t)$. The "free decay modes" arising from an arbitrarily specified interior temperature field have died out, and the expression for the interior temperature $T(r,t)$ can be characterized by a form-invariant functional dependence on the forcing function $E(T_s)$ or, equivalently, on T_s. That is,

$$T(r,t) = T[r, T_s(t)]. \tag{3}$$

Such an expression for $T(r,t)$ is given, which has the form of the sum of polynomials in r multiplied by powers of $T_s(t)$ in which all coefficients are time-independent numbers (cf. eqs. 14 and 23). This solution corresponds to the "particular solution" in the theory of linear differential equations, but the present problem is nonlinear because the forcing function $E(T_s)$ is a function of the unknown surface temperature.

2. Outline of Solution Method Employed

A four-step procedure is employed to solve the weak form of the predictive problem: (1) First the sphere is imagined to be immersed in a controlled temperature bath with a given time-dependent temperature $T_s(t)$. This is the only boundary condition imposed (except for the requirement that the interior temperature be everywhere finite). This is a linear problem whose solution can be expressed as a convolution integral. This integral is then transformed so as to cast the solution into a simple and novel form in which the temperature is expressed as an infinite (but subsequently truncated) sum of characteristic polynomials in r of degree $(2n+1)$, each of which is multiplied by $(-1)^n d^n T_s/dt^n$. Thus the time derivatives of the surface temperature can be regarded as "driving" the solution for the interior temperature. (2) the next step consists of imposing the boundary condition that relates $(\partial T/\partial r)_s$ to $E(T_s)$. When the solution to the linear problem is substituted into this boundary condition, the boundary condition assumes the form of an ordinary differential equation in $T_s(t)$ that is linear except for the fact that the forcing function $E(T_s)$ is a nonlinear function of the dependent variable T_s. The differential equation is of infinite order, but is truncated to fourth order. (3) An iterative procedure is used to find a self-consistent solution to this nonlinear differential equation in which dT_s/dt and the higher derivatives are expressed as sums of powers of T_s. This is the "particular solution" that characterizes the post-transient regime. (4) The equation $dT_s/dt = F(T_s)$ is integrated to give an explicit expression for $t(T_s)$, which is the universal cooling curve for a hot sphere in the post-transient regime.

The same ordinary differential equation that results from the imposition of the boundary condition involving the radiance E also serves as the basis of the solution of the calorimetric problem, except that $E(t)$ and $T_s(t)$

112

(and hence all of its derivatives in the ordinary differential equation) must now be regarded as known functions, so that the differential equation becomes an <u>algebraic</u> equation in which the unknowns are α and c. If α and c are constants, then it is only necessary to know the values of E and T_s at two moments during the cooling in order to construct and solve a system of two algebraic equations for the two unknowns α and c. However, an alternative procedure for solving for α and c is employed that leads to expressions for them that lend themselves to an easily automated iterative solution.

The problem of finding the temperature dependence of variable parameters $\alpha(T)$ and $c(T)$ is solved by introducing new dependent and independent variables that reduce the nonlinear partial differential equation to the same form as that for constant parameters except for the presence of a very small effective heat source density whose effect can be neglected. The same solution procedure is followed as in the case of constant parameters, and the end result is expressions for $\alpha(T)$ and $c(T)$ in terms of $E(t)$ and $T_s(t)$ (and their derivatives that can be solved by a simple iterative procedure.

There appears to be no discussion of the weak form of the predictive problem in the existing literature, except for the limiting case in which the interior temperature may be considered to be constant throughout the sample. The strong form of the predictive problem, i.e. the initial value heat problem, has of course a superabundant literature.[1]

The calorimetric problem has been investigated by a small group of mathematicians[2-10] , but the investigations have been limited either to two <u>constant</u> parameters, or else <u>only one</u> variable parameter, and the resulting expressions are complicated and difficult to solve numerically. One important cause for this complication is the fact that these authors insisted on

maintaining the requirement of uniform initial interior temperature, and the concept of the post-transient regime was not introduced. Without limiting the analysis to this regime, and simultaneously rigidly maintaining specified initial conditions, the problem becomes overdetermined, and in general ill-posed.

3. Predictive Problem for Constant Thermal Parameters

Although the primary purpose of this report is to present the solution of the calorimetric problem, the necessary analysis must be confronted already in the simplest predictive problem (i.e. the one for constant parameters). The solution of this problem also provides estimates of the numerical values of various quantities that become observational data in the calorimetric problem.

The partial differential equation governing the flow of heat in a body in the absence of any interior heat sources is

$$\underline{\nabla} \cdot (k \, \underline{\nabla} \, T) = c \, \partial T / \partial t \qquad (4)$$

where k is the thermal conductivity and c is the heat capacity per unit volume. (Strictly speaking, since c is the product of the mass density and the constant-pressure specific heat, and because the mass density is a function of temperature, c is the heat capacity of the quantity of material that occupies unit volume at some given reference temperature, and is not strictly the heat capacity per unit volume at an arbitrary temperature, although this simplified nomenclature will be used in what follows. If $\rho(t)$ is the mass density, then the constant-pressure specific heat $C_p = c/\rho$. C_p and ρ enter into the formalism only as the product $c = \rho C_p$.)

The boundary condition that must be applied to eq. 4 is obtained by noting that the integral of the right side of eq. 4 over the volume occupied by the hot sphere is equal to the rate of decrease of heat content of the sphere, and

114

so must be equal to $4\pi R^2 E$ where the radiance E is the radiated heat flux per unit area. Applying Gauss' Theorem to the volume integral of the left side of eq. 4, the following boundary condition results:

$$-k(\partial T/\partial r)_s = E(t) \qquad \text{(calorimetric problem)} \quad (5a)$$
$$= \epsilon \sigma T_s^4 \qquad \text{(predictive problem)} \quad (5b)$$

where the subscript s designates quantities evaluated at the surface, σ is the Stefan-Boltzmann constant, and ϵ is the emittance. This boundary condition assumes that the sphere is radiating into a "cold vacuum", i.e. a vacuum at absolute zero of temperature. This assumption is convenient, but in no way essential for what follows.

With proper scaling, all quantities can be made dimensionless, and all parameters (including dimensionless ones) can be eliminated from the equations, reducing them to a universal form that applies to spheres of all sizes with all possible (constant) thermal parameters. In order to do this, it is necessary to introduce a characteristic length r_1, time interval t_1, and temperature T_1. The first two are self-evident:

$$r_1 \equiv R \quad ; \quad t_1 \equiv R^2/\alpha. \qquad (6a,b)$$

The definition of the characteristic temperature T_1 is not so obvious. Various definitions can be found in the literature, such as the highest or lowest temperatures encountered in the problem, or an equipment-related temperature such as that of a furnace to which the sample is exposed. If, however, one wishes to remove even dimensionless constants from the equations, only the following definition will suffice:

$$T_1 \equiv (k/R\epsilon\sigma)^{1/3}. \qquad (6c)$$

This characteristic temperature is determined by the size and thermal properties of the sample, and is independent of the starting conditions of the experiment or of the properties of the environment to which the sample is exposed. For a

tungsten sphere for which $R = 1$ cm, $T_1 = 17,300$ K which is nearly five times the melting temperature (3653 K), whereas for a sphere of uranium dioxide of the same size, $T_1 = 3650$ K, which is only 500 K higher than the melting temperature (3151 K).

The dimensionless varia¹les (designated by a circumflex) corresponding to the characteristic magnitudes defined above are

$$\hat{r} \equiv r/R \; ; \qquad \hat{t} \equiv \alpha t/R^2 \; ; \qquad \hat{T} \equiv T/T_1 \; ; \tag{7a,b,c}$$

and the corresponding equation and boundary condition can be written as follows:

$$\partial^2(\hat{r}\hat{T})/\partial\hat{r}^2 - \partial(\hat{r}\hat{T})/\partial\hat{t} = 0 \tag{8a}$$

$$- (\partial\hat{T}/\partial\hat{r})_s = \hat{E}(\hat{t}) \qquad \text{(calorimetric problem)} \tag{8b}$$

$$= \hat{T}_s^4 \qquad \text{(predictive problem)} \tag{8c}$$

where

$$\hat{E}(\hat{t}) \equiv E(t) \; [k(T_1/R)]^{-1} = RE/kT_1. \tag{9}$$

The first expression for $\hat{E}$ above shows that it may be regarded as a dimensionless heat flux for which the scaling flux is $[k(T_1/R)]$, i.e. the flux driven by the temperature gradient t_1/R.

As noted in Section 2, the first step in the solution of eq. 8 above consists of replacing the boundary condition (8c) by the requirement that at the surface of the sphere $\hat{T}$ be equal to the (as yet unspecified) temperature $\hat{T}_s(\hat{t})$ which is regarded as the forcing function that drives the interior temperature $\hat{T}(\hat{r},\hat{t})$. It is more convenient to deal with the temperature difference $(\hat{T} - \hat{T}_s)$, and to this end the dependent variable is defined as

$$\theta(\hat{r},\hat{t}) \equiv \hat{r}[\hat{T}(\hat{r},\hat{t}) - \hat{T}_s(\hat{t})]. \tag{10}$$

Thus the equations to be solved are

$$\partial^2\theta/\partial\hat{r}^2 - \partial\theta/\partial\hat{t} = \hat{r} \, dT_s/d\hat{t} \qquad\qquad (11a)$$

$$\theta(0,\hat{t}) = \theta(1,\hat{t}) = 0 . \qquad\qquad (11b)$$

This is a linear inhomogeneous equation with Dirichlet-type boundary conditions that is driven by the forcing function $\hat{r} \, d\hat{T}_s/d\hat{t}$. It is easily confirmed that the solution can be written in the following form:

$$\theta(\hat{r},\hat{t}) = \frac{2}{\pi} \sum_{m=1}^{\infty} \frac{(-1)^m}{m} \sin(m\pi\hat{r}) \; A_m(\hat{t}) \; \exp[-(m\pi)^2\hat{t}] \qquad\qquad (12a)$$

where

$$A_m(\hat{t}) = \int_{-\infty}^{\hat{t}} \exp[(m\pi)^2 t'] \; [d\hat{T}_s(\hat{t}')/d\hat{t}'] \; d\hat{t}' . \qquad\qquad (12b)$$

An alternative form results from splitting the integral of (12b) into two parts as follows:

$$A_m(\hat{t}) = B_m + \tilde{A}_m(\hat{t}) \qquad\qquad (13a)$$

where B_m is a constant given by

$$B_m = \int_{-\infty}^{0} \exp[(m\pi)^2\hat{t}'] \; [d\hat{T}_s(\hat{t}')/d\hat{t}'] \; d\hat{t}' \qquad\qquad (13b)$$

and

$$\tilde{A}_m(\hat{t}) = \int_{0}^{\hat{t}} \exp[(m\pi^2) \, \hat{t}'] \; [d\hat{T}_s(\hat{t}')/d\hat{t}'] \; d\hat{t}' . \qquad\qquad (13c)$$

If eq. 13a is substituted into eq. 12a, we have the more familiar form of the solution in which the terms involving B_m describe the rapidly decaying normal modes, and the summation involving $\tilde{A}_m(\hat{t})$ describes the inhomogeneous part of the solution that is driven by the forcing function $\hat{r} \, d\hat{T}_s/d\hat{t}$ on the right side

117

of eq. 11a. Because $\tilde{A}(0) = 0$, it is evident that only the part of the solution (12a) that involves the B_m is non-zero at $\hat{t} = 0$, and that $[(-1)^m B_m/m]$ are the Fourier coefficients for a sinusoidal expansion of $\theta(\hat{r},0)$. The longest-lived normal mode ($m=1$) decays like $\exp(-\pi^2\hat{t}) = \exp[-(\pi^2\alpha/R^2)t]$, so when $t \sim R^2/\alpha$, this longest-lived mode has a magnitude of order $\exp(-\pi^2) = 5 \times 10^{-5}$, so it is safe to say that by this time the post-transient regime has become established.

When the solution (12a) is written using (12b) rather than (12), the entire solution is regarded as "driven", with the effects of the driving force reaching back to $\hat{t} = -\infty$. That is, one effectively takes $\hat{t} = -\infty$ to mark the beginning of the experiment, and takes the position that for all finite $\hat{t}$ the decaying homogeneous solution has long since died away, leaving only the inhomogeneous driven solution. For a solid sphere whose interior temperatures can be influenced only by the environment to which its surface is exposed, this is a physically more natural point of view than that posed by the initial-value problem, which requires that the initial interior temperature field be specified, rather than the past history of the surface temperature.

If the derivative in the integrand of (12b) is expanded in powers of $(\hat{t}' - \hat{t})$, the integration can be carried out explicitly and the solution assumes the form

$$\theta(\hat{r},\hat{t}) = \sum_{n=1}^{\infty} (-1)^n \hat{T}_s^{(n)}(\hat{t}) P_n(\hat{r}) \tag{14a}$$

where

$$\hat{T}_s^{(n)}(\hat{t}) \equiv d^n \hat{T}_s/d\hat{t}^n \tag{14b}$$

and

$$P_n(\hat{r}) \equiv 2 \sum_{m=1}^{\infty} (-1)^{(m+1)} (m\pi)^{-(2n+1)} \sin(m\pi\hat{r}). \tag{14c}$$

The $P_n(\hat{r})$ are polynomials of degree $(2n+1)$ that have the following properties:

$$P_n(0) = 0 \quad \text{for } n \geq 0; \tag{15}$$

$$P_o(1) = 1, \tag{16a}$$

$$P_n(1) = 0 \quad \text{for } n > 0; \tag{16b}$$

$$\left. \begin{array}{l} d^2P_o/d\hat{r}^2 = 0, \\[2mm] d^2P_n/d\hat{r}^2 = - P_{n-1} \quad \text{for } n > 0 \; . \end{array} \right\} \quad \text{for } 0 \leq r \leq 1 \qquad \begin{array}{l} (17a) \\[2mm] (17b) \end{array}$$

The first few of these polynomials can be found in handbooks. (See, for example, p. 87 of reference 11.) Property (17b) can then be used to generate successively higher-order polynomials by double integration using properties (15) and (16b) to determine the two constants of integration. The four lowest-order polynomials are listed below:

$$P_o(\hat{r}) = \hat{r} \tag{18a}$$

$$P_1(\hat{r}) = \hat{r}(1-\hat{r}^2)/6 \tag{18b}$$

$$P_2(\hat{r}) = \hat{r} \, (7 - 10 \, \hat{r}^2 + 3 \, \hat{r}^4)/360 \tag{18c}$$

$$P_3(\hat{r}) = \hat{r}(31 - 49\hat{r}^2 + 21 \, \hat{r}^4 - 3 \, \hat{r}^6)/15,120 \tag{18d}$$

$$P_4(\hat{r}) = \hat{r}(381-620 \, \hat{r}^2 + 294 \, \hat{r}^4 - 60 \, \hat{r}^6 + 5 \, \hat{r}^8)/1,814,400. \tag{18e}$$

Using the property (17b), it is a very easy matter to show by direct substitution that the differential equation (11a) is satisfied. The properties (15) and (16) guarantee that the boundary conditions (11b) are satisfied.

The form of the solution given in (14) represents a different way of stating that the interior temperature field is determined by the history of of the surface temperature. Whereas the form of the solution given in (12) represents this history by an integral reaching into the distant past (with a kernel that provides "memory loss"), the form given in (14) represents this history by means of all of the time derivatives of the surface temperature

calculated at the present instant of time. Instead of the ever-diminishing influence of the surface temperature as one reaches deeper into the past, it is now the ever-diminishing signific ace of the higher-order time derivatives of surface temperature as the order of the derivative increases. This decreasing influence of $\hat{T}_s^{(n)}$ as n increases results from the fact that P_n decreases as n increases. For this reason, a truncation of the infinite series in (14a) is feasible in the case of a nume 'cal calculation. In the calculation described in this report, only the terms of (14a) up to and including n = 4 were retained.

The infinite set of polynomials P_n does not span the entire class of continuous functions on the interval $0 \leq \hat{r} \leq 1$. The set is, however, sufficiently large to include all permissible solutions to (11). To see this, it should be noted that since $(\theta/\hat{r}) = \hat{T} - \hat{T}_s$, the set $(P_n/\hat{r})$ ought to be capable of describing the most general form of $\hat{T} - \hat{T}_s$ inside the sphere, and on the surface should vanish. This latter requirement is satisfied in view of (16b) and the fact that n = 0 is excluded from the summation in (14a). As to the completeness of the et $(P_n/\hat{r})$, it should be noted that (as (18) indicates) it is isomorphic to the set of all even powers of $\hat{r}$, which corresponds to the requirement that $\underline{\nabla}\,\hat{T} = 0$ at the center of the sphere, which in turn follows from the fact that, in the absence of a point source or sink at the origin, the heat flux must vanish there.

The second step of the solution method that was outlined in Section 2 above consists of substituting (14) into the boundary condition (5b) in order to obtain an ordinary differential equation that determines the time dependence of $\hat{T}_s(t)$. The dimensionless form of the boundary condition (5) is

120

$$-(\partial\theta/\partial\hat{r})_{\hat{r}=1} \;=\; \hat{E}(\hat{t}) \qquad \text{(calorimetric problem)} \qquad \text{(19a)}$$

$$=\; \hat{T}_s^4. \qquad \text{(predictive problem)} \qquad \text{(19b)}$$

Differentiation with respect to $\hat{r}$ of the solution given in (14), and subsequent substitution into (19) yields the following result:

$$\sum_{n=1}^{\infty} (-1)^n \; [2^{2n} B_n/(2n)!] \; d^n \hat{T}_s/d\hat{t}^n \;=\; \hat{E}(\hat{t}) \qquad \text{(calorimetric problem)} \qquad \text{(20a)}$$

$$=\; \hat{T}_s^4 \qquad \text{(predictive problem)} \qquad \text{(20b)}$$

where B_n are the Bernoulli numbers, which are tabulated in sundry handbooks[12]. The first 7 of these are

$$B_1 = 1/6, \; B_2 = 1/30, \; B_3 = 1/42, \; B_4 = 1/30, \; B_5 = 5/66, \; B_6 = 691/2730,$$

$$B_7 = 7/6. \qquad \text{(21)}$$

If the series in (20) is truncated at $n = 4$, the following ordinary differential equation results:

$$\frac{1}{4725}\frac{d^4 \hat{T}_s}{d\hat{t}^4} - \frac{2}{945}\frac{d^3 \hat{T}_s}{d\hat{t}^3} + \qquad\qquad\qquad\qquad \text{(22a)}$$

$$+ \frac{1}{45}\frac{d^2 \hat{T}_s}{d\hat{t}^2} - \frac{1}{3}\frac{d\hat{T}_s}{d\hat{t}} \;=\; \hat{E}(\hat{t}) \qquad \text{(calorimetric problem)}$$

$$=\; \hat{T}_s^4 \;. \qquad \text{(predictive problem)} \qquad \text{(22b)}$$

In the calorimetric problem, $T_s^{(n)}(t)$ and $E(t)$ are given functions of time, so when (22a) is written in dimensional form it becomes an algebraic equation in the two unknowns α and c. This case is discussed in Section 4 below. In the predictive problem however, one must solve the ordinary differential equation (22b), which would be linear except for the fact that the forcing function $\hat{T}_s^4$ is a nonlinear function of the dependent variable $\hat{T}_s$. Except for this nonlinearity, one could assert that the solution of (22b) consists of the sum of a homogeneous part that requires a knowledge of four initial conditions, and a particular solution that

is entirely determined by the forcing function and is independent of the initial conditions. The form of (14a) shows that the initial conditions of (22b) determine the initial interior temperature field, and vice versa. This homogeneous solution has completely died away by the time the system has entered the post-transient regime that is completely determined by the forcing function $\hat{T}_s^4$. The "particular solution" that describes this regime can be found analytically by an iterative process which leads to a set of self-consistent expressions for the derivatives $\hat{T}_s^{(n)}$ as functions of $\hat{T}_s$ alone, i.e., there are no arbitrary degrees of freedom that must be specified by initial conditions or any other condition. These self-consistent expressions are the following:

$$\hat{T}_s^{(1)} = -\left[3 \hat{T}_s^4 - \frac{12}{5} \hat{T}_s^7 + \frac{12}{25} \hat{T}_s^{10} + \frac{432}{875} \hat{T}_s^{13} \right] , \tag{23a}$$

$$\hat{T}_s^{(2)} = 36 \hat{T}_s^7 - \frac{396}{5} \hat{T}_s^{10} + \frac{1512}{25} \hat{T}_s^{13} , \tag{23b}$$

$$\hat{T}_s^{(3)} = -\left[756 \hat{T}_s^{10} - \frac{14904}{5} \hat{T}_s^{13} \right] , \tag{23c}$$

$$\hat{T}_s^{(4)} = 22680 \hat{T}_s^{13} . \tag{23d}$$

If these expressions for $\hat{T}_s^{(n)}$ are substituted into (14a), $\theta(\hat{r}, \hat{t})$ becomes the sum of products of powers of $\hat{r}$ and $\hat{T}_s$ in which the coefficients are numbers, rather than functions of $\hat{t}$. That is, θ becomes a form-invariant function of $\hat{r}$ and $\hat{T}_s$ (or, equivalently, of the forcing function $\hat{T}_s^4$), and its total time dependence is contained in the time dependent of $\hat{T}_s(\hat{t})$. This is one way of characterizing the post-transient regime.

The expressions given in (23) are valid only if the truncation of the infinite series in (20b) is valid. The range of validity of this truncation is indicated by Table I below which uses the eqs. 23 to

calculate the magnitudes of the various terms of eq. 22b for a range of values of $\hat{T}_s^4$. (Powers of 10 are indicated in parentheses following the numbers, e.g. 3.9(-2) = 3.9×10^{-2}.)

Table I

$\hat{T}_s$	$\hat{T}_s^4$	$(-\hat{T}_s^{(1)}/3)$	$(+\hat{T}_s^{(2)}/45)$	$(-2\hat{T}_s^{(3)}/945)$	$(+\hat{T}_s^{(4)}/4725)$
1	1.000	0.525	0.384	-4.709	4.800
3/4	0.316	0.223	3.96(-2)	-6.00(-2)	0.114
1/2	6.25(-2)	5.64(-2)	4.70(-3)	+7.92(-4)	5.86(-4)
1/4	3.91(-3)	3.86(-3)	4.72(-5)	+1.43(-6)	7.15(-8)
1/8	2.44(-4)	2.44(-4)	3.80(-7)	+1.48(-9)	8.73(-12)

A left-to-right sweep of the first row of Table I shows that the magnitudes of the higher-order terms in (22b) are definitely not small compared with the magnitude of the forcing function $\hat{T}_s^4$. However, this is the case for $T_s \leq 1/2$, so it seems safe to conclude that in this range the truncation of the infinite series is a valid procedure.

It is hoped that it will be possible to extend the free-cooling calorimetric method up to temperatures that exceed the melting temperatures of refractory materials by several hundred degrees Kelvin. If the methods and results of this report (and its intended extension to include melting) are to be used, it is necessary that the size of the sample sphere be chosen so that the condition

$$\hat{T}_s \equiv T_s/T_1 = T_s \ (k/Re_J)^{-1/3} \leq 1/2 \qquad (24)$$

is satisfied. Referring to the remarks made in Section 1 above, it is evident that this condition is easily satisfied for a tungsten sphere of radius 1 cm. In fact, at the melting point of tungsten (3653 K), $\hat{T}_s = 0.211$ for a sphere

of this size. However, for a sphere of uranium dioxide of the same size at its melting point (3151 K), $\hat{T}_s = 0.86$. However, for a sphere of radius 1 mm, at the melting point of uranium dioxide $\hat{T}_s = 0.40$, so condition (24) is satisfied. Thus, in applying the free-cooling method, one of the first design considerations is to choose a sample sphere size that is small enough to satisfy condition (24). In general, for metals any radius up to 1 cm would be safe, but for refractory non-metals, 1 mm should be regarded as the upper limit.

The eq. 23a can be written in the form

$$d\hat{t} = - d\hat{T}_s / F(\hat{T}_s) \qquad (25)$$

where $F(\hat{T}_s)$ is the expression contained in the brackets on the right side of (23a). This equation can be integrated to give $\hat{t}(\hat{T}_s)$. When this is carried out to an accuracy consistent with that of eq. 23a, the following equation results:

$$\begin{aligned}
\hat{t} &- \frac{1}{9} \, (\hat{T}_s^{-3} - 1) - \frac{4}{15} \, \ell n \, \hat{T}_s \\
&+ \frac{4}{75} \, (1 - \hat{T}_s^3) + \frac{8}{1575} \, (1 - \hat{T}_s^6)
\end{aligned} \qquad (26a)$$

where

$$\hat{t} \equiv \alpha t / R^2 \quad \text{and} \quad \hat{T}_s \equiv \left[\frac{R \epsilon \sigma}{k} \right]^{1/3} T_b . \qquad (26b,c)$$

The arbitrary integration constant in (26a) has been chosen so that $\hat{t} = 0$ for $\hat{T}_s = 1$. It should be noted, however, that (26a) is reliable only for $\hat{T}_s \leq 1/2$. The first term on the right side of (26a) is the well-known expression that characterizes the cooling of a very good conductor. The other terms allow for the presence of a temperature gradient within the cooling material. The last two terms are not important. If they are omitted, the error that is introduced at $\hat{T}_s = 1/2$ is less than 1%, and considerably smaller than that for smaller values of $\hat{T}_s$. Eq. 26 is

124

a universal cooling curve that is valid for spherical samples of all sizes for materials having constant thermal parameters. It is useful for estimating the cooling time $\Delta t = t_f - t_i$ that is required for a sample to cool down from an initial temperature T_i to a final temperature T_f. Dropping the last two terms in (26a), this becomes

$$\Delta t = \frac{Rc}{9\epsilon\sigma\, T_i^3}\left[\left(\frac{T_i}{T_f}\right)^3 - 1\right] + \frac{4\,R^2}{15\alpha}\,\ell n\left(\frac{T_i}{T_f}\right) . \tag{27}$$

For example, using parameters appropriate to a tungsten sphere of radius 1 cm, one can calculate the time required for the sphere to cool from 3000 K to 1500 K. In this case (27) yields $\Delta t = (501.2 + 0.62)$ seconds. This shows that the second term, that allows for an interior temperature gradient is negligible, although it would have a relatively greater significance in the case of a short time interval near the beginning of the cooling process. This cooling time of 502 seconds is to be compared with the time $R^2/\alpha = 3.3$ seconds that is required for the post-transient regime to become established. The same calculation for a small sphere of uranium dioxide having a radius of 1 mm yields $\Delta t = (28.5 + 0.37) = 28.9$ seconds for the sphere to cool from 3000 K to 1500 K. This interval is to be compared with $R^2/\alpha = 2.0$ seconds, which is the approximate time required for the post-transient regime to become established.

4.   **Calorimetric Problem for Constant Thermal Parameters**

In the calorimetric problem, $E(t)$ and $T(t)$ are given functions, and α and c are unknown constants. A knowledge of the fact that the cooling obeys the T^4 radiation law is necessary only for a calculation of the emittance ϵ, which is given by

$$\epsilon = E(t)/\sigma\,[T(t)]^4 , \tag{28}$$

125

where σ is the Stefan-Boltzmann constant. This relation is actually the definition of ϵ, and it is valid even if ϵ is not constant. From a knowledge of $\epsilon(t)$ and $T(t)$, one could find the temperature-dependent emittance $\epsilon(T)$.

The basic equation is now (22a) rather than (22b). When the definitions contained in (7) are used to convert (22a) into dimensional form, it can be written as follows:

$$- \dot{T}_s (1-F) = 3E/Rc \tag{29a}$$

where

$$\dot{T}_s \equiv d\, T_s/dt \tag{29b}$$

and

$$F \equiv \frac{R^2}{15\alpha \dot{T}} \left(\frac{d^2 T_s}{dt^2} - \frac{2}{21} \frac{R^2}{\alpha} \frac{d^3 T_s}{dt^3} + \frac{R^4}{105\alpha^2} \frac{d^4 T_s}{dt^4} \right). \tag{29c}$$

This yields the following expression for c:

$$c = [3E/R\,(-\dot{T}_s)]\,(1 - F)^{-1}. \tag{30}$$

For a perfect conductor, $F = 0$ because $\alpha = \infty$. For finite α, $F \to 0$ as the sphere cools down because the cooling curve $T_s(t)$, although still descending, tends to flatten out so that the higher derivatives of $T_s(t)$ that appear in F tend to vanish. This suggests a simple procedure for evaluating c and α: First, corresponding readings of E and $\dot{T}_s$ near the cold end of the cooling curve are used to calculate c from (30) with $F = 0$. Then this value of c together with corresponding readings of E and $\dot{T}_s$ near the beginning of the post-transient regime are used in (29a) to calculate a numerical value for F. Using this numerical value of F in (29c), together with the known numerical values of the derivatives of $T_s(t)$, a cubic equation in $(1/\alpha)$ results which can be solved for α. This value of α could then be used in (30) together with the cold temperature readings to calculate an improved value for c, and so on.

A simple analytical expression for α can be derived by neglecting $T_s^{(3)}$ and $T_s^{(4)}$ in (29c). To this approximation,

$$F \doteq \frac{R^2}{15\alpha \dot{T}_s} \ddot{T}_s = \frac{R^2}{15\alpha} \frac{d}{dt} \ln \; (-\dot{T}_s), \tag{31}$$

and when this is used in (29a), the following expression for α results:

$$\frac{R^2}{15\alpha} \doteq \left[\frac{d \; \ln(-\dot{T}_s)}{dt}\right]^{-1} + \frac{3E}{Rc\ddot{T}_s} \; . \tag{32}$$

This expression for α involves c on the right side, but this can be eliminated by a substitution. If (29a) is differentiated, and $T_s^{(3)}$ and $T_s^{(4)}$ are ignored as they were in (31), as well as $\dot{T}_s^2$, the following approximate expression results:

$$\ddot{T}_s \doteq - 3 \; \dot{F}/Rc. \tag{33}$$

With this, (32) becomes

$$\frac{R^2}{15\alpha} \doteq \left[\frac{d \; \ln(-\dot{T}_s)}{dt}\right]^{-1} - \left[\frac{d \; \ln E}{dt}\right]^{-1} \; . \tag{34}$$

It can be shown that the following exact expression can be derived without making any of the above approximations:

$$\frac{R^2}{15\alpha} = \left[\frac{d\ln(-\dot{T}_s)}{dt} - f \; (\alpha, \dot{T}_s)\right]^{-1} - \left[\frac{d\ln E}{dt} - g(\alpha, E)\right]^{-1}, \tag{35a}$$

where

$$f(\alpha, \dot{T}_s) \equiv \frac{2}{21} \frac{R^2}{\alpha} \left[\frac{1}{\dot{T}_s} \frac{d^2 \dot{T}_s}{dt^2} - \frac{1}{10} \frac{R^2}{\alpha} \frac{1}{\dot{T}_s} \frac{d^3 \dot{T}_s}{dt^3}\right],$$

$$g(\alpha, E) \equiv \frac{1}{35} \frac{R^2}{\alpha} \left[\frac{1}{E} \frac{d^2 E}{dt^2} - \frac{2}{45} \frac{R^2}{\alpha} \frac{1}{E} \frac{d^3 E}{dt^3} - \frac{149}{4725} \frac{R^4}{\alpha^2} \frac{1}{E} \frac{d^4 E}{dt^4}\right], \tag{35c}$$

$$\dot{T}_s \equiv dT_s/dt. \tag{35d}$$

Because this expression involves only the _ratios_ $T_s^{(n)}/\dot{T}_s$ and $E^{(n)}/E$, it is insensitive to the calibration of T and E, which is a significant experimental advantage. Furthermore, because this expression involves only α and not c, an iterative process can be employed to calculate an accurate value of α using readings of E(t) and $T_s(t)$ and their derivatives at a single point on the cooling curve. Then these same readings and the calculated value of α can be used to calculate c from (30) without the need for further iteration. In fact, the F that appears in (30) can be written in the following form:

$$F = \frac{R^2}{15\alpha}\left[\frac{d\ln(-\dot{T}_s)}{dt} - f(\alpha, \dot{T}_s)\right]. \tag{36}$$

where $f(\alpha, \dot{T}_s)$ is defined in (35b).

The factor (1-F) that appears in (30) involves derivatives of T_s. It is possible to make use of (35a) to exchange this factor for one that involves only derivatives of E. The resulting expression for c is

$$c = [3E/R(-\dot{T}_s)](1+G), \tag{37a}$$

where

$$G = \frac{R^2}{15\alpha}\left[\frac{d\ln E}{dt} - g(\alpha, E)\right], \tag{37b}$$

where $g(\alpha, E)$ is defined in (35c). It seems likely that, as a matter of experimental technique, T_s and its derivatives will have higher precision than E and its derivatives, so (30) is likely to give better accuracy than (37).

Although these expressions for α and c appear to involve readings taken at only one point on the cooling curve, in actual fact they involve readings at several neighboring points, because these are necessary to calculate the various derivatives of T_s and E which are not measured

directly in the experiment. However, once these derivatives have been calculated (ard any necessary smoothing of the data carried out), the expressions (35) and (30) (or (37)) can be used to march along the cooling curve and calculate an independent pair of values for α and c at each point of the curve. Thus, if these thermal parameters are actually mild functions of temperature rather than constants, this procedure ought to give reasonably accurate expressions for $\alpha(T)$ and $c(T)$.

There are two sources of error in this procedure, however, which will be corrected in the next section. One is that the calculated values of α and c should not be associated with the surface temperature of the point on the cooling curve at which they were calculated, but rather with a temperature resulting from some kind of averaging throughout the volume of the sphere. Second, the temperature dependence of the thermal parameters makes the basic differential equation nonlinear, and not just the boundary condition. In spite of these considerations, the application of the results of this section will provide good first approximations for insertion into the formulas that are derived in the next section.

5.   Calorimetric Problem for Temperature-Dependent Parameters

The strategy that will be employed in chis section is to invoke appropriate redefinitions of both the dependent variables in order to reduce the problem to one which, in its dimensionless form, is identical to the dimensionless form of the calorimetric problem for constant parameters. In this way a formal solution of the equation and boundary conditions is achieved. When the transition is made back to the dimensional quantities appropriate to the experiment, the effects of the changes in

variables that were made at the beginning of the solution manifest themselves, with the result that terms involving the derivatives of the parameters with respect to temperature appear in the expressions for α and c. These expressions are the desired generalizations of those derived in the preceding section. This approach automatically refers everything to the surface temperature T_s and to the values of the parameters at the surface, even though the effects of the higher temperatures of the interior are implictly taken into account.

The equation and boundary condition are the same as given in eqs. 4 and 5a, except that now k(T) and c(T) are arbitrary and independent functions of temperature. Instead of working with T as the dependent variable, the enthalpy density h(T) now assumes this role where

$$h(T) = \int_{T_r}^{T} c(T') \, dT' + h_r,$$
(38a)

and

$$h_r \equiv h(T_r).$$
(38b)

T_r is any convenient constant reference temperature. Strictly speaking, h(T) is actually the enthalpy of that quantity of matter which occupies unit volume at the reference temperature, but which at a different temperature occupies a slightly different volume because of the temperature dependence of the mass density. For simplictly, however, h will be called simply the enthalpy density. In terms of h, the partial differential equation and the boundary condition become

$$\underline{\nabla} \cdot [\alpha(T) \underline{\nabla} h] = \partial h / \partial t$$
(39a)

and

$$- \alpha_s (\partial h / \partial r)_{r=R} = E(t)$$
(39b)

where

$$\alpha(T) \equiv k(T) / c(T)$$
(40a)

130

and

$$\alpha_s \equiv \alpha \ (T_s). \tag{40b}$$

α_s is a function of t via the time dependence of $T_s(t)$, and this function $\alpha_s(t)$ will be used to define a dimensionless time variable τ:

$$\tau \equiv R^{-2} \int_0^t \alpha_s(t') \ dt'. \tag{41}$$

Using (41), the eq. 39a can be put into the following form:

$$\nabla^2 h + \underline{\nabla} \cdot \left[\left(\frac{\alpha}{\alpha_s} - 1 \right) \underline{\nabla} \ h \right] = R^{-2} \partial h / \partial \tau \tag{42}$$

where the second term on the left is an effective heat source density arising from the effective heat flux $-[(\alpha/\alpha_s) - 1] \ \underline{\nabla}h$. This effective flux vanishes at the surface of the sphere where $\alpha = \alpha_s$. Because of this, the volume integral of the effective heat source is zero. If the effect of this effective source density were taken into account by an iterative perturbation technique, it would be found that h would have to be corrected by a small amount δh such that $\underline{\nabla}\delta h$ would be very nearly equal to the effective flux density $-[(\alpha/\alpha_s) - 1]\underline{\nabla}h$. Because this vanishes at the surface, so would $\underline{\nabla}\delta h$ and $(\partial \delta h / \partial r)_s$. Because of this, the correction δh would produce no change in the boundary condition (39b) which gives rise to the equation from which the expressions for α and c are derived. In other words, the second term on the left side of (42) would produce a slight change in the interior h-field, but it would produce no significant effect on the equation that is derived from the boundary condition involving E, and this equation is all that matters for the solution of the calorimetric problem.

The reference temperature T_r, and the values of the sundry quantities at this temperature, are used to make the equation and boundary condition

131

dimensionless. Dimensionless quantities will be designated by a circumflex. Thus

$$\hat{c} \equiv c/c_r \equiv c(T)/c(T_r); \quad \text{and} \quad \hat{\alpha} \equiv \alpha/\alpha_r \equiv \alpha(T)/\alpha(T_r). \qquad (43\ a,b)$$

The characteristic temperature is now defined in terms of the values of the material constants ϵ_r and k_r at the reference temperature:

$$T_1 \equiv (k_r/R\epsilon_r\sigma)^{1/4}. \qquad (44)$$

This is used to scale both h and T:

$$\hat{h} \equiv h/c_r T_1 = \int_{T_r}^{\hat{T}} \hat{c}(\hat{T}')\ d\hat{T}' \ + \ h_r/c_r T_1 \qquad (45a)$$

where

$$\hat{T} \equiv T/T_1. \qquad (45b)$$

The dimensionless independent variables are

$$\hat{r} \equiv r/R \quad \text{and} \quad \tau \equiv \alpha_r R^{-2} \int_0^t \hat{\alpha}_s(t')\ dt'. \qquad (46a,b)$$

In complete analogy with the variable θ defined in (10), it is convenient to introduce the variable η defined by

$$\eta\ (\hat{r},\tau) = \hat{r}\ \left[\hat{h}(\hat{r},\tau) - \hat{h}_s(\tau)\right]. \qquad (47)$$

In terms of these variables, the equation becomes

$$\partial^2\eta/\partial\hat{r}^2 + \hat{r}\ \left[\gamma - d\ \hat{h}_s/d\tau\right] = \partial\eta/\partial\tau \qquad (48a)$$

where

$$\gamma \equiv \hat{r}^{-2}\ \frac{\partial}{\partial\hat{r}}\left[(\frac{\alpha}{\alpha_s} - 1)\ (\hat{r}\ \frac{\partial\eta}{\partial\hat{r}} - \eta)\right] \qquad (48b)$$

$$= \hat{r}^{-2}\ \frac{\partial}{\partial\hat{r}}\left[(\frac{\alpha}{\alpha_s} - 1)\ \hat{r}^2\ \frac{\partial\hat{h}}{\partial\hat{r}}\right]. \qquad (48c)$$

132

The boundary conditions are

$$(\eta)_{\hat{r}=0} = 0 \; ; \qquad (\eta)_{\hat{r}=1} \equiv \eta_s = 0 \qquad\qquad (49)$$

$$- (\partial \eta / \partial \hat{r})_{\hat{r}=1} = \hat{E}/\hat{\alpha}_s \qquad\qquad (50)$$

where

$$\hat{\alpha}_s \equiv \alpha(T_s)/\alpha(T_r); \; \hat{E} \equiv RE/k_r T_1 \; ; \quad T_1 \equiv (k_r/R\epsilon_r \sigma)^{1/3}. \qquad\qquad (51a,b,c)$$

Except for the presence of the $\hat{r}\gamma$ term in (48a), this equation and the homogeneous boundary conditions (49) are identical to the system defined by (10) and (11), and could be solved in the same way if the $\hat{r}\gamma$ term were ignored. The inclusion of this term presents no fundamental problem since it can be handled by an iterative approach that treats it as a prescribed forcing function like $(-dh_s/d\tau)$, except that γ depends on $\hat{r}$ as well as τ. The formal solution of (48a) including $\gamma(\hat{r},\tau)$ (regarded as a specified function rather than as a function of η) has been carried out, but will not be given here, because numerical analysis (not yet carried out) will almost certainly show that the error caused by ignoring the $\hat{r}\gamma$ term in the case of any material of practical interest is not greater than the error caused by truncating the infinite series for η. For this reason, the $\hat{r}\gamma$ term will be ignored, and the solution for $\eta(\hat{r},\tau)$ will be taken to have the same form as that given in (14).

The same argument that converted the boundary condition (19a) into the ordinary differential equation (22a) now leads to the following equation:

$$\frac{1}{4725} \frac{d^4\hat{h}_s}{d\tau^4} - \frac{2}{945} \frac{d^3\hat{h}_s}{d\tau^3} + \frac{1}{45} \frac{d^2\hat{h}_s}{d\tau^2} - \frac{1}{3} \frac{d\hat{h}_s}{d\tau} = \hat{E}/\hat{\alpha}_s . \qquad\qquad (52)$$

This is identical in form to (22a) except that $\hat{T}_s$, $\hat{t}$, and $\hat{E}$ are replaced by $\hat{h}_s$, τ, and $\hat{E}/\hat{\alpha}_s$ respectively. To convert to the dimensional form it is only necessary to note that it follows from (45a) and (41) that

133

$$\frac{d\hat{h}_s}{d\tau} = \frac{dT_s}{d\tau}\left(\frac{d\hat{h}}{dT}\right)_s = \left(\frac{d\tau}{dt}\right)^{-1}\frac{dT_s}{dt}\frac{c(T_s)}{c_r T_1} = \frac{R^2 c_s}{\alpha_s c_r T_1}\frac{dT_s}{dt} \quad . \tag{53}$$

Successive differentiation proceeds in the same way, with care being taken to note that

$$\frac{dc_s}{d\tau} = \left(\frac{d\tau}{dt}\right)^{-1}\left(\frac{dc}{dT}\right)_s\frac{dT_s}{dt} = \frac{R^2}{\alpha_s}\frac{dc_s}{dT_s}\frac{dT_s}{dt} \tag{54}$$

and similarly for $d\alpha_s/d\tau$.

The same procedures employed in Section 4 that led to expressions for α and c in the case of constant parameters now lead to similar expressions that include the effects of the variability of the parameters. The expression for $\alpha_s \equiv \alpha\,(T_s)$ is

$$\frac{R^2}{15\alpha_s} = \left[\frac{d\ln(-\dot{T}_s)}{dt} - f'(\dot{T}_s,c_s,\alpha_s)\right]^{-1} - \left[\frac{d\ln E}{dt} - g'(E,\alpha_s)\right]^{-1} \tag{55a}$$

where

$$f'(\dot{T}_s,c_s,\alpha_s) = \frac{d\ln\alpha_s}{dt} - \frac{d\ln c_s}{dt}$$

$$+ \frac{2}{21}\frac{R^2}{\alpha_s}\left[\frac{1}{\dot{T}_s}\frac{d^2\dot{T}_s}{dt^2} - \frac{1}{10}\frac{R^2}{\alpha_s}\frac{1}{\dot{T}_s}\frac{d^3\dot{T}_s}{dt^3}\right.$$

$$+ \frac{d^2\ln c_s}{dt^2} - \frac{d^2\ln \alpha_s}{dt^2}$$

$$+ \frac{1}{\dot{T}_s}\frac{d\dot{T}_s}{dt}\left(2\frac{d\ln c_s}{dt} - 3\frac{d\ln \alpha_s}{dt}\right)$$

$$\left.+\left(\frac{d\ln \alpha_s}{dt} - \frac{d\ln c_s}{dt}\right)\left(2\frac{d\ln \alpha_s}{dt} - \frac{d\ln c_s}{dt}\right)\right]$$

and

$$g'(F,\alpha_s) = \frac{d\ln \alpha_s}{dt} + \frac{1}{35}\frac{R^2}{\alpha_s}\left[\frac{1}{E}\frac{d^2E}{dt^2} - \frac{2}{45}\frac{R^2}{\alpha_s}\frac{1}{E}\frac{d^3E}{dt^3}\right.$$

$$\left.- \frac{d^2\ln \alpha_s}{dt^2} - 3\frac{d\ln E}{dt}\frac{d\ln \alpha_s}{dt} + 2\left(\frac{d\ln \alpha_s}{dt}\right)^2\right] \tag{55c}$$

where the terms involving $E^{(4)}$ and third and higher derivatives of $\ln \alpha_s$ and $\ln c_s$ as well as cubics in the first derivatives of these have been neglected.

The two alternative expressions for $c_s \equiv c(T_s)$ are

$$c_s = \frac{3E}{R(-\dot{T}_s)} \left\{ 1 - \frac{R^2}{15\alpha_s} \left[\frac{d\ell n(-\dot{T}_s)}{dt} - f'(\dot{T}_s, c_s, \alpha_s) \right] \right\}^{-1} \tag{56}$$

where $f'(\dot{T}_s, c_s, \alpha_s)$ is given by (55b), and

$$c_s = \frac{3E}{R(-\dot{T}_s)} \left\{ 1 + \frac{R^2}{15\alpha_s} \left[\frac{d\ell n\ E}{dt} - g'(E, \alpha_s) \right] \right\} \tag{57}$$

where $g'(E, \alpha_s)$ is given by (55c).

The point of view to be taken in applying these expressions is that $E(t)$ and $T_s(t)$ are given, and after suitable smoothing their sundry time derivatives are calculated. These functions are then substituted into (35) and (30) to obtain the time-dependent functions $\alpha(t)$ and $c(t)$ which are then used for α_s and c_s on the right sides of (55) and (56) to evaluate more accurate functions $\alpha_s(t)$ and $c_s(t)$ which are reinserted into the right sides of (55) and (56), and so on until the process converges. From the final functions $\alpha_s(t)$ and $c_s(t)$, together with $T_s(t)$, the functions $\alpha(T_s)$ and $c(T_s)$ can be found. Because α and c are functions of T alone, and the functional relations are the same in the interior of the sphere as on the surface, the subscript s can be dropped since the computed functions are the desired functions $\alpha(T)$ and $c(T)$.

It is probable that a numerical analysis will show that, for the kinds of functional relations $\alpha(T)$ and $c(T)$ that are encountered in the case of any real material of practical interest, many of the terms in (55b) and (55c) are negligible in the sense that they are smaller than the experimental error of the larger terms.

135

6. Discussion of Part B

The working formulas for the application of the free-cooling calorimetric method are (55) and (56) (or eq. 57). It is noteworthy that (55) (the expression for α) is completely insensitive to the units used to measure E and T_s since only relative values enter into the formula. Thus, for the calculation of α, it is not necessary to calibrate the instruments in absolute terms since arbitrary units can be used. In the case of the calculation of c, the value of $(E/\dot{T}_s)$ is the only quantity that must be calibrated. If the value of c is known for the sample in question at any temperature (most likely the coldest temperature in the experimental range), then the calibration can be made at that temperature. If c is completely unknown for the material in question, then an entirely different material and different sphere size can be used for calibration purposes if c for the calibration material is known at some temperature.

The derivation of the working formulas made no assumption whatever about the dependence of E on T_s. Rather, it was simply assumed that $E(t)$ and $T_s(t)$ were independent given functions. Only in the calculation of the emittance $\varepsilon(T_s)$ was any assumption made about the physical nature of the cooling. (Cf. eq. 1.) Thus the formulas for α and c apply also to a sphere that is cooled by some mechanism other than radiation into a cold vacuum so long as the assumption of spherical symmetry remains valid.

There is no fundamental reason why the methods employed in this report could not be adapted to cylindrical geometry. This geometry admits the possibility of controlled electrical heating of refractory materials (an established experimental technique). Such heating would be represented in the formalism as a prescribed heat source density. The definition of the post-transient regime would have to be modified only to the extent of including the prescribed heat source as one of the determining factors,

along with the cooling law and the thermal parameters. Such prescribed heat sources have already been included in the analysis for spherical geometry. Although their inclusion complicates the formalism, it introduces no fundamental difficulties.

Following a numerical test and confirmation of the relations derived in this report, the proposed next stage of development of the analysis is the inclusion of the possibility of a solid spherical shell surrounding a molten core that shrinks in size as the sphere cools. The object or this analysis would be to determine the heat of fusion, i.e. the jump in enthalpy density across the solidification front. For this purpose h is a much more natural variable than T, so the formalism of Section 5 should provide a natural starting point.

References for Part B

1. M.N. Özişik, *Heat Conduction* (Wiley, New York, 1980)

2. B.F. Jones, J. Math. Mech. $\underline{11}$, 907 (1962)

3. J. Douglas and B.F. Jones, J. Math. Mech. $\underline{11}$, 919 (1962)

4. B.F. Jones, Comm. Pure Appl. Math. $\underline{16}$, 33 (1963)

5. J.R. Cannon and B.F. Jones, Int. J. Engng Sci. $\underline{1}$, 457 (1963)

6. J.R. Cannon, J. Math. Anal. Appl. $\underline{8}$, 188 (1964)

7. J.R. Cannon, P.C. DuChateau, and D.L. Filmer, Math. Biosciences $\underline{9}$, 61 (1970)

8. J.R. Cannon and P. DuChateau, SIAM J. Appl. Math. $\underline{24}$, 298 (1973)

9. J.R. Cannon and P. DuChateau, Int. J. Engng Sci. $\underline{11}$, 783 (1973)

10. J.R. Cannon and P. DuChateau, SIAM J. Appl. Math. $\underline{39}$, 272 (1980)

11. V. Mangulis, *Handbook of Series* (Academic Press, New York, 1965)

12. See, for example, p. 40 of reference 11.

Task 5

Experimental and Theoretical Studies in Wetting and Multilayer Adsorption.

M. R. Moldover and J. W. Schmidt

Thermophysics Division

Center for Chemical Physics

J. W. Cahn

Center for Materials Science

Summary

Equipment has been assembled and/or fabricated to measure the ellipsometric parameters of the liquid-vapor interface of binary mixtures near the predicted transition from high adsorption to low adsorption. Preliminary measurements on the mixture C_7F_{14} - C_7H_{14} have not yet discovered the predicted transition. A variety of interfering phenomena have been tracked down. Further measurements are in progress.

Introduction

We have assembled a semi-automatic ellipsometer together with sample cells and a thermostat capable of precisely monitoring the ellipsometric parameters of the liquid-vapor interface above binary liquid mixtures. We have made a computer model of the ellipsometer in order to optimize its sensitivity to the appearance of the predicted high adsorption layer. We have tested a method of measuring and recording the index of refraction of the binary mixture under study simultaneously with the recording of the ellipsometric parameters. The index of refraction measurement is extremely sensitive to the appearance of macroscopic amounts of a second liquid phase; thus it will serve to locate the adsorption transition with respect to the miscibility gap in the specific liquid sample under study. We expect the strategy of simultaneously measuring the index of refraction and the ellipsometric parameters to obviate the necessity of carrying out detailed exacting chemical analyses of each sample of each mixture to be studied.

In preliminary measurements we have searched for the predicted[1,2] high adsorption-low adsorption transition in the liquid-vapor interface between a C_7F_{14} - C_7H_{14} mixture and air saturated with this mixture's vapor. We have found no evidence of such a transition in a sample which undergoes phase separation near 23°C. (The consolute temperature in this system is near 46°C.) This sample is approximately 7% fluorocarbon on a mole fraction basis. In these preliminary measurements, the ellipsometric parameters showed a smooth temperature dependence between 23°C and 60°C which would be equivalent to the adsorption of a 70Å thick layer of the fluorocarbon at the interface between the vapor and this

hydrocarbon-rich liquid. This temperature dependence is probably spurious. At the moment our highest priority is to determine its origin. These preliminary measurements could have detected an abrupt high adsorption-low adsorption transition equivalent to a 20Å change in the thickness of a fluorocarbon-rich layer at the liquid-vapor inter-face. We expect improved sensitivity in future measurements and to scan the composition range in order to locate and trace out the expected interface transition curve on a phase diagram.

The index of refraction measurement revealed a secular drift in the temperature at which bulk phase separation occurred (roughly 0.5°C/month). This was traced to a leak in the quartz sample cell which we have now repaired.

The measurement system we are developing will be automated. This is required because of the long equilibration times encountered.

Experimental Procedures

The experimental procedures we have carried out will be described under the following subheadings: (1) Optical Table, (2) Thermostat, (3) Equilibration (4) Sample cell, (5) Model for ellipsometer, (6) Optical components for ellipsometer, (7) Optical components for index of re-fraction measurement, and (8) Sample preparation. When it is appropriate, we will indicate the rationale for the procedure followed as well as the improvements we anticipate in the near future. Figure 1 shows the experimental arrangement.

(1) Optical Table: The ellipsometric measurement is sensitive to the angle of the incident light. As the liquid-vapor surface sloshes about (from ambient vibrations) the angle of incidence varies. Further-

more, the path of the reflected beam through various optical components is also a function of the instantaneous position of the surface. These two effects modulate the intensity of the reflected beam. Thus they appear as noise in the ellipsometry. A commercially manufactured air suspension table was purchased and installed to use as a low vibration support for the entire experiment. Even at the comparitively low sloshing frequencies the table significantly reduced the liquid-vapor surface vibrations. The table is held very nearly level by a system of valves which admit compressed air to the legs. When functioning properly the variations in level are $\pm$ 1 milliradian. This seems to be satisfactory at the present precision of our measurements. We have found that occasionally one of the valves may stick. Then, much larger excursions in the position of the table level occur. These excursions are correlated with room temperature variations (which alter the air pressure in the table suspension) and are corrected periodically as the valve finally opens. This larger amplitude tilting produced an un-acceptably large ellipsometric signal whose origin was tricky to locate. Ultimately we may have to regulate the table level with a much smaller dead band than the compressed air servo system tolerates. This is possible by moving two small weights on the table.

(2) Thermostat: We are now using a two stage thermostat. The temperature of the outer stage is controlled by circulating water from an external circulater/thermostat. We have used this circulator between 15 C and 60°C. The temperature of a particular point on the outer shell is now monitored with a thermistor. Temperature fluctuations of this point are on the order of $\pm$ 0.05°C.

The thermal relaxation time of the sample is several hours (see below). We change the temperature setpoint of the outer stage by switching resistors in parallel with the temperature sensitive element of the regulator. The switching is done at preselected times. This hardware based programming scheme will eventually be replaced with a software based one incorporating feedback.

The inner shell of the thermostat is regulated by a home-made electronic servo system using a thermistor sensor. The set point temperature exhibits noise of less than 10^{-4}C; however, there are substantial temperature gradients across the inner stage (roughly 30 mK). In the near future two improvements will be made to reduce this gradient by nearly two orders of magnitude. First, the point heaters on the inner shell will be replaced by a distributed heater placed symmetrically around the shell. Second, the temperature of the outer shell's set point will be servoed in such a way as to maintain the outer shell's temperature much closer to that of the inner shell.

(3) Equilibration: Equilibration of concentration gradients in binary mixtures via diffusion is a notoriously slow process. Typical diffusion constants in the liquids of interest are 10^{-5} cm^2/s. Typical dimensions of our samples are 3 cm; thus characteristic times should be several hours when one liquid phase is present and much longer when two liquid phases are present. A magnetic stirring bar has been enclosed in a glass envelope and placed within the sample cell. This bar is turned periodically (e.g. 2 minutes every 30 minutes) by a second magnet built into the thermostat which in turn is attached to a motor outside the thermostat. We are able to directly observe equilibration

of the ellipsometric parameters of the liquid-vapor surface after a temperature change. When one liquid phase is present, equilibration takes about one hour. When two phases are present, equilibration can be monitored using the index of refraction measurement because the index of only the upper phase is measured. We have observed that equilibration took between two and four hours when the sample was cooled into the two phase region even though the liquid-vapor interface acts as a nucleation site for the lower fluorocarbon-rich liquid phase and the sample is stirred vigourously.

(4) Sample cells: The sample cells are essentially hollow prisms. They are fabricated from fused quartz windows and quartz tubing held together with a high melting temperature solder glass. The cells are filled through a quartz tube which is sealed with a teflon stopper and O-ring. (It is possible to seal the cells by fusing the tube shut; however, at this point we have not done so). The prism angle is 60° and is oriented with its apex upward. The angle of incidence for the ellipsometer is near 60°. This minimizes the influence of the residual birefringence of the cell's windows on the ellipsometer performance. This angle of incidence is also close to Brewster's angle for the hydrocarbon-rich mixture; thus, it is near optimum for the ellipso-meter's sensitivity.

In equilibrium, the liquids under study are in contact with quartz and vapor (the stopper is in the vapor phase). The hydrocarbon-rich phase of C_7F_{14}-C_7H_{14} mixtures totally wets the quartz. Thus the sample cells' walls and corners as well as the glass encapsulated stirring bar do not act as nucleation sites for the appearance of the fluorocarbon

rich phase. The fluorocarbon-rich phase can only appear at the liquid-vapor interface, the interface we are studying ellipsometrically. The absense of "traps" for the fluorocarbon-rich phase insures that the index of refraction measurement will clearly indicate the initial formation of macroscopic amounts of this phase.

(5) Model for the Ellipsometer: The ellipsometer arrangement is a conventional one: source-polarizer-compensator-sample-analyzer-detector. In order to choose reasonable design compromises, a computer program was written to calculate the intensity at the detector as a function of the angle of incidence, the orientations of the polarizer, compensator, and analyzer, the index of refraction of the substrate fluid, and the thickness and index of refraction of the multilayer adsorbed film we are searching for. This program is an essential tool for the design of the instrument and the interpretation of the measurements. With it we can explore the sensitivity of the measurements to extraneous factors such as the tilt of the table and component imperfection.

(6) Optical components for the ellipsometer: A 1mW He-Ne laser is used as a source. The polarizer and analyzer crystals have an extinction ratio near 10^6. A Faraday modulator is inserted between the polarizer and analyzer. In effect, it rotates the plane of polarization through a few tenths of a degree. The modulator is excited with an AC signal so that the photomultiplyer output can be monitored with a lock-in amplifier. A DC signal is also fed back to the modulator to insure that the intensity of the detector is near null. The ellipsometer is set up for extinction when the sample is at a high temperature. Then we expect essentially zero preferential adsorption at the liquid-vapor surface. As the sample

is cooled the DC component of the current fed back to the modulator is continuously monitored. If a thin dielectric film, i.e. an adsorbed layer, appears on the liquid surface the extinction will be maintained by the feedback signal. This method does fail when the layer becomes on the order of 1/8 of a wavelength of light thick. Then two optical components must be adjusted to maintain extinction.

An integrator with a 2 minute period is used in the feedback loop to average over the interface vibrations.

The most serious problem we have encountered with this arrangement is an ambient temperature dependent residual ellipticity introduced by the modulator. We have started monitoring this by periodically inserting a test sample between the modulator and a second detector. This sample simply a quartz flat whose optical properties are constant. In the future, we will attempt to use thermostated modulator of our own design.

(7) Optical components for index of refraction measurement: The index of refraction measurement is based on measuring the deviation that a collimated beam of light experiences upon passing through the prism-shaped sample cell. A second He-Ne laser is used as a light source. Its beam is spatially filtered and expanded to fully illuminate the cell. The beam passes through the cell and is reflected back upon itself. (This doubles the sensitivity of the index of refraction measurement and reduces the number of windows needed for the thermostat). A beam splitter is used to separate the returning beam from the incident one. A telescope focuses the returning beam upon a position sensitive detector. The voltage from the detector provides a continuous monitor of changes in the index of refraction of the sample.

(8) Sample preparation: The C_7F_{14}-C_7H_{14} mixtures are prepared from the pure components as received. A rough measurement indicates the consolute temperature of our samples are within 1°C of that reported in the literature for these components. Because we intend to establish the location of the adsorption transition in relation to the phase separation temperature it is not necessary to prepare mixtures of a precisely known composition. Instead we prepare mixtures such that two phases are present at the temperature at which phase separation is desired. Then the hydrocarbon-rich upper phase is drawn off and used as the sample.

Experimental Results

As we have indicated, the experimental techniques are still being actively developed. The tests of the apparatus that have been carried out to date have not yielded new results of physical significant. We have not yet observed the predicted phase transition, but we have scanned only one composition.

Conclusions and Discussion

The measurement technique we have developed can be improved significantly. Substantial progress is expected in the near future. An automatic data acquisition system has been ordered. As of this writing, the primary factor limiting the resolution of our present equipment is a large temperature dependent shift in the apparent etllipsometric parameters of our fluid samples.

References

1. M. R. Moldover and John W. Cahn, Science 207, 1073 (1980).
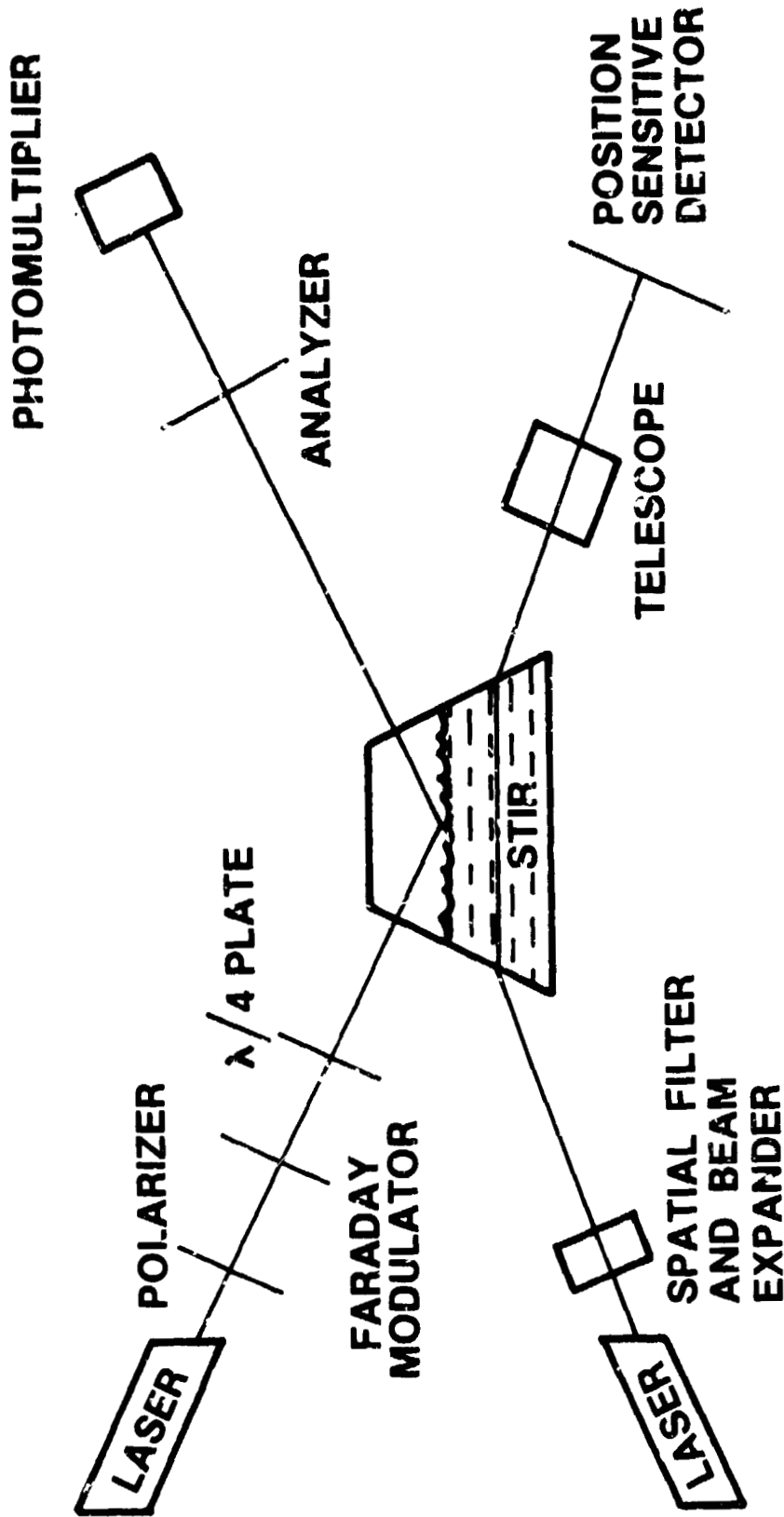2. J. W. Cahn, J. Chem. Phys. 66, 3667 (1977).

Figure 1. Schematic diagram of experimental apparatus. In ellipsometer measurements the laser beam, after passing through a polarizer, Faraday moderator and quarter-wave plate, is reflected from the surface of the liquid mixture in the sample chamber and subsequently analyzed. Simultaneously a second laser beam passing through the stirred mixture, as indicated in the lower part of the diagram, can be used to measure the index of refraction of the mixture.